Modeling time-dependent optical and UV correlations in active galactic nuclei

Patricia Rojas Lobos

UNIVERSITÉ DE STRASBOURG

ÉCOLE DOCTORALE DE PHYSIQUE ET CHIMIE-PHYSIQUE – ED 182

OBSERVATOIRE ASTRONOMIQUE DE STRASBOURG

THÈSE

présentée par :

Patricia Andrea ROJAS LOBOS

soutenue le : **21 décembre 2018**

pour obtenir le grade de : **Docteur de l'université de Strasbourg**

Discipline/ Spécialité : Astrophysique

Modélisation des corrélations temporelles dans les bandes optiques et ultraviolettes dans les Noyaux Actifs de Galaxies

THÈSE dirigée par :

Mr GOOSMANN René	Ancien Maitre de Conférence HDR, Université de Strasbourg
Mr HAMEURY Jean-Marie	Directeur de recherche au CNRS, Université de Strasbourg

RAPPORTEURS :

Mme NEINER Coralie	Directrice de recherche au CNRS, Observatoire de Paris
Mr POPOVIĆ Luka	Professor, University of Belgrade

AUTRES MEMBRES DU JURY :

Mr ALLEN Mark	Directeur de recherche au CNRS, Université de Strasbourg
Mme BOISSON Catherine	Astronome, Observatoire de Paris

Patricia Andrea ROJAS LOBOS

Modélisation des corrélations temporelles dans les bandes optiques et ultraviolettes dans les Noyaux Actifs de Galaxies

Résumé

Les Noyaux Actifs de Galaxie (AGN) incluent les sources quasi stables les plus énergétiques connues dans l'univers jusqu'à aujourd'hui. Du fait de leur distance, de leur haute luminosité et de leur petite taille, leurs régions intérieures ne sont pas directement résolvables avec les télescopes actuels. C'est pour ces raisons que nous avons besoin de techniques d'observation indirectes et de modèles théoriques pour discerner leur structure. Dans cette optique, le rôle de la polarimétrie est crucial. Elle a été ces dernières années la méthode clé qui a permis de développer le modèle unifié des AGN et pourrait, à l'avenir, nous offrir des nouveaux éléments pour sonder les régions des AGN irrésolues. Dans cette thèse, j'ai conduit des simulations sur les transferts radiatifs relatifs aux rayonnements continus émis des différentes régions intérieures des AGN en utilisant la nouvelle technique de cartographie de réverbération polarimétrique. Ce travail a été inspiré par les recherches de Gaskell et al. (2012). Le but de cette recherche est de fournir des modèles théoriques sur les différents composants des AGN en considérant le rayonnement polarisé en fonction du temps. La polarisation induite par la diffusion a été modélisée et différentes géométries de poussières circumnucléaires ont été testées. Les résultats incluent les effets de l'agrégation des poussières et différentes compositions de poussière. Pour étendre le modèle, les effets complémentaires des vents ionisés s'étirant en direction des pôles ont également été étudiés ainsi que ceux de l'anneau de diffusion équatorial théorique, avec pour postulat qu'il explique l'angle de polarisation observé dans les pôles des AGN. Les simulations ont été exécutées en utilisant une version du *code S*TOKES incluant la dépendance temporelle. Il sera possible d'étendre ce travail à l'avenir. Les prochaines étapes suggérées incluront des raies d'émission aux modélisations ainsi que plus de complexité concernant la géométrie et la distribution de la poussière et/ou des électrons dans les régions de diffusion. Ce travail sera important pour profiter de futures données observationnelles systématiques avec un bon échantillonnage temporel.

Mots clés : Noyaux Actifs de Galaxie – polarisation – cartographie de réverbération – transfert radiatif.

Résumé en anglais

Active Galactic Nuclei (AGN) include the most powerful quasi-steady sources of energy known to date in the universe. Due to their distance, high brightness and small size, their inner regions are not directly resolvable with current telescopes. This is the reason why indirect techniques and theoretical models are needed to discern their structure. In this scenario the role of polarimetry is crucial. In the past it was the key method that led to the development of the Unified Model of AGN and in the future, it may give us new clues to probe unresolved AGN regions. In this thesis, I conducted radiative transfer simulations for continuous radiation of different inner regions of the AGN using the new technique of polarimetric reverberation mapping. This work has been inspired by the work of Gaskell et al. (2012). The goal of this research is to provide theoretical models of the different components of the AGN considering time-dependent polarized radiation. Scattering-induced polarization has been modeled and different circumnuclear dust geometries have been explored. The results include the effects of clumpiness and different dust compositions. To further extend the model, the effects of additional extended ionized winds along the polar direction have also been explored as well as the putative equatorial scattering ring postulated to explain the polarization angle observed in pole-on AGN. The simulations were run using a time-dependent *versio*n of *the S*TOKES code. It will be possible to extend this work in the future. Suggested future steps are including emission lines in the models, as well as more complexity in the geometry and distribution of dust and/or electrons in the scattering regions. This work will be important for taking advantage of systematic future observational data with good temporal sampling.

Keywords: Active Galactic Nuclei – polarization– reverberation mapping – radiative transfer.

Modeling time-dependent optical and UV correlations in Active Galactic Nuclei

Acknowledgments

I'm very grateful for a life that has allowed me to spend these years working on my PhD thesis in a country that has welcomed me and where I have made good friends. I am grateful for the opportunity to participate in scientific conferences where I have been able to expand my horizons on a scientific, human and social level. These years have left me full of wonderful experiences.

I would like to begin by thanking Martin Gaskell, my mentor, the first person to introduce me to the exciting world of AGNs and who has always been an invaluable supporter. I am very grateful to René Goosmann, who was my Ph.D. supervisor for almost three years. He was always very kind and a good teacher and without him this thesis could not have been completed. Many thanks are due to Jean-Marie Hameury who took over the task of accompanying me as my thesis supervisor for the last year, a great contribution. I am also very grateful to Frédéric Marin, who although not officially a supervisor, has not only taught me about polarimetry but also about professionalism and human qualities.

I want to thank the people at the Strasbourg Observatory, where I felt welcomed from the very first moment and who I have been loving and discovering year after year, meeting every Friday for the observatory breakfast or enjoying together 'le repas de solstice' every year: Sandrine et Véronique, Ludovic and his team, Thomas, the nice people in the east building: Emmanuelle, Evelyne, Mihaela, Caroline, Sébastien, Benoît, Magali, François-Xavier, André, Patricia, Philippe, Marc, Magali. I also want to thank those of you who share a coffee at "la Menuiserie": Ada, Mari, Fabién, Estrella, Iwona, Yelena, Catherine, Bertrand, Mireille, Pierre, Chaitra, Laurence, Ariane, Anaïs, Madjid, Francesco. Then I must thank my fellow doctoral students, some of whom have already obtained their doctorates: François, Jean-Baptiste, Nicolas, Guillaume, Nicolas, Maxime, Mathieu, Julien, Enmanuelle, Guillaume, Tohir, Jerôme, Khyati, Nicolas, Joseph, Quentin, Timothe, Federico. Most of all I have to thank my friends who have helped me enormously: Anu with her tenderness and support. And my great friend and thesis, conference, travel, beer and "*STOKES*" partner, Djordje.

Thanks are due to the friends I met in France on Tuesdays first at the Schloss and then at the Cafe Berlin. Then there are the friends of the Wednesday tandem and the friends of the CDE. For the support and friendship I must thank Ewa, Selver, Inna, Nico, Fran, Sylvain, Zsuzsanna, Catita, Pablo de Costa Rica, Pablo de Chile, Magda, Edmond, Alex, Alex, Alex, Karim, Danko, Mila, Sauri, Carola, Ufuk. Special thanks to Pilar and Marcel for their help in the thesis review. Simon, Lina, Leandro, Geza, Gabriela, Maria Victoria, Marina, Sandra, Ana Luisa, Father Adrian.

Many thanks also to my friends in Chile, who have been keeping in touch with me, despite the distance, offering me their support, friendship and love: Fran, Rafita, Rosa Maria, Gise, Nicola, Sole, Nathalie, Karina, Karla, Amokrane, Javi, Irma, Ida, Edith, Carmen Luz, Pam, Tito, Jaime, Nathalia, Monica, Maria Loreto, Father Ivan, Father Carlos.

I could not finish without thanking the most important people in my life, my family: my parents Patricia y Ricardo, who with their unconditional love and dedication have always been present, supporting me, and upholding my decisions and, standing by me at all times, even when the decision to do a doctorate so far away meant a painful separation. Many thanks to my siblings, Monica and Alex, and my nephews, Sofia and Matias, although we are far away, their love has always been with me. I would like to thank Emmanuel for his love, care and support, especially in this last year of doctorate and, also for his help in translating into French.

Finally I give thanks to God, the creator of the universe, who has given me life and has always taken care of me. He gave me this wonderful project that He put in my heart, the desire to discover his creation. And I also greet his collaborators in this mission, la Mater and Father Joseph Kentenich.

This PhD thesis was sponsored by the Chilean scholarship CONICYT BecasChile.

Contents

Chapter 1

Summary in French

L'Univers est un endroit mystérieux. Depuis le début de l'humanité, nous contemplons le ciel et tentons de le comprendre. Ce qui brille attire notre attention et c'est pour cela que nous étudions les étoiles et le soleil depuis si longtemps. Parmi les objets astronomiques les plus lumineux, les quasars (contraction de "source radio quasi stellaire" en anglais) se distinguent particulièrement. Ils ressemblent aux étoiles mais sont situés à des distances cosmologiques, c'est-à-dire très loin dans l'univers, et leur physique prend place au centre des galaxies. La source d'une telle quantité d'énergie provient du potentiel gravitationnel d'un trou noir supermassif central (supermassive black hole, SMBH, en anglais). Cette très forte luminosité est due à l'accrétion de matière par le trou noir: la matière spirale et forme un disque d'accrétion qui va émettre des spectres de corps noirs à différentes températures. L'émission est fortement variable mais les causes d'une telle variabilité sont encore mal connues. C'est pour cela qu'il est nécessaire d'étudier la variabilité temporelle du signal lumineux dans ce que nous nommons les Noyaux Actifs de Galaxie (active galactic nuclei, AGN, en anglais).

Comme nous l'avons dit, les AGNs présentent une variabilité de flux dans une large bande de longueur d'ondes, de la radio aux rayons gamma. Les AGNs possèdent un spectre continu qui est semblable à une loi de puissance mais sont aussi caractérisés par des raies d'émission intenses, comme les raies des séries de Lyman et Balmer, ou l'émission de raies interdites/semi-interdites (Oxygène, Néon, Carbone ...). Comparativement à une galaxie normale, le noyau d'un quasar est toujours au moins dix fois plus brillant et sa luminosité bolométrique est maximale à une longueur d'onde inférieure: les galaxies ont un pic en émission dans la gamme infrarouge/optique à cause du rayonnement stellaire alors que les AGN ont une forte luminosité en optique/ultraviolet. Ce pic en émission des quasars porte le nom de Big Blue Bump (BBB) et il est précédé par un autre pic, plus faible, en infrarouge à cause de la réémission de la poussière locale. Une quantité importante de rayons X est aussi produite près du coeur de ces objets.

D'un point de vue observationnel, les AGNs sont classées en deux principales catégories: les "type-1" et les "type-2". Concernant les types-1, on observe à la fois des raies d'émission étroites et des raies d'émission larges provenant du cœur du système. Dans le cas des types-2 on observe seulement des raies d'émission étroites qui proviennent des régions polaires étendues. Cette différence est principalement due à l'orientation de l'AGN qui dans un cas offre une vue directe du trou noir

central (type-1) alors que dans l'autre le trou noir supermassif est caché par une épaisse quantité de poussière (type-2) et seuls les vents polaires sont visibles, d'où les raies étroites. Il existe aussi des cas particuliers. Par exemple si l'AGN est relativement faible comparé à l'émission de la galaxie hôte on appellera ces objets des LINERs (Low Ionization Nuclear Emitting Regions en anglais). D'autres AGNs sont appelés radio-forts lorsque l'on est en présence d'une forte émission radio due à un jet de matière relativiste étendu. Les AGNs thermiques sont ceux dont l'émission est dominée par un BBB ("dont le maximum de luminosité est atteint dans le domaine optique-ultraviolet") et les AGNs non-thermiques sont ceux dont l'émission est dominée par des jets qui émettent de la radio aux rayons gamma.

La représentation actuelle des AGNs, déduite d'observations directes et indirectes des structures internes, est la suivante: au centre, le moteur du système est un trou noir supermassif dont la masse se situe entre un million et un milliard de masses solaires. Le disque d'accrétion qui entoure le trou noir est géométriquement mince avec des dimensions de l'ordre de la fraction de parsec. Le disque d'accrétion est responsable de l'émission ultraviolette, optique et infrarouge proche de l'AGN. Dans le même plan équatorial, se trouve la BLR (la Broad Line Region, en anglais), zone d'émission des raies larges à cause de la photo-ionisation puis du phénomène de recombinaison radiative du continuum. La BLR est entourée par une région circumnucléaire poussiéreuse, historiquement appelée tore, qui empêche la détection des raies larges des AGNs de type-2. Toute la structure de la région équatoriale ne mesure que quelques parsecs de large et encore moins de haut. Le tore de poussière va avoir tendance à collimater les éjections de matière dans l'axe des pôles, imposant une géométrie particulière aux vents ionisés qui forment un cône mesurant des centaines de parsecs de long. Ces vents ionisés vont naturellement ralentir et se diluer dans la poussière du milieu interstellaire, donnant naissance à la NLR (Narrow Line Region, en anglais). Comme son nom l'indique c'est la région où sont produites les raies étroites en émission. La NLR peut atteindre une taille de l'ordre du kiloparsec. Enfin, pour les AGN radio-forts, on peut observer des jets relativistes qui se propagent au-delà de la galaxie, sur des distances qui peuvent atteindre l'échelle du mégaparsec.

Cependant, ce schéma n'est que fragmentaire. Nous manquons de contraintes sur les tailles, géométries et compositions des régions les plus internes. Pour aller plus loin dans la compréhension des AGNs nous devons découvrir la structure exacte de la BLR, de la région circumnucléaire et des régions polaires, et surtout, comprendre comment la matière arrive jusque dans ces régions. Nous cherchons à connaître leur composition, à savoir quelle est la distribution spatiale de la poussière, à connaître la géométrie des grains et contraindre les phénomènes physiques impliqués. Malheureusement, nous ne disposons pas encore de télescopes assez grands et puissants, disposant d'une résolution suffisante, pour résoudre les régions les plus profondes des AGNs, régions de la taille d'une fraction de parsec, localisées à des distances de l'ordre de la centaine de mégaparsecs. Nous devons donc trouver une méth-

ode d'observation indirecte afin d'améliorer nos connaissances du modèle théorique des AGNs. Une technique potentielle qui a fait ses preuves par le passé est la polarimétrie, particulièrement si elle est résolue en temps.

A ce jour, la polarimétrie constitue un apport essentiel pour résoudre la complexité des AGNs et contribuer à compléter nos connaissances sur la formation et l'évolution des galaxies. Elle a déjà été, par le passé, la pièce principale qui a permis de proposer un modèle unifié des AGNs lorsque Antonucci and Miller (1985) ont découvert la présence de raies d'émission larges dans le flux polarisé de l'AGN de type-2 NGC 1068. Ils ont alors soutenu l'idée que les types-1 et les types-2 constituaient le même type d'objet, et que l'observation ou non de raies larges de la série de Balmer dépendait de l'angle de vue de l'observateur. Nous comptons donc sur la polarimétrie pour nous donner les clés nécessaires à l'évaluation critique de la géométrie de la région circumnucléaire entourant les trous noirs supermassifs et pour mieux comprendre la structure des AGNs en général.

Cette thèse a été inspirée par la découverte de la cartographie de réverbération de la polarisation dans le cadre des travaux conduit par Gaskell et al. (2012) sur le noyau actif de galaxie NGC 4151. Le but de cette recherche est de modéliser différentes géométries en considérant des mesures de polarimétrie dépendantes du temps, afin de reproduire les cartographies de Gaskell puis de contraindre de futures nouvelles observations. Pour ce faire, nous avons corrélé le flux du continuum avec sa contrepartie polarisée, afin de déterminer la distance réelle (et inobservable autrement) entre la source (le disque d'accrétion) et la plus proche région de diffusion. L'objectif de ce travail de thèse est donc de fournir une réponse théorique au décalage temporel de polarisation induit par les différentes composantes de l'AGN.

Cette thèse est composée de sept chapitres. Le premier est un résumé en français et le second une introduction qui donne une brève description des AGNs. Le chapitre 3 définit les concepts de base de la polarimétrie dans ses représentions mathématiques et décrit les sources de polarisation linéaires les plus adaptées pour cette recherche. Dans le chapitre 4 nous donnons une explication synthétique de l'équation de transfert radiatif, de la méthode de Monte Carlo et du code de transfert radiatif *STOKES*. Le chapitre 5 montre la réponse au transfert radiatif de STOKES pour différents modèles conçus pour les régions internes de l'AGN. Le chapitre 6 présente les résultats de la réverbération en polarimétrie au travers de la fonction de relation croisée appliquée aux modèles étudiés ici. Enfin, le chapitre 7 dresse un état des objectifs qui ont été atteints, détaille les conclusions et aborde les perspectives futures de la polarimétrie de réverbération.

Deux géométries on été modélisées pour la région circumnucléaire avec une section transversale elliptique, appelée "dusty-torus" (en français, tore de poussières) et une autre plus étendue avec une section transversale en forme de coin, le "Flared-disk", disque évasé (fig. 1.1 à gauche, en haut et au milieu). La taille a été choisie

en fonction des contraintes observationnelles pour NGC 4151. Le rayon intérieur est de 0.061 pc (Kishimoto et al., 2013), le rayon extérieur de 15.061 pc et un angle de demi-ouverture de 60° depuis l'axe de symétrie du disque a été fixé (Ruiz et al., 2003). Ces régions ont été testées avec deux types de distribution de la poussière. La première poussière est celle que l'on appelle AGN-dust (AGN-poussière, Gaskell et al., 2004) qui est constituée de 85% de silicates et de 15% de graphites, avec une taille des grains comprise entre 0.005μm et 0.2μm. La seconde poussière testée a été celle que l'on appelle poussière Milky Way (celle de notre propre Voie Lactée), également connue sous le nom de MRN (Mathis, Rumpl and Nordsieck de Mathis et al., 1977). Elle est composée de 62.5% de silicates et de 37.5% de graphites. Nous avons prouvé dans cette thèse que le décalage temporel de l'émission polarisée n'est que faiblement affecté par la modification du type de poussière et donc l'ensemble des simulations subséquentes ont été réalisées avec la poussière de type Milky Way.

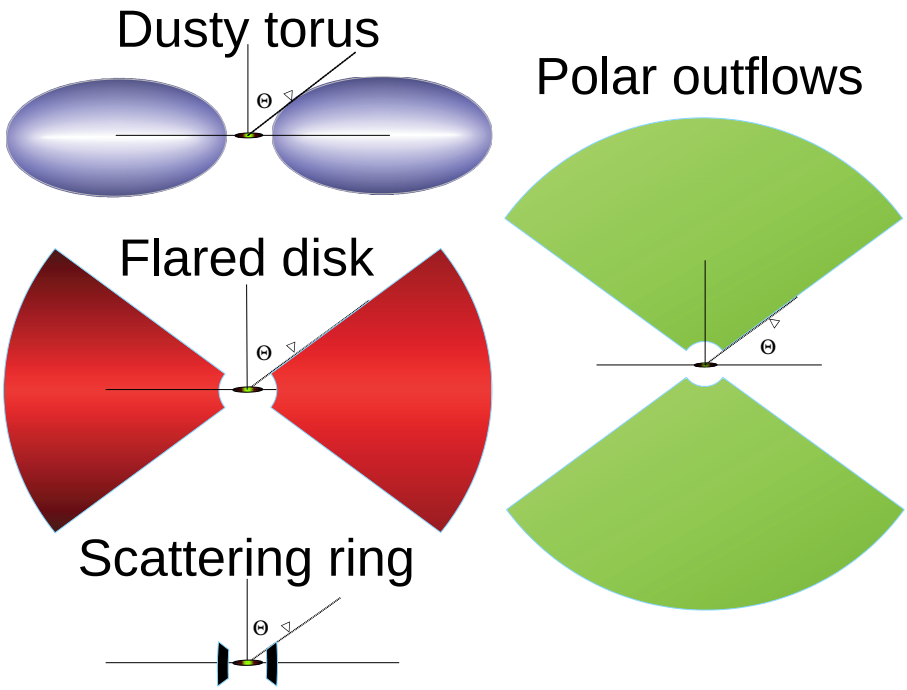

Figure 1.1: Schéma géométrique des modèles. *En haut, à gauche*: la géométrie classique du tore à section transversale elliptique (en bleu). *Au milieu, à gauche*: la géométrie du disque évasé étendu avec section transversale en coin (en rouge). *En bas à gauche*: anneau de diffusion (brun). *À droite*: vents polaire (en vert). (Figure extraite de Rojas Lobos et al., 2018)

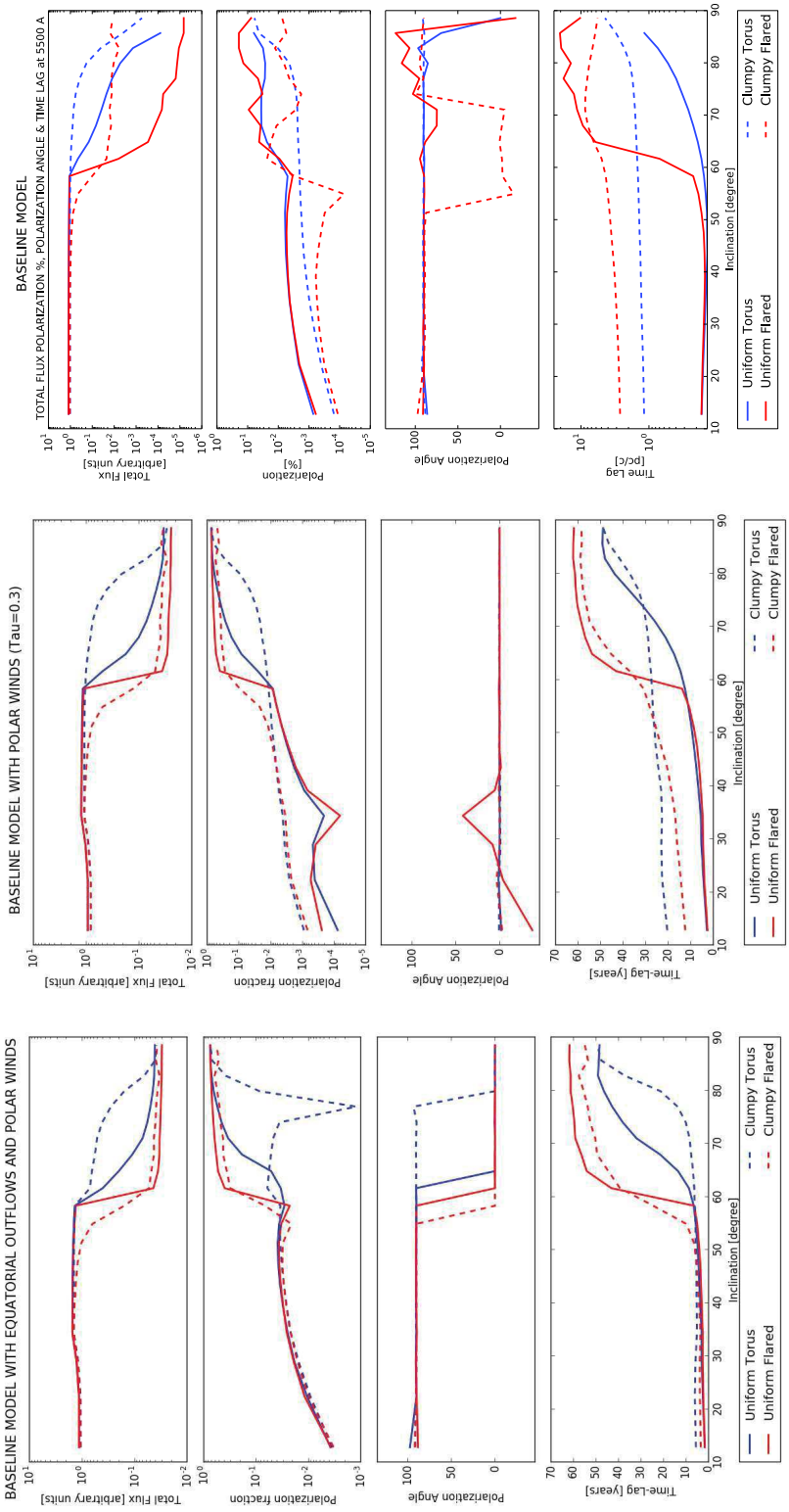

Figure 1.2: Résultat de *STOKES*. *En haut*: modèle de base. *Au centre*: modèle de base avec vents polaires. *En bas*: modèle de base avec vents polaires et anneau équatorial diffusant (Rojas Lobos et al., 2018).

.

Par la suite deux types de distribution de la poussière ont été testés, l'un uniforme, l'autre grumeleux ("Clumpy" en anglais). Les résultats ont montré, pour l'ensemble des modèles, que le décalage en temps augmentait considérablement pour la distribution en grumeaux de la poussière, à cause des effets de multidiffusion entre les différents grumeaux.

La seconde région qui a été testée est celle des vents polaires (Fig. 1.1 à droite), une région entièrement ionisée avec une forme de double cône se situant entre le disque d'accrétion et la région d'émission des raies étroites (NLR). Le rayon intérieur est 0.067 pc et le rayon extérieur est 30.067 pc. Cette région a été testée avec une profondeur optique radiale Thompson de 0.3 et 0.03 (donc optiquement mince). L'addition de cette région à la région circumnucléaire n'a pas d'impact majeur sur les résultats relatifs au décalage du flux polarisé en temps mais il affecte significativement l'angle de polarisation (Fig. 1.2 au centre). Les détails de ces résultats sont précisés dans le chapitre 5.

La dernière région de dispersion testée est l'anneau équatorial diffusant (en anglais, scattering ring) avec une géométrie évasée. Cette région est située sur le plan équatorial entre la zone d'émission du continuum et la poussière circumnucléaire. Cette région correspond à la BLR, elle est également entièrement ionisée, avec une profondeur optique Thomson de l'ordre de l'unité. Le rayon interne de l'anneau équatorial correspond à la distance trouvée par Gaskell et al. (2012) pour NGC 4151 qui est de 8 jours-lumière ($\sim$ 0.0067 pc). Cette valeur est la première à avoir été contrainte par la technique de réverbération polarimétrique. Le rayon extérieur a été fixé à 0.057 pc afin de laisser un espace suffisant entre les surfaces de l'anneau équatorial et de la région circumnucléaire. Lors de l'addition de cette zone aux deux régions précédentes seules les propriétés de la polarisation et le décalage temporel en flux ont été affectés. Cette composante, qui n'absorbe pas les radiations du fait de sa composition, n'a pas d'impact sur le flux total. Cet anneau fixe la polarisation du rayonnement à 90° pour les orientations de type-1 comme observé par Smith et al. (2004). Plus important encore, du fait de la proximité de cette région par rapport à la source centrale du continuum, le décalage en temps observé est plus petit pour des inclinaisons de type-1. Une fraction du rayonnement entrant, en fonction de l'angle solide couvert par l'angle d'ouverture de l'anneau d'électron, est directement dispersée vers l'observateur, induisant un plus petit décalage temporel. Pour de plus grandes inclinaisons, le rayonnement traverse le milieu optiquement mince et se disperse à l'intérieur de la structure de poussière optiquement épaisse. De ce fait, l'impact de l'anneau équatorial devient presque indétectable.

En incluant les vents polaires et cet anneau de diffusion à la région circumnucléaire (Fig. 1.2 en bas), nous aboutissons à des conclusions similaires. En effet l'addition d'un anneau d'électrons équatorial reste marginale en termes de flux total mais favorise l'obtention du degré de polarisation et de l'angle de polarisation qui se stabilisent à des valeurs caractéristiques connues pour les AGNs locaux comme celles

déterminées par des études précédentes (e.g. Marin, 2014). Le degré de polarisation reste au dessous de 1% pour les inclinaisons de type-1 et monte brusquement pour des orientations de type-2. L'angle de polarisation pivote d'une valeur parallèle (90°) à une valeur perpendiculaire (0°) à l'axe de symétrie du modèle lorsque la ligne de visée de l'observateur est masquée par la région circumnucléaire poussiéreuse. Il est important de remarquer que l'anneau équatorial réduit le décalage temporel dans les vues de types-1 par un facteur 5 à 10, ce qui reflète la présence de l'anneau.

Jusqu'ici les résultats polarimétriques qui ont été présentés utilisent une moyenne temporelle obtenue pour différents paramètres tels que le flux total, l'angle de polarisation, le pourcentage de polarisation, le flux de polarisation et le décalage temporel en incluant les phénomènes de multidiffusion et en considérant des surfaces aussi grandes que la région circumnucléaire et les vents polaires. En conséquence certaines valeurs sont élevées du fait du volume des régions étudiées, comme celles relatives au décalage temporel et qui nous intéressent particulièrement. Néanmoins, afin d'obtenir la distance minimum entre les régions d'émission et de réflexion, ce qui veut dire entre le disque d'accrétion et la région de diffusion, il est nécessaire d'appliquer une autre technique: la réverbération. Dans cet objectif, j'ai cherché à établir la corrélation croisée entre la courbe exprimant le flux total de lumière et la courbe exprimant le flux de lumière polarisé.

Pour traiter les données, nous avons tout d'abord utilisé le code *STOKES* en segmentant la modélisation sur plusieurs intervalles de temps, assez petits pour obtenir les distances minimums entre la source et la région de diffusion qu'il nous intéresse de sonder. Afin d'obtenir un traitement des données plus efficace et rapide pour construire des courbes de lumiére, ces dernières n'ont été calculées que pour un seul angle de vue représentatif des AGNs de type-1. Les résultats obtenus correspondent à ceux qui étaient attendus via les observations pour toutes les régions de diffusion prises de manière isolées, ainsi que pour l'ensemble des régions considérées dans leur ensemble (Fig. 1.3). En ne considérant que la seule région circumnucléaire, les valeurs de la corrélation croisée entre le flux total et le flux polarisé sont proches de la valeur théorique du rayon intérieur. L'addition des vents polaires au modèle de base n'affecte pas les résultats tandis que l'ajout de l'anneau équatorial de dispersion diminue fortement la distance minimale.

L'étude du décalage temporel de l'émission polarisée en fonction de l'angle de vue a montré qu'en raison des multiples effets de diffusion le signal polarisé des objets de type-2 est plus en retard par rapport à l'intensité totale que pour les sources de type-1. Une augmentation significative du délai en temps est enregistrée lorsque la distribution de la poussière est grumeleuse. Lorsque l'on ajoute les vents polaires au modèle, le rayonnement diffusé augmente encore davantage le temps de décalage de la polarisation pour les inclinaisons de type-1 car une fraction du flux de photons est diffusé par les électrons (diffusion Thomson) et s'échappe dans les directions polaires. La présence d'un anneau d'électrons équatorial réduit naturelle-

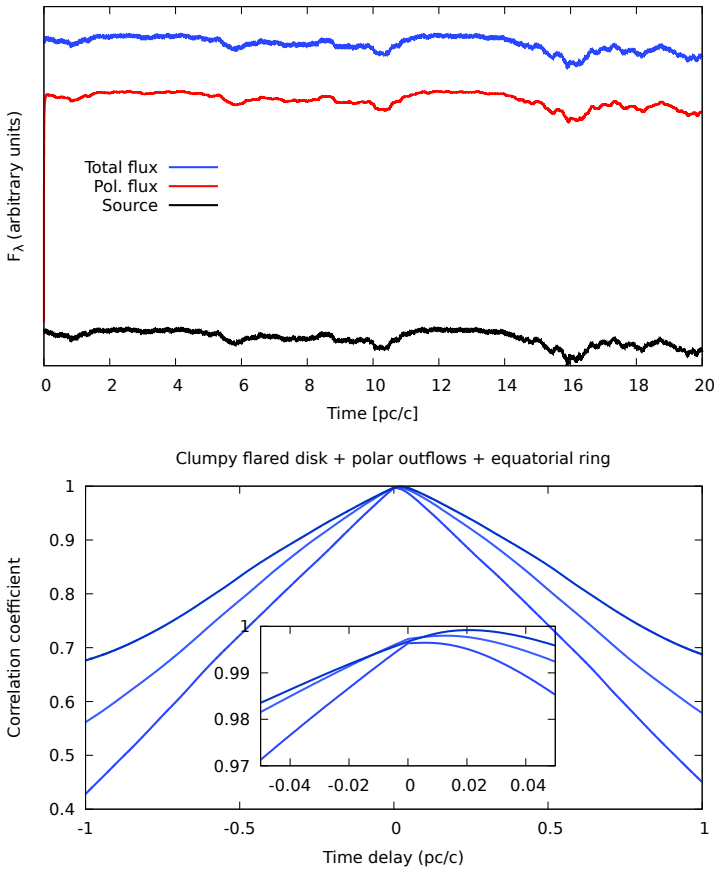

Figure 1.3: Résultat du modèle de base: *En haut*: Courbes de lumière du flux total (en bleu) et du flux polarisé (en rouge). *En bas*: Corrélation croisée.

ment les décalages temporels observés pour les inclinaisons de type-1 pour la même raison déjà expliquée: une fraction du flux de photon est redirigé sur les électrons et s'échappe ainsi en direction des pôles.

Les résultats polarimétriques, qui ont été présentés jusqu'ici, incluent le décalage moyen. Rappelons que cette moyenne est calculée par *STOKES*, en comparant la différence qu'il faut pour atteindre l'observateur entre les photons diffusés et ceux qui arrivent directement de la source. Cela inclut des contributions de régions très différentes. Par conséquent, le décalage temporel obtenu est dû à la moyenne de diffusion sur l'ensemble du volume des régions étudiées. Notez que cette moyenne de décalage dans le temps n'est pas observable, puisqu'il n'est pas possible de déterminer le temps d'émission zéro et même à un angle de vue de type 1, nous voyons également une composante dispersée en plus du flux direct.

Il convient de souligner que, jusqu'ici, nous avons fait référence au décalage ou

au retard dans le temps pour que les photons atteignent l'observateur directement depuis la source et aprés avoir été diffusés. Ceci n'est pas observable. C'est pourquoi dans la suite de cette thèse, nous faisons référence au décalage temporel ou retard dans le temps, correspondant à la différence obtenue par la corrélation croisée entre les courbes lumineuses du flux direct et du flux polarisé. Dans ce cas, cette valeur est équivalente à celle obtenue à partir des observations.

Néanmoins, afin d'obtenir le décalage temporel comparable aux observations et la distance minimale entre la zone d'émission et la zone de diffusion, il est nécessaire pour appliquer la technique de réverbération polarimétrique de construire les courbes de lumière correspondantes et d'établir la corrélation croisée entre ces deux éléments. Pour cela, j'établis donc la corrélation croisée entre la courbe de lumière du flux direct et celle du flux polarisé.

A partir des fonctions de transfert obtenues avec $STOKES$, nous générons les courbes de lumière correspondantes ce qui nous permet de comparer les données d'observation. Puis, nous calculons la différence temporelle entre le flux total (source + polarisé) et le flux polarisé par corrélation croisée, c'est-à-dire la différence de distance parcourue par les photons.

Nous avons constaté que pour les angles de vue de type-1, le temps de retard du flux polarisé est défini par la région ionisée dans l'anneau équatorial, la BLR. Ce dernier devient un polariseur puissant en raison de son angle de diffusion perpendiculaire. Au contraire, les cônes polaires sont surtout visibles en transmission et donc polarisent moins. Ceci nous permet, par la technique de réverbération en polarisation, de déterminer la taille du rayon intérieur du BLR. Il est important de noter qu'il est possible de déterminer les dimensions et les caractéristiques de cette région dans le cadre d'une observation de quelques mois seulement, compte tenu des dimensions moins importantes de la zone étudiée.

Le tableau d'ensemble reste donc complexe et inclut sûrement des dégénérescences qu'il reste à identifier et examiner. Pour cette raison il faudra ensuite effectuer une distinction entre la densité structurelle des flux polaires et le niveau d'agglutination et de répartition des poussières dans le tore. Toutefois, utiliser la polarisation en fonction du temps offre un moyen indépendant pour restreindre les paramètres nécessaires à la modélisation. Pour cela, il est important de combiner le décalage temporel de la polarisation, le degré et l'angle de polarisation et de comparer ces observables aux résultats des différents types de simulation que je présente ici. Les différents tores de poussière ayant une densité uniforme et qui ont été examinés ont révélé que le décalage temporel de polarisation aux angles de vue pour les AGNs de type-1 est légèrement plus grand que le temps mis par la lumière pour traverser le rayon intérieur du tore. La réverbération de la polarisation nous fournit d'importantes informations sismologiques relatives aux AGNs mais il convient, comme pour la polarisation en général, de concevoir une modélisation minutieuse

pour l'interpréter correctement.

La polarimétrie résolue en temps et les développements de cette thèse proposent des contraintes indépendantes sur la structure non résolue (spatialement) des AGNs afin d'optimiser la conception des modélisations et la recherche dans ce domaine. Cette technique d'observation indirecte peut également être utilisée dans d'autres domaines d'étude en astrophysique portant sur des objets non résolus.

Chapter 2

Introduction

The Universe is full of mysteries to be discovered. Since the beginning of time humanity has contemplated the sky and has marveled at what it sees and has always tried to understand. The shiny things catch our attention, the stars at night, the Sun during the day. A supernova, the explosion of a star liberating a tremendous amount of energy, is responsible for the formation of the heaviest elements. One of the brightest objects in the astrophysics context are the Quasars, their name deriving from "quasi-stellar radio source". They look like stars but are found at cosmological distance in the center of some galaxies. The source of huge amount of energy is the gravitational potential of a Super Massive Black Hole (SMBH) found at the galaxy center. High luminosity levels are then due to accretion of matter falling on to the black hole (BH) that eventually will form an accretion disk (AD) that will emit blackbody spectra at different temperatures. This emission is highly variable but the causes of such variability are still poorly known. This is why it is necessary to study the temporal variability of the light signal in what we call the Active Galactic Nuclei (AGN).

The current representation of AGNs, derived from direct and indirect observations of internal structures, is as follows: in the center, the system engine is a super massive black hole whose mass lies between one million and one billion solar masses. The accretion disk that surrounds the black hole is geometrically thin with radial dimensions of the order of a fraction of parsec. The accretion disk is responsible for the ultraviolet, optical and near infrared emission of AGNs. On the same equatorial plane, and perhaps as an accretion disk release, there is the Broad Line Region (BLR), the emission zone of broad lines due to photo-ionization by the continuum followed by radiative recombination. The BLR is surrounded by a dusty circumnuclear region, historically called the torus, that prevents the detection of broad lines in type-2 AGNs. The whole structure of the equatorial region is only a few parsecs wide and even less than that in height. The dust torus will tend to collimate ejections of matter in the poles axis, forcing a particular geometry to the ionized winds which form a cone measuring hundreds of parsecs long. These ionized winds will naturally slow down and dilute with dust from the interstellar medium, giving rise to the Narrow Line Region (NLR). As its name indicates, it is the region where narrow lines are emitted. NLR can reach a size in the kilo-parsec range. Finally, for radio-loud AGNs, we can observe jets of relativistic matter that propagate beyond the galaxy, over distances that can reach the mega-parsec scale.

However, this view is only a fragment. We lack constraints on size, geometry and compositions of the most internal regions. To go further in the understanding of AGNs we must discover the exact structure of the BLR, the circumnuclear region and the polar regions, and especially understand how matter reaches these regions. We seek to know their composition, to know what is the spatial distribution of dust, to know the geometry of the grains and to constrain the physical phenomena involved. Unfortunately we do not yet have large and powerful enough telescopes with sufficient resolution to observe the deepest regions of AGNs, regions the size of a fraction of parsecs located at distances of the order of a hundred mega-parsecs from us. We must therefore find an indirect observational method in order to improve our knowledge of the theoretical model of AGNs. A potential technique that has proven useful in the past is polarimetry; in particular time resolved polarimetry could be especially useful.

Nowadays, polarimetry constitutes an essential contribution to solve the complexity of AGNs and contribute to improve our knowledge in galaxy formation and evolution. It was already the main method which made possible the proposal of a unified AGN model when Antonucci and Miller (1985) discovered the presence of broad emission lines in the polarized flux of the AGN type-2 NGC 1068. They then supported the idea that types-1 and types-2 constituted the same type of object and that whether one observes or not Balmer series broad lines depended on the viewing angle of the observer. We are therefore counting on polarimetry to give us the key data needed to critically evaluate the geometry of the circumnuclear region surrounding the supermassive black holes and to better understand the structure of AGNs in general.

This thesis was inspired by the discovery of polarization reverberation mapping in the work conducted by Gaskell et al. (2012) on the active galaxy core NGC 4151. The goal of this research is to model different geometries by considering time-dependent polarimetry measurements in order to reproduce Gaskell's maps and then compare the results of our models with future new observations. To do this, we correlated the flow of the continuum with its polarized counterpart in order to determine the real (and otherwise unobservable) distance between the source (the accretion disk) and the nearest scatter region. The objective of this thesis work is therefore to provide a theoretical response to the polarization time lag induced by the different components of AGN.

This thesis is composed of seven chapters. The first is a French summary, the second is an introduction that gives a brief description of AGNs. Chapter 3 defines the basic concepts of polarimetry in its mathematical representations and describes the most suitable linear polarization sources for this research. In Chapter 4 a synthetic explanation of the radiative transfer equation, the Monte Carlo method and the *STOKES* radiative transfer code is given. Chapter 5 presents the radiative transfer response from *STOKES* for several models designed for the inner regions

of AGN geometries. Chapter 6 shows the result for reverberation in polarimetry using the cross-correlation function applied to the models studied here. Finally, Chapter 7 reviews the objectives that have been achieved, explains the conclusions and discusses future prospects for reverberation in polarimetry.

2.1 The discovery of Active Galactic Nuclei

Active Galactic Nuclei (AGN) were discovered in the optical waveband by Carl Seyfert who was the first to describe high and compact sources of optical luminosity at the center of what at the time was known as spiral nebulae (Seyfert, 1943). He conducted spectroscopic observations of six objects at the Mount Wilson Lick Observatory. The sources he observed were NGC 1275, NGC 3516, NGC 4051, NGC 7469, NGC 1068 and NGC 4151. An important characteristic Seyfert observed in most of these objects was strong broadened emission lines. The hydrogen lines sometimes appeared broader than other lines. With the development of radio-astronomy, in the 1950s the first catalogues of radio sources appeared. They made it possible to systematically relate radio sources to optical observations. Back then, many radio sources appeared as unresolvable bright stars and such objects were baptized Quasi Stellar Radio Sources (QUASARS). In 1969, Maarten Schmidt made spectrometric studies of a comprehensive number of quasars and found large ultraviolet (UV) fluxes and broadened emission lines (Schmidt, 1969). He realized that the Balmer emission lines series was redshifted. Interpreting this redshift as the effects of cosmological expansion of the Universe, he proved that quasars are extragalactic objects.

AGN present optical flux variability, a characteristic set of emission lines (intense Lyman and Balmer series, forbidden Oxygen and Neon, semi-forbidden Carbon, etc) and a more or less characteristic continuum spectrum that can be roughly described by a power law shape. Compared to normal galaxies, the nucleus of Quasars is at least ten times brighter, with most of this luminosity peaking at higher wavelengths in comparision to normal galaxies for which the major contribution comes from stars and is centered in the optical range. With increasing telescope power, more and more AGN could be actually identified as the central components of galaxies. The fact that these galaxies have very high luminosity originating from a small region at their center coined their denomination as Active Galactic Nuclei. They represent the most luminous compact steady sources in the Universe and the mechanism to produce so much power remained a riddle for a long time. After the development of astronomical instrumentation covering the entire electromagnetic spectrum and decades of observation, we know today that AGNs emit from radio to γ-rays, and with a characteristic Spectral Energy Distribution (SED) (Fig. 2.1).

2.2 Observational features of AGN

As described before, AGNs are high luminosity point sources at the center of massive galaxies (Kormendy and Richstone, 1995; Silk and Rees, 1998; Kauffmann et al., 2003). The source of the observed optical light cannot be explained by radiation of stars and its high variability implies that it is emitted from a small central source. The only explanation we have at the moment to this concentration of energy is the presence of a super massive black hole surrounded by orbiting material which forms the accretion disk (Pringle et al., 1973; Shakura and Sunyaev, 1973). The foremention disk is extremely efficient in converting mass in to energy (Hoyle and Fowler, 1963; Salpeter, 1964; Lynden-Bell, 1969; Shields, 1978) (see sub-section: 2.3.1). Broad lines are also observed, these show us high speeds and indicate densities over 10^6 cm^{-3} for its components when located close to the center. On the contrary, narrow lines indicate lower speeds and a much less dense environment since they are emitted farther away from the center. In the same way the line profiles we observe in different wavebands tell us about different physical processes and different regions.

From an observational point of view, AGNs are classified into two main categories: "type-1" and "type-2". For type-1, both narrow and broad emission lines are observed. In the case of type-2, only narrow emission lines from the extended polar regions are observed. This difference is mainly due to the orientation of the AGN that in one case offers a direct view of the central black hole (type-1) while on the other hand, the supermassive black hole is hidden by a thick amount of dust (type-2) and only the polar winds are visible, hence the narrow lines (Antonucci, 1993). There are also special cases, for example, if the AGN luminosity is relatively faint compared to the emission of the host galaxy, these objects are called LINERs (Low Ionization Nuclear Emitting Regions). AGNs are called radio-loud when one is in the presence of a strong radio emission due to an extended relativistic jet. Thermal AGNs are those whose emissions are dominated by the big blue bump (BBB), whose maximum luminosity is reached in the optical-ultraviolet range, and non-thermal AGNs are those whose emissions are dominated by radio jets which emit from the radio to the gamma rays (Beckmann and Shrader, 2012).

2.2.1 The central engine

Using Newtonian physics is quite difficult to explain how luminosity as large as thousands of million of stars concentrated in a sphere with a radius not larger than 1 pc can be produced. The first indication of how small the central region is comes from variability studies, that has been observed since the very beginning (Smith and Hoffleit, 1963) and provides sizes of the order of light-days for the emitting source. In this dilemma the idea of a black hole, a massive object as engine of the system, was born.

The typical luminosity of AGNs is between 10^{44} and 10^{46}erg s^{-1}. Using the virial theorem (Woltjer, 1959), it was concluded that the mass of the source must be of the order of 10^8 solar masses. Woltjer (1959) also postulated that the degree of ionization should be higher in the center than outside the nucleus. He investigated the possibility that the continuum observed in active nuclei was coming from stars, but he came to the conclusion that the continuum is produced by another mechanism such as synchrotron radiation or Bremsstrahlung.

Looking at a different scenario, Hoyle and Fowler (1963) considered the existence of a very high mass stellar object surrounded by a disk of gas. Salpeter (1964) studied the characteristic of the accretion process by massive objects. The spectral profile in the visible and UV bands indicates the presence of a disk with an inner part that is warm and emits in extreme UV or soft X-rays. The outer and cooler part of the disk emits in optical and, in the intermediate region, in UV. The AGN thermal emission has its maximum in the UV regime (Peterson, 1997).

The characteristic of the Newtonian disk was studied by Shakura and Sunyaev (1973). In their work, they introduced the viscosity parameter α which is responsible for angular momentum transport in the accretion disk and heating by friction of the gas. They described the disk viscosity v by the approximation $v = \alpha c_s h$, where c_s is the speed of sound and h represents the height of the disk. The α parameter is a dimensionless quantity between 0 and 1. The emission in the disk can be represented by concentric rings of increasing radius and responsible for the different peaks in emission at different wavelengths according to the temperature at a given radius. For circles closer to the center, the temperature is higher with emission in the UV regime, while cooler outer regions of the disk emit in the optical regime. The effective temperature of each ring is given by:

$$\sigma T^4 = \frac{3GM\dot{M}}{8\pi R^3}\left[1 - \sqrt{\frac{R_{in}}{R}}\right] \tag{2.1}$$

where R_{in} is the inner radius of the disk, R the ring radius and $\dot{M}$ is the accretion rate (Beckmann and Shrader, 2012).

2.2.2 X-Ray emission

X-rays represent 10% of the bolometric luminosity of AGN and one of their most distinctive signature is the presence of an iron Kα lines in a large fraction of type-1.5 (intermediate type of AGN, where the broad and narrow components of Hβ line are comparable). The broadening of the lines is in the range of over 10.000 km s^{-1}. This feature is attributed to cold matter that could be in the form of an accretion disk in close vicinity of the black hole (Mushotzky et al., 1995).

It is possible to distinguish four components in X-rays emission: a power-law continuum due to thermally comptonized soft photons, a soft excess at low energy,

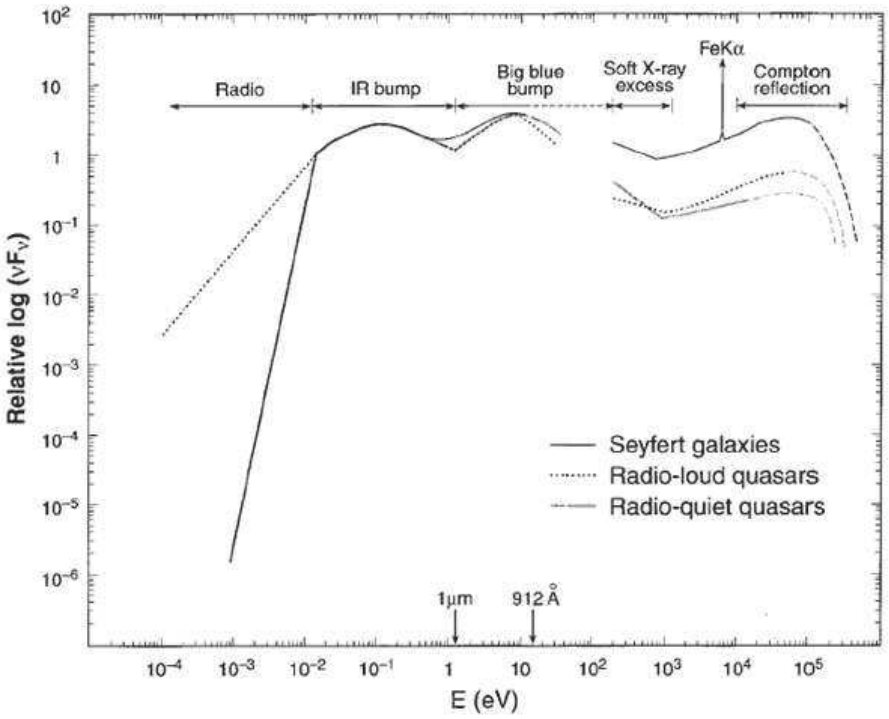

Figure 2.1: Scheme of AGN spectral energy distribution (from Koratkar and Blaes, 1999).

recombination of a Kα iron line and a Compton hump produced by the reflection of X-rays on the disk (Jovanović and Popović, 2009). Soft X-rays excess are thought to be produced on the disk itself and by recombination (Gardner and Done, 2014).

On the other hand, in radio-loud AGN, the X-ray emission is dominated by jets, which are characterized by a high speed, and very collimated beams travel in both directions along the polar axis depending on the accretion disk's angular momentum. The jets are abundant sources of X-rays. Soft X-rays are generated when they reach the peak in synchrotron emission. X-rays and gamma-rays are generated from the interaction between the synchrotron radiation and ultra-relativistic electrons.

2.2.3 Optical-UV line emission

One of the most important optical features observed in AGNs is broad emission lines with widths of over 1000 km s^{-1}. The Balmer lines usually show much larger widths when compared with the forbidden lines as mentioned by Seyfert (1943). Even if the spectra and the width of the lines vary from object to object, in general strong Balmer lines are observed in Seyfert-1 (H$\alpha\lambda$6563, H$\beta\lambda$4861 and H$\gamma\lambda$4340) as well as Hydrogen $Ly_\alpha\lambda$1216 and forbidden [OIII]. Some of them also show MgII, H, K lines of CaII, OI, NII (Rubin and Ford, 1966, 1968). The width of the lines

indicates speeds over 1000 km s^{-1}, from a region close to the black hole and with a distance between 0.01 and 0.1 pc. The region where those lines are produced is known as the Broad Line Region (BLR). Many models have been proposed (see 2.3.4) to try to explain this region, but it is still a puzzle. Although the lines give us information about density, ionization and location of emissions, the inner radius, the BLR composition and its geometry are not known yet.

Narrow lines are emitted farther away from the nucleus than the BLR. The full width at half maximum (FWHM) of the lines varies from 200 to 900 km s^{-1} and the dust that forms this narrow line region is optically thin as suggested by the presence of forbidden lines. The dust torus tends to collimate the ejection of matter in the axis of the poles, forcing a particular geometry to the ionized winds which form a cone measuring hundreds of parsecs long. These ionized winds will naturally slow down and dilute with dust from the interstellar medium, giving rise to the NLR. It was the first AGN region that has been resolved by direct observation. The line profile also reflects different levels of ionization (see sub-sections: 2.3.4 and 2.3.6).

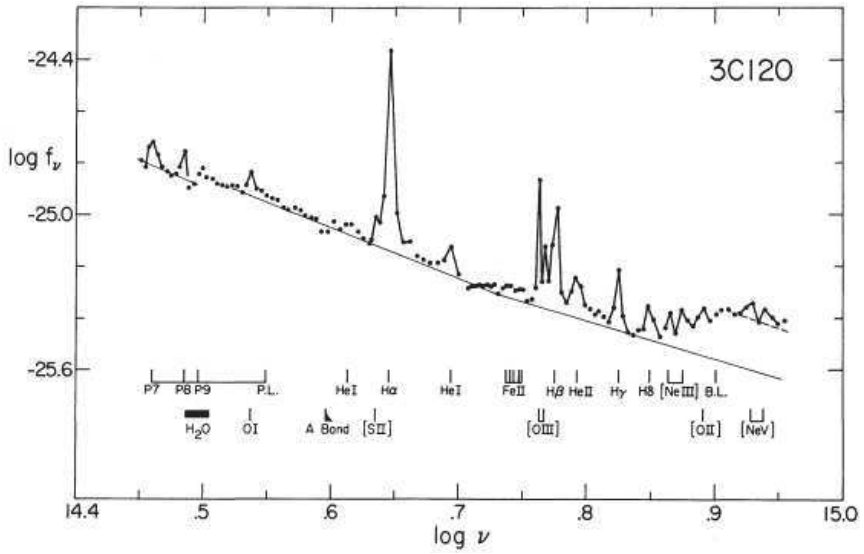

Figure 2.2: Plot of flux in function of wavelength for AGN 3C 120, some Balmer, forbiden and iron lines are shown from Shields et al. (1972).

A good example of the diversity of lines in one object is the optical spectrum observed for the Seyfert galaxy 3C 120 (Fig. 2.2), also known as PKS0430+05 (Shields et al., 1972). Older studies of this object indicate a radio source having a diameter less than 0.3 pc. Shields et al. (1972) found a FWHM around 300 km s^{-1} for forbidden lines, 2000 km s^{-1} for Hβ and 3000 km s^{-1} for HeIλ5876, and HeIIλ4686 appears around 8000 km s^{-1}. The set of emission lines observed in this publication are: [NeV], [OII], [NeIII], Hε, Hδ, Hγ, [OIII], HeI, HeII, Hβ, [SII], OI,

[FeII]. The presence and the width of the lines is a big source of information, i.e. temperature, velocity, and density of the central region of AGNs. For example, Shields et al. (1972) discovered that at least two regions can be identified: the first is where the forbidden lines are produced, here they deduced an effective temperature $T_e \sim 2\text{x}10^4$ K, $N_e \sim 10^3$ cm^{-3}, and a mass of the order of 10^4-10^5 solar masses. The other region, is where the broad and permitted lines are produced, which have $T_e \sim 6000$ K, $N_e \sim 10^8$ cm^{-3}, and a mass ≤ 200 solar masses. In fact, the strong [OIII]λ5007 line depends on the mass of the central BH (see sub-chapter: 2.3.1). Much more forbidden and narrow lines are observed in the near-infrared emission spectrum.

2.2.4 Radio emission

Since the first observations, radio emission has been associated to the activity of AGN. Radio emission is produced when jets of plasma are launched from the vicinity of an accretion disk in both polar directions along the axis. The core of the radio emission is situated at the center of the AGN, while the brightest parts of the radio flux are located in the lobes of the jets found at several tens of kilo-parsec from the center, in regions where the jets interact with the intergalactic medium. There are objects where jets can reach distances of the order of a mega-parsec (Liu and Zhang, 2002), as the giant radio source J2345-0449 which extends up to ~ 1.6 Mpc (Bagchi et al., 2014). In general, the radio energy is generated by synchrotron radiation from relativistic electrons and free-free emission in HII regions. There exists an empirical correlation between radio and X-ray emissions that suggests that the accretion flow is connected with the radio emission [Panessa et al. 2007].

2.2.5 IR emission

Note that the IR SEDs in AGNs also have a component from star formation (SF) from the host galaxy. IR emission is almost always related to dust. The temperature of the NIR and MIR dust emission is in the range of 100 to 2000 K, the size of the region emitting at this temperature is in average around 1 pc and is the product of a secondary dust emission. The primary emission is due to the accretion process (see sub-section: 2.3.2), while the secondary emission is due to dust grains in the torus heated by the primary radiation source. The dust is located in the circumnuclear region usually named torus, and the broad and narrow lines observed in IR are found in the BLR and NRL respectively. IR excess in emission is observed in AGNs, apparently its origin is thermal. The UV and optical photons emitted by the disk heat the dust and generate the IR emission. The dust is composed by grains of graphite and silicates, the average dimension is of the order of 0.1 μm. This is close to optical and UV wavelengths. The scattering and absorption become more efficient when the dust size is comparable with grain size, that is in the regime of $2\pi/\lambda$, therefore dust is responsible for extinction and reddening for those frequencies.

The torus is responsible for the obscuration phenomena in the central region of AGNs. In AGNs, the dust distribution is not isotropic and is concentrated in the equatorial region. This region cannot be well resolved; although some nearby sources have been observed recently by VLT interferometry, their geometry, distribution dynamic, composition and formation of the dust in the inner region of AGNs are still unknown.

2.2.6 Absorption lines

Some of the absorption lines observed in AGNs come from the intergalactic medium plus local ISM; for that reason, it is important to have a good model to remove the contamination by the host galaxy. Just as for emission lines, absorption lines can be observed in X-ray, UV-optical and IR, and can be broad (BAL) or narrow (NAL). X-ray observation show highly ionized gas (HIG) that is usually associated with a region of strong absorption, the so-called warm absorber (WA). The most common absorption lines observed in QSO (Quasi Stellar Object) are Lyα, CIV, MgII; CII, SiIV, MgI and FeII are also detected. In rare cases CaII and in a few QSO the 21 cms HI has been detected in absorption. Sometimes, broad absorption lines are observed in QSO, known as BAL system. They are usually dominated by high-ionization elements like CIV, SiIV an NV, there are however other QSO where low-ionization lines, such as MgII, AlII, AlIII and CII are dominant. The intrinsic absorption lines are an evidence of gas outflows in AGNs.

2.2.7 Continuum variability

The variability is a strong characteristic of AGNs and it is observed at all wavelengths. Its small scale, from days (Ponti et al., 2012) to years (Middei et al., 2017), was the first indication of the small size of the emitting region and of the presence of a SMBH. For size determination, only the short-term variability is important. The variability time scale varies from object to object but there are in general correlations between optical, UV and IR. With X-ray the correlation is less clear (Nandra, 2001). It is an invaluable property that allows us to discover the size of the different emission regions, for example the size of the BLR using reverberation mapping (see subsection 6) when one uses the cross-correlation between continuum and Balmer lines.

For radio-quiet AGNs, the variability observed in optical and UV band is most probably due to fluctuations of direct disk thermal emission plus scattered emission. In AGNs, the blue bands have higher variability than the red bands, which is consistent with the idea that the optical continuum is produced by thermal emissions from the disk, whereas longer wavelengths come from the outer regions of the disk, that are cooler. The IR variability should originate from different regions such as the outer part of the disk. However, not all observations are consistent with this

picture, as some objects show a different scale of variability. Lira et al. (2011) for example reported in the case of NGC 3783 differences in the correlation analysis shown by the near IR band J with respect to the H and K bands, which suggests in their opinion that the emission in the J band comes from the disk, while the emission in the H and K bands comes from the torus.

In the case of radio-loud AGNs, variability is highly dominated by fluctuations in the relativistic jets. The variability from optical to radio bands is due to synchrotron emissions generated by the interaction of relativistic particles of the jets and the magnetic field of the AGN engine. The hard X-rays and γ-rays are most probably due to Compton scattering (Beckmann and Shrader, 2012).

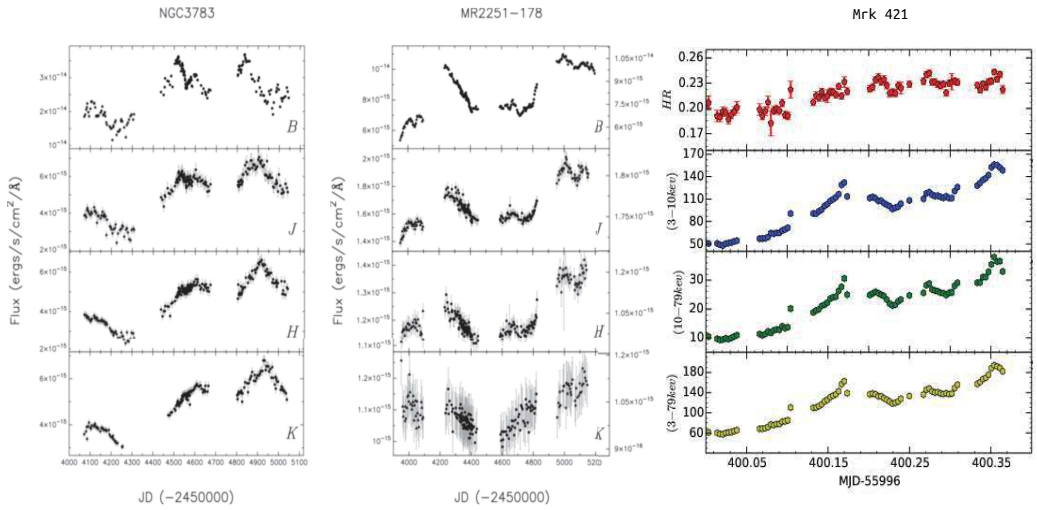

Figure 2.3: Variability Light curves. *Left and center:* near-IR and optical B-band lights curves for NGC 3783 and MR 2251 from Lira et al. (2011). *Right:* X ray light curves for Mrk 421, H R, hard and soft X ray flux variations from Rani et al. (2017)

Fig. 2.3 shows examples of variability in light curves. On the left and in the center, an example of long term variability in the near IR from Lira et al. (2011). On the right, the light curve of Mrk 421 is shown in X-ray bands, with variability in short term; this figure is from Rani et al. (2017), who in this study found ranges of variability less than 10 minutes in 11 sources.

2.2.8 Mega maser emission

With the development of millimeter and sub-millimeter arrays it became possible to detect masers (microwave amplification by stimulated emission of radiation). These phenomena are based on the stimulated emission enunciated by Albert Einstein in

1916. Masers consist of stimulated emission of a photon when it interacts with a molecule in a high energy state that comes back to its lowest level and emits a photon of the same energy as the initial one. Usually, the lifetime for the photon emission is small (10^{-8} s), but there are processes where the lifetime is longer (10^{-3} s). These states with long lifetime are called metastable and are fundamental to produce a maser. The lifetime plus the resonance of the photon chain reaction generate a beam that is extremely focused and coherent. This light amplification is observed in nature. In the astrophysical context, it is observed in interstellar space with molecules such as water (H_2O), hydroxyl radicals (OH), formaldehyde (CH_2O), methanol (CH_3OH) and silicon monoxide (SiO). In AGNs, extremely powerful masers that are 10^6 times more luminous than stellar masers are observed. They are known as mega-maser. In the iconic Seyfert-2 NGC 1068, Wang et al. (2014) found SiO and CH_3OH masers that are both located near the center of the AGN. They argue that the SiO mega-maser originates from the nuclear disk, while the CH_3OH mega-maser originates from shock fronts. Nowadays mega-masers have been observed in hundreds of AGNs and are found in a large molecular disk at a distance of about 0.1pc. Today, mega-masers are the most accurate direct measurement enabling the determination of the mass of the SMBH and the distance to the source.

2.3 AGN structure and the unified model

As explained in the previous section, there are different regions responsible for the AGN continuum emission and for the emitted and absorbed lines. Figure 2.4 shows the AGN SED together with the various emission processes involved and the associated emission region. The SED in AGNs is the result of contributions from AD, Compton emission, BELs and narrow emission lines (NELs) and dust emission can originate from two sources, one probably due to the heat of the AGN itself and a second one possibly due to star formation from the host galaxy (Beckmann and Shrader, 2012).

Initially the classification was based on observational characteristics. One of the most important one was the presence or lack of broad emission lines in Seyfert, leading to the type-1 and type-2 classification, respectively. However, Antonucci and Miller (1985) discovered the presence of broad emission lines in the type-2 NGC 1068 in polarized flux, and they argued that type-1 and type-2 are the same type of objects: the detection of the broad Balmer lines depends on the observer viewing angle. This was the initial nudge to the Unified Theory and also implies that AGNs are anisotropic emitters.

Nevertheless, there are also AGNs that defy the unified model and need additional mechanisms to be explained. Such is the case of the AGNs with changing-look. They show high brightness variability and changes in the width of broad lines, so

high that in some cases the broad lines disappear, going from a classification type-1 to type-1.9 or type-2. It is not possible to attribute this change of look to the inclination change of the AGN, as they occur in a short period of time. Although there is still no definitive answer for this characteristic, some signs begin to appear on the road to understand them. Marin (2017), with optical polarimetry, was able to confirm that in the changing-look J1011+5442, the disappearance of the broad lines is due to a change in the accretion rate of the disk. In a recent publication, Yang et al. (2018) has identified 21 new changing-look AGNs with data from various catalogues such as SDSS and WISE to mention a few. The study of changing-look as well as AGNs in general continue to be an area of active scientific research.

The actual picture of an AGN is as follows: at the center and as the engine of the system is a SMBH, which is a black hole with a mass between 10^6 $M_\odot$ and 10^9 $M_\odot$, and a size of the order of million to billion of kilometers. Surrounding the SMBH there is an accretion disk formed by material that is attracted by the SMBH: the disk is flat with radial dimensions of the order of a fraction of a parsec and is the source of the high optical luminosity. Close to the equatorial plane there is the BLR, responsible for broad lines, surrounded by the circumnuclear region, historically named torus and responsible for the obscuration which hides the broad lines in type-2 Seyfert. All these structures are within a few parsecs from the center. In the polar region there is a cone of ionized electrons just reaching a few parsecs followed by the narrow line region (NLR) that, as its name indicates, is where the narrow lines are produced. This region is of the order of a kilo-parsec in size. Some AGNs show jets that extend beyond the galaxy, with scales of several tens of Mpc. The not-to-scale actual scheme of the AGN was presented by Marin (2016) and is shown in Fig. 2.5.

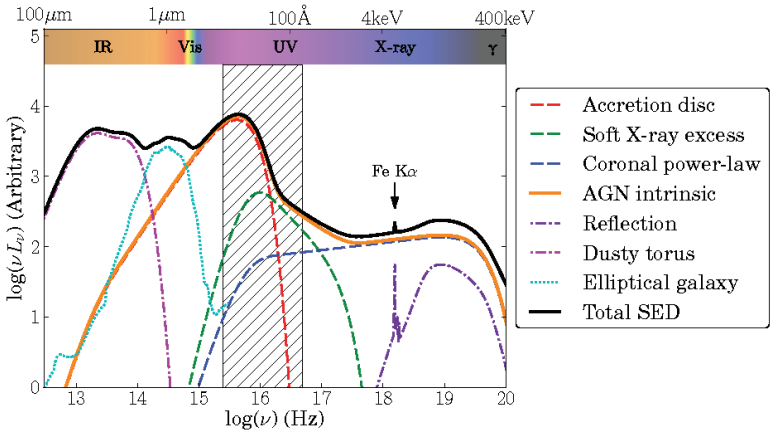

Figure 2.4: Scheme of AGN spectral energy distribution and the different region associated with the emissions, from Collinson et al. (2017)

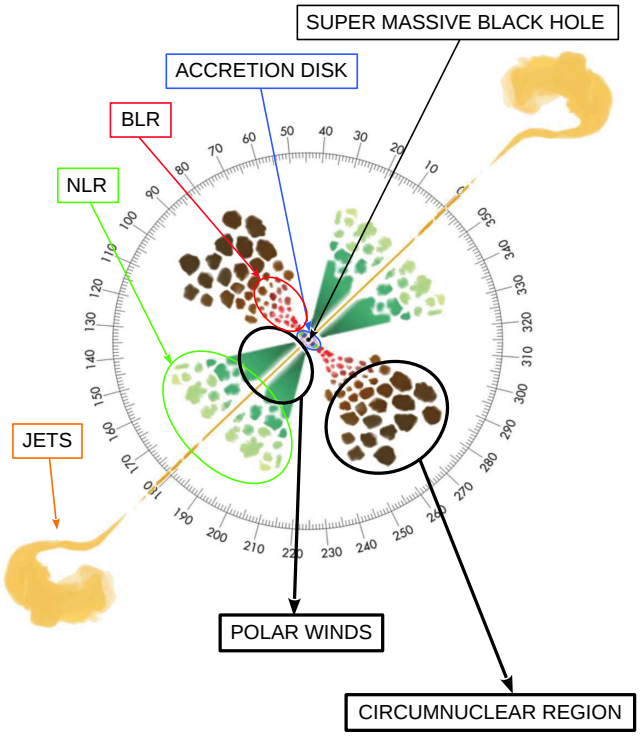

Figure 2.5: Scheme of AGN structure from Marin (2016)

2.3.1 Black hole

A black hole is a singularity in space time surrounded by an event horizon. It is not possible to see it directly because its strong gravity pull does not allow for light to escape from its center. However, we know about their existence thanks to the impact they cause in the nearby regions. A BH is characterized by only three pa rameters: mass, spin and charge.

Einstein developed the theory of general relativity, which predicts the formation of black holes when an compact enough mass deforms space time (Einstein, 1915b,a, 1916). In 1916, Karl Schwarzschild using the general relativity equation, discovered the minimum distance from a BH where matter is not absorbed by it, known as Schwarzschild radius, and defined the 'event horizon' (Schwarzschild, 1916). In 1930, at the age of 19, Subrahmanyan Chandrasekhar calculated the possible mass limits for a white dwarf to collapse and become a black-hole or a neutron star (Chandrasekhar, 1931), this equation is now known as Chandrasekhar limit.

There are four types of BH that are derived from the solution of the Einstein field equations and are named according to the metric that solves them: Schwarzschild for not rotating and not charged BH, Kerr for uncharged rotating BH, Reissner-Nordström for charged not rotating BH, and Kerr-Newman for charged and rotating BH. Charged BHs do not exist in nature.

BHs with masses of a few solar masses are formed by the collapse of massive stars. However, the SMBH, whose mass exceeds 10^6 solar masses, cannot be formed by the collapse of one star. Their origin is unclear, they might be primordial, or be the result of many mergers of BHs that were formed in the early universe, in any case, their growth by accretion is too slow to account for the observed masses. In 1974 Stephen Hawking argued that because of quantum effects, they should emit thermal radiation as a black-body and in effect they lose mass; however, the emission is proportionally inverse to the mass. For stellar mass BHs, the evaporation time is by far longer than the age of the Universe (Hawking, 1974).

2.3.2 Accretion disk

Most of the optical and UV emission, as well as a fraction of IR originates from the accretion disk (AD). After having analyzed the IR, optical and UV emissions of six quasars, Malkan (1983) concluded that the best fit for the observation is an optically thick accretion disk. However, several models of accretion disks have been proposed and still there is no consensus. The classical or standard model refers to Shakura and Sunyaev (1973) and describes a geometrically-thin optically-thick disk by hydrodynamic equations in the radial direction. In the z-direction, one assumes equilibrium between the gravitational force and the pressure gradient. Viscosity, that transports angular momentum, is generated by the magneto-rotational instability (Balbus and Hawley, 1992). Another model is the theory of geometrically thick flows. In this model, Narayan and Yi (1995), describe the accretion flow as a two-temperatures plasma which is cooled by Bremsstrahlung, synchrotron and comptonization. This solution is hotter than the standard model. It is optically thin and is viscously and thermally stable. This model is also known as Advection Dominated Accretion Flows (ADAFs). Originally, the problem with this model was to explain how a geometrically thin cool gas can generate such a flow; today one possible answer is the evaporation instability (Done, 2010). When a hot flow interacts with a cold disk, there is thermal conduction between them. It can happen in two ways: evaporation of the disk, and condensation of the flow. An eccentric accretion disk was proposed by Lyubarskij et al. (1994). They derived the equation for a non stationary viscous accretion disk in which particles are orbiting along Keplerian ellipses that drift and are slowly carried to the center. The variability, in this global model, is the product of the variability at different radii, considering a fluctuating α (viscosity parameter) for different radii. The energy released by viscous dissipation

is transported by advection processes.

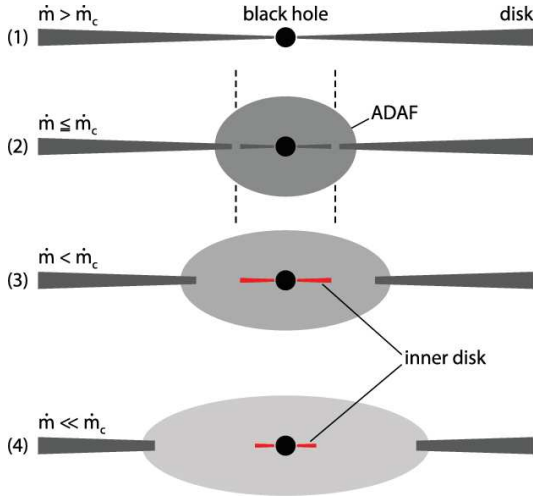

Figure 2.6: Scheme of the accretion flow as a function of accretion rate $\dot{m}$, where $\dot{m}_c$ is critical rate for which the state transition happens (Meyer-Hofmeister et al., 2009). This is an adaptation of Esin et al. (1997).

For all models, the most important settings are the viscosity parameter α and the accretion rate $\dot{m}$. The temperature of the disk increases as the radius decreases, until it reaches the innermost stable circular orbit (ISCO) and the predicted spectrum is the sum of a multicolor blackbody. However, the AD SED is more complex and, for example, hard X-rays and soft x-ray excess are not well understood and should be related to the corona (see the following sub-section). In Fig. 2.6 we show a scenario from Meyer-Hofmeister et al. (2009), with different geometries depending on the accretion rate $\dot{m}$.

2.3.3 Accretion disk corona

The presence of soft (E$<$ 10 Kev) and hard ($>$ 10 Kev) X-ray emission in the accretion disk surrounding the stellar mass BH of Cyg X-1 was studied in detail by Liang and Price (1977). They suggested that the AD pumps energy into its upper atmosphere to form a high temperature corona as observed in the sun. In AGN two types of flows might coexist, optically-thick and geometrically-thin accretion disk, plus vertically-extended, optically-thin, geometrically-thin flows (Meyer-Hofmeister et al., 2017). The presence of X-ray reflection is a sign that the corona is cooled by Compton scattering of photons emitted by the inner region of the AD. Haardt and Maraschi (1991) successfully reproduced the three components of X-ray spectra with a two-phase AD model where an important fraction of the gravitational power is dissipated via buoyancy and reconnection of magnetic fields in a hot corona surrounding the disk and the main cooling mechanism of the hot layer is comptonization of soft photons, thermally produced in the underlying cold phase.

2.3.4 Broad line region

This is the region responsible for the most characteristic feature of AGNs, the broad emission lines (BEL), that have been observed since the early discovery of that class of object (Seyfert, 1943). The Doppler width is in the range $\sim$ 1000 to 25000 km s^{-1} with a high density gas ($n_e > 10^9$ cm^{-3}). Since the BLR cannot be resolved, several indirect techniques have been used to find out the size of this region and the conclusion is that the size of this region in IR is in the scale of light days to months (Beckmann and Shrader, 2012).

Observations show a high variability from this region and photoionization is clearly the source of the observed lines, corresponding to permitted and semi-permitted transitions. Initial studies of reverberation mapping of multiple lines showed that high-ionization lines were originating from smaller radii than the low ionization-lines (Gaskell and Sparke, 1986) and later studies have confirmed the radial ionization stratification of the BLR. Several models have been proposed to explain the geometry and the characteristics of this unresolved region. Emmering et al. (1992) proposed that the BEL are formed by dense clouds in a molecular, hydromagnetic wind accelerated radiatively and centrifugally away from the AD.

One of the most popular models is the so-called LOC (acronym of "locally optimally emitting clouds") that was put forward by Baldwin et al. (1995). They modeled the photoionization for any line with different densities and distance from the continuum source to evaluate the maximum reprocessing efficiency, that mean local optimally emitting clouds. They showed that the sum of contributions from the different clouds produce a total spectrum similar to what is observed in AGN; the problem with this model is that the covering factor needs to be large (over 50%) to explain the line strengths. To solve this problem Gaskell et al. (2007) suggested the shielding model where clouds are concentrated in the equatorial plane, in contrast with the traditional model where clouds are distributed quasi-spherically. Most of the BLR clouds have a flattened distribution that extends out to the inner edge of the dusty torus; the inner clouds absorb much of the radiation before it can reach the outer clouds or the torus as it is shown in Fig. 2.7.

The actual picture is a set of dense clouds in the equatorial region between the accretion disk and the torus, or circumnuclear region (see subsection 2.3.5), at the dust sublimation radius. The lines are produced by photoionization of the reprocessed photons coming from the AD. The size of the BLR is of the order of a fraction of a parsec and it is still not possible to resolve it. In this thesis it is proposed to use reverberation in polarization (see chapter 6) to add constraints on this region as well as on other scattering regions of AGNs.

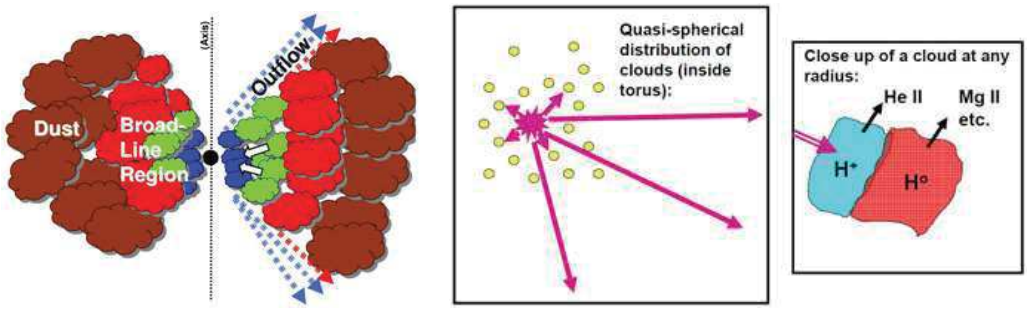

Figure 2.7: Scheme of the BLR structure. Left: A schematic view of the BLR embedded in the torus in the shielding model. Middle: Cartoon of a common traditional view of the BLR. Right: A schematic close up of an individual cloudlet (Gaskell, 2009).

2.3.5 Circumnuclear region (torus)

Historically known as torus or dusty torus, this region is filled with gas and dust, consequently responsible for the IR emission as is shown with the dashed pink line in Fig. 2.4. Circumnuclear region is a better denomination, because the geometry is uncertain. This region is located close to the equatorial plane, between the host galaxy and the BLR, and is perhaps an extension of the latter (see Fig. 2.5 and left scheme of Fig. 2.7). The origin of this region is not yet clear, it could be due to large scale winds of material from the host galaxy that is attracted by the SMBH, or it could be a wind of material expelled by the accretion disk, or both. The composition of the dust is also unknown, but it is probably made of silicates and carbon, and in order to allow for molecules to survive, it should stand at radii larger than the sublimation radius. The presence of this dense dust is responsible for the obscuration of broad lines in type-2 AGNs. Different dust components have been proposed, see subsection 3.2.2.

Several models have been developed to explain observations; most of them assume a toroidal structure surrounding the accretion disk. The initial models considered a uniform distribution of dust, later a clumpy dust distribution (Stalevski et al., 2012) was proposed as well as a mix of both (Siebenmorgen et al., 2015). But the geometry, composition and origin of the circumnuclear region have not yet been proven.

For a long time, due to its small size, the inner part of the dusty torus remained unresolved by telescopes and the only way to understand this region was by modeling to try to explain the large scale observations. At the present time, thanks to interferometry, it is possible to resolve this region in the nearest AGNs, but models and indirect techniques are still very helpful to understand them. The first model was proposed by Pier and Krolik (1992) and consists of a 2D simulation of an annular ring with uniform density. This model, however, does not agree with observation

in the IR and a smooth dust distribution cannot survive in the innermost part of an AGN.

The clumpy distribution of the dust turned out to be in better agreement with observations, including the X-ray variability. The usual parameters are: inner radius, often the sublimation radius, the outer radius, the half opening angle, the covering factor that depends on the number of clouds, and the optical depth of the clouds. In this thesis, this region was modeled using two different geometries (see chapter 5 for details).

2.3.6 Narrow line region

In contrast with the BLR that is located close to the center, the narrow line region is relatively far away from the SMBH and is one of the components of the AGN that has been resolved, showing dimensions in the range of parsecs to kilo-parsecs (Fischer et al., 2013) in the polar region of AGNs (see Fig. 2.5). The characteristic Doppler width is between 300 and 1000 kms^{-1} with low density gas ($n_e \approx 10^3 - 10^6 \mathrm{cm}^{-3}$). This region forms in general a bi-conical structure (Pogge, 1988); Pogge reported that with a simple ionization map obtained with the emission lines of Hα, [NII] and [OIII] a cone-shaped region revealed high-ionization gas emanating from the nucleus of the Seyfert-2 NGC 1068.

The NIR, optical and UV spectra allow us to observe more than one hundred lines from the NLR of nearby AGNs. These are low-ionization lines as NeII that should be emitted by HII regions, or NeIII whose origin should be HII regions or the NLR. There are also high-ionization lines, as NeV that can only be exited by the continuum (Netzer, 2013). The strongest narrow lines in Seyfert spectra are: $Ly\alpha$(λ1216), CIV(λ1549), CIII](λ1909), MgII (λ2798), [NeV](λ3426), [OII](λ3726), [NeIII](λ3869), HeII(λ4686), Hβ(λ4861), [OIII](λ4363, λ4959, λ5007), [NI](λ5199), HeI(λ5876), [FeVII](λ6087), [OI](λ6300), [FeX](λ6375), [NII](λ6548), Hα(λ6563), [NII](λ6583), [SII](λ6716 , λ6731) and [ArIII](λ7136) (Peterson, 1997).

The analysis of different lines allows us to determine the physical properties of the NLR, such as temperature or electron density. It is also possible to estimate the mass of this region. The typical temperature of the NLR is in the range of 12.000 - 25.000 K, as was obtained by Koski (1978) from the spectral analysis of 20 Seyfert-2 galaxies. For the same sample, he found that the average density in the line-emitting gas is about 2000 cm^{-3}. Most AGNs present a blue-shift asymmetry in the NL profile, with more flux on the short wavelength side of the line, relative to the peak. For example, Vaona et al. (2012) found asymmetries on the blue wing of the [OIII](λ5007) in 75% of a sample of 2153 Seyfert-2 and 521 intermediate-type Seyfert. The electron density and ionization decrease with radius (Bennert et al., 2006) and using the [OIII] line which is attributed to extended narrow line region (ENLR) or HII regions, they determined the radius of NLR in two Seyfert-2 to be

700 - 1500 pc while for three other objects the size determined by them is 700 - 3300 pc.

In the polar region of AGNs the NLR extends to the region where it becomes mixed with the host galaxy gas.

2.3.7 Polar winds

Between the NLR and the central BH there are three zones that should be distinguished: the warm absorber (WA), the non ultrafast outflows and the Ultra Fast Outflow (UFOs); the classification between the latter two depending on their speed, whether it is lower or higher than 10,000 km s^{-1}.

A high ionization wind cone was inferred from blue-shifted K-shell resonance absorption lines from FeXXV and FeXXVI (Tombesi et al., 2010b,a) who gave the name of Ultra Fast Outflows (UFOs). In average, UFOs are located at 0.0003 - 0.03 pc from the central BH, with a mass outflows rate between 0.01 and 1 $M_{\odot}$ yr^{-1} and blue shifted velocity $\geq$ 10,000 kms^{-1} (Tombesi et al., 2012). The characteristic column density for UFOs are between $N_H \sim 10^{22}$ and 10^{24} cm^{-2} (Tombesi et al., 2013).

On the other hand, non-UFOs are less ionized with rates of blue shifts less than 10,000 kms^{-1}. Velocities are in the range 0.04 - 0.15 c, with a mass outflows rate between 0.1 and 0.5 $M_{\odot}$ yr^{-1} and $N_H \sim 10^{22}$ - 10^{24} cm^{-2}. Their distance to the BH is between 0.03 and 0.3 pc (Tombesi et al., 2012).

The short distance of UFOs and non-UFOS to the center engine may indicate an origin in AD winds or AD outflows. Kraemer et al. (2018) defined the UFOs as massive, highly ionized, modestly relativistic outflows, that moderate the BH growth by a large quantity of mass and energy outflow, and they suggest that they should be part of a magneto-hydrodynamic (MHD) wind. They also argue that the electron temperature T_e ($< 10^9$ K) is produced by the equilibrium between heating by Compton scattering and cooling by inverse Compton scattering.

The material observed in absorption in soft X-rays is called warm absorber, it is responsible for several absorption lines that are systematically blue-shifted, showing outflows velocities in the range $\sim$100 - 1000 km s^{-1} and they are located at approximately 1 pc from the BH, with column density between $N_H \sim 10^{20}$ and 10^{22} cm^{-2} (Ramírez and Tombesi, 2012). This region is also included in the models presented here (see chapter 5).

2.3.8 Jets

Jets have been observed in only about 10% of AGNs. These are fast and very collimated outflows that emerge near the center of the AGNs and extend up to millions of parsecs on both sides of the symmetry axis. Their origin is still unclear. Observation shows that jets are accelerated at sub-parsec scale, the most likely mechanism being magnetic driven scenarios (Vlahakis and Königl, 2004). Superluminal motion are observed that can reach 40 c, and the polarimetry variability locate the relativistic components at distances less than 1 pc and can get as far as kpc or Mpc distances (Königl, 2006). The apparent speed greater than c is an optical effect produced by jets traveling at speeds close to the speed of light and whose direction is at a very small angle with respect to the observer. In radio it is also possible to observe lobes at the end of the jet. The jets emit at all wavelengths from radio to γ-ray.

There are several models that try to explain the origin and dynamics of jets. Shibata and Uchida (1985) proposed the magneto dynamical mechanism for jets formation, where the accretion disk twist the magnetic field lines of the intergalactic media (Uchida and Shibata, 1985). Another model that also proposes the origin of the jets in the accretion disk is magneto-centrifugal acceleration from the disk, which is known as Blandford-Payne (BP) (Blandford and Payne, 1982). There are other theories that locate the origin of jets at the black hole horizon, such as magneto-centrifugal acceleration from the BH. In this case the wind that forms the jets is taken out of the black hole magnetosphere by the mechanism known as Blandford & Znajek (Blandford and Znajek, 1977).

Figure (2.8) shows a scheme of quasars that includes the AD, the disk corona, the BLR, the NLR and the jets in contrast with same scheme with emission region. This picture is taken from Marscher (2005).

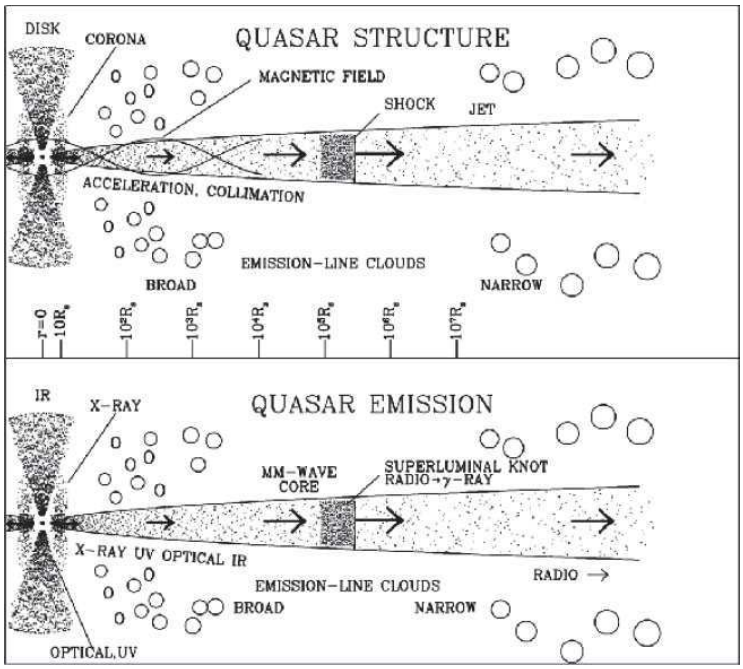

Figure 2.8: Scheme of the structure and emission regions of a radio-loud AGN, including jets (Marscher, 2005).

Chapter 3

Polarization and Polarimetry

Polarization is a fundamental characteristic of light. We can classify polarization as linear, circular and elliptical and there are different sources of polarization (Fig.3.1). We focus here just on linear polarization produced by electron and/or dust scattering. There are many possible mechanisms to polarize the incident light, including Thomson scattering when radiation interacts with an electron. When photon energy is larger than electron rest energy, we refer to Compton scattering; when the electron is relativistic we are in the presence of inverse Compton scattering. Radiation scattering by atoms or molecules is called Rayleigh and/or Mie scattering.

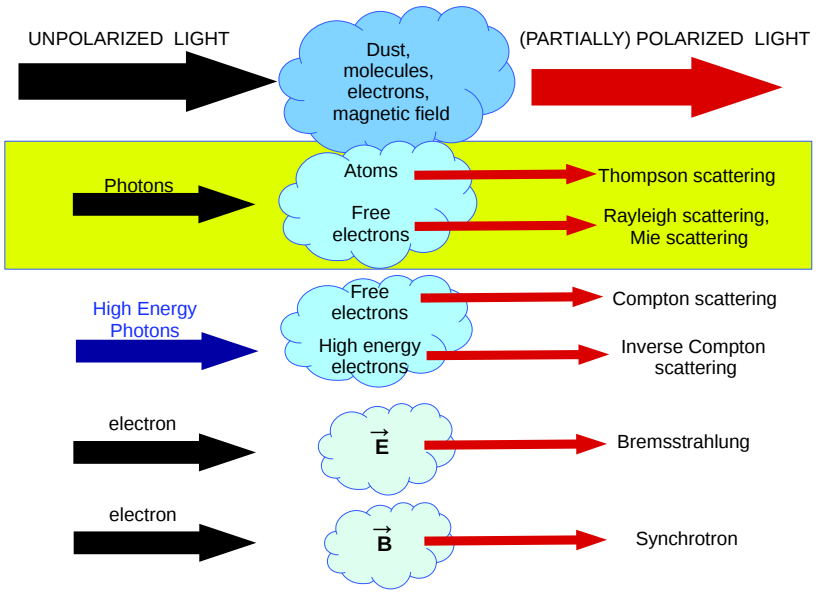

Figure 3.1: Scheme of the source of polarization.

This chapter intends to give a global vision of polarization and of its impact on the development of astrophysics, especially in the AGN context.

3.1 Mathematical representation of polarization

Light is an electromagnetic wave where an electric field $\vec{E}$ propagates together with a magnetic field $\vec{B}$ perpendicular to it, $\vec{E}$ and $\vec{B}$ being both perpendicular to the

propagation direction, in phase and whose planes of displacement are perpendicular to each other. The light is unpolarized when the electric (or magnetic) field orientation is random and is polarized when the opposite situation takes place. For perfectly coherent light the following characteristic polarization states can be distinguished; if the electric field orientation is constant, polarization is linear, if the angle varies in time and describes circles, polarization is circular. If the electric field varies systematically describing an ellipse, the polarization is elliptical. Further details can be found in Rybicki and Lightman (1985).

3.1.1 Stokes Parameters

Electromagnetic radiation is described as a wave traveling in space and its electric vector can be described by $\vec{E} = \vec{E}_0 e^{i(\vec{k}\cdot\vec{x}-\omega t)}$, where $\vec{E_0}$ is the amplitude and $\phi{=}\vec{k}\cdot\vec{x}{-}\omega$t is the phase. It can be decomposed in Cartesian coordinates assuming that the 2 components are in the direction of propagation and:

$$E_x = E_{x0} e^{i\phi} \tag{3.1}$$

$$E_y = E_{y0} e^{i\phi} \tag{3.2}$$

In 1852 Sir George Gabriel Stokes developed a mathematical method to describe the state of polarization using observable polarized fluxes at different polarization position angles. Using the appropriate representation of the Cartesian coordinates in spherical coordinates, he computed four parameters, today known as the "Stokes parameters", to describe polarization: I, Q, U and V.

$$I = \langle E_x \rangle^2 + \langle E_y \rangle^2 \tag{3.3}$$

$$Q = \langle E_x \rangle^2 - \langle E_y \rangle^2 \tag{3.4}$$

$$U = 2E_x E_y \cos(\delta x - \delta y) \tag{3.5}$$

$$V = 2E_x Ey \sin(\delta x - \delta y) \tag{3.6}$$

Where "$\langle\ \rangle$" denotes the time average.

I is the total intensity, Q shows the linear polarization projected on the vertical and horizontal axes of the polarization ellipse (Fig. 3.2-right side), while U is the projected linear polarization at 45 degrees of the vertical and horizontal axis. V is the representation of circular polarization; when V is negative the rotation is in the counterclockwise direction (see Fig. 3.2-left hand side).

A very useful way to use the Stokes parameters is the matricial representation shown in equation 3.7. We see, on the left side, the Stokes vector in terms of the polarization ellipse parameters:

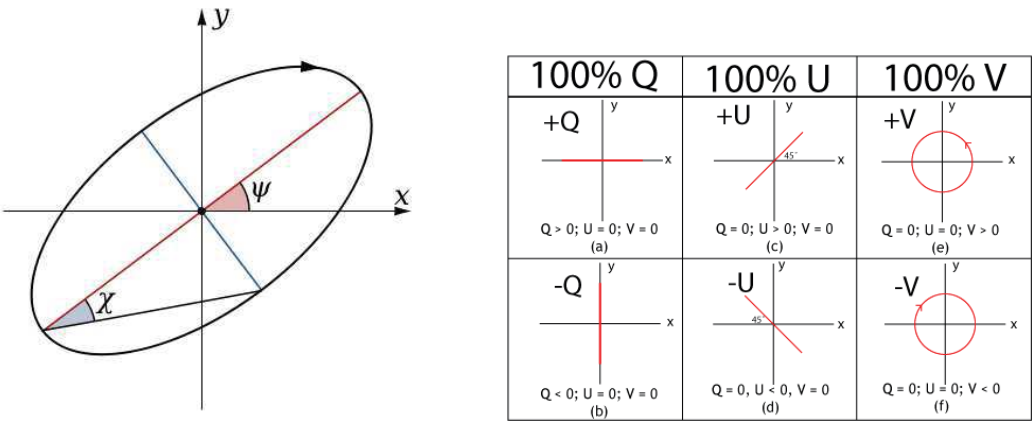

Figure 3.2: *Left:* Polarization ellipse (by https://commons.wikimedia.org) *Right:* representation of the Stokes Parameters (by Dan Moulton).

$$[S] = \begin{bmatrix} I \\ Q \\ U \\ V \end{bmatrix} = \begin{bmatrix} I \\ IPcos(2\psi)cos(2\chi) \\ IPsin(2\psi)cos(2\chi) \\ IPsin(2\chi) \end{bmatrix} \tag{3.7}$$

where P is the polarization fraction (Eq. 3.12), with values between 0 and 1.

The unitary vector shows the state of polarization, such as:

$$\begin{bmatrix} Unpolarized \\ beam \end{bmatrix} = \begin{bmatrix} 1 \\ 0 \\ 0 \\ 0 \end{bmatrix} \tag{3.8}$$

$$\begin{bmatrix} Linear \\ Polarization \\ (horizontal) \end{bmatrix} = \begin{bmatrix} 1 \\ 1 \\ 0 \\ 0 \end{bmatrix} \tag{3.9}$$

$$\begin{bmatrix} Linear \\ Polarization \\ (vertical) \end{bmatrix} = \begin{bmatrix} 1 \\ 0 \\ 1 \\ 0 \end{bmatrix} \tag{3.10}$$

$$\begin{bmatrix} Circular \\ Polarization \end{bmatrix} = \begin{bmatrix} 1 \\ 0 \\ 0 \\ 1 \end{bmatrix} \tag{3.11}$$

The degree of polarization P is defined as the ratio between the intensity of the polarized light and the total intensity (Eq. 3.12).

$$P = \frac{I_{pol}}{I} = \frac{\sqrt{Q^2 + U^2 + V^2}}{I} \tag{3.12}$$

3.1.2 Mueller Matrix

The Stokes parameters represent the polarization state of a beam; the 4x4 Mueller matrix describes the interaction of this beam with matter whose parameters represent its optical characteristics. So computing both Stokes parameters and the Mueller matrix gives us an equation that describes the relation between the incident and the transmitted light beams (Eq. 3.13).

$$\begin{bmatrix} I' \\ Q' \\ U' \\ V' \end{bmatrix} = \begin{bmatrix} M \end{bmatrix} \begin{bmatrix} I \\ Q \\ U \\ V \end{bmatrix} \tag{3.13}$$

The Mueller matrix has different parameters depending on the optical characteristics of the media. Equations (3.14), (3.15) and (3.16) give several examples for a linear horizontal polarizer and a circular polarizer .

$$\begin{bmatrix} Linear \\ Polarizer \\ (horizontal) \end{bmatrix} = 1/2 \begin{bmatrix} 1 & 1 & 0 & 0 \\ 1 & 1 & 0 & 0 \\ 0 & 0 & 0 & 0 \\ 0 & 0 & 0 & 0 \end{bmatrix} \tag{3.14}$$

$$\begin{bmatrix} Circular \\ Polarizer(+) \end{bmatrix} = 1/2 \begin{bmatrix} 1 & 0 & 0 & -1 \\ 0 & 0 & 0 & 0 \\ 0 & 0 & 0 & 0 \\ -1 & 0 & 0 & 1 \end{bmatrix} \tag{3.15}$$

$$\begin{bmatrix} Circular \\ Polarizer(-) \end{bmatrix} = 1/2 \begin{bmatrix} 1 & 0 & 0 & 1 \\ 0 & 0 & 0 & 0 \\ 0 & 0 & 0 & 0 \\ 1 & 0 & 0 & 1 \end{bmatrix} \tag{3.16}$$

Other matrices describe the interaction between light and matter, such as Mie scattering (see 3.37). All different processes responsible for polarization in AGNs are further discussed in this chapter.

3.2 Polarization mechanisms

As mentioned at the beginning of this chapter, there are different mechanisms that can produce polarization. I will present the most important ones for astrophysical purposes that cause linear polarization, as shown in Fig. 3.1, and in particular those present in the innermost region of AGNs and that cover the optical and UV bands studied in this thesis.

3.2.1 Thomson scattering

Thomson scattering occurs in AGNs when a photon emitted by the accretion disk encounters an electron in the polar winds or in the BLR (see subsection 2.3.4). In the *STOKES* code, Thomson scattering is used to calculate the polarization emerging from ionized regions.

Thomson scattering is produced when a low energy photon interacts with a free electron ($E = h\nu << mc^2$). As a result of the interaction, the electron redirects the photon with the same energy in a different direction at an angle Θ with respect to the incident photon as shown in Fig. (3.3). The scattering cross section is independent of the polarization state of the beam, and the differential cross section can be written as:

$$\frac{d\sigma}{d\Omega} = \frac{1}{2}(1 + cos^2\Theta)r_0^2 \tag{3.17}$$

where r_0 is the classical electron radius. The total cross section is then:

$$\sigma_T = 2\pi \int_0^\pi \frac{d\sigma}{d\Omega} sin(\Theta) d\Theta = \frac{8\pi}{3} r_0^2 = \frac{8\pi}{3} \frac{e_0^4}{m^2 c^4} \tag{3.18}$$

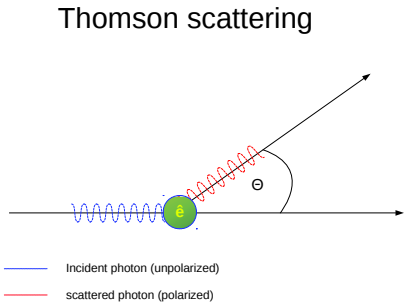

Figure 3.3: Scheme of Thomson scattering. Directions of the photon before (blue) and after (red) scattering by the electron are shown.

As the energy of the incident photon is the same as the polarized photon, but with a different orientation, the degree of polarization is:

$$P = \frac{I_{pol}}{I} = \frac{(1 - cos^2\Theta)}{(1 + cos^2\Theta)} \tag{3.19}$$

The scattering phase function $P(\Theta, \phi)/4\pi$ describes the angular distribution of scattered radiation and is defined as:

$$\int_0^{4\pi} P(\Theta, \phi) d\omega = \int_0^{2\pi} d\phi \int_0^{\pi} d\Theta sin(\Theta, \phi) = 4\pi \tag{3.20}$$

where ϕ is the azimuthal angle.

For details of Thomson scattering see section 3.4 of Rybicki and Lightman (1985).

3.2.2 Dust scattering

An important source of polarization in many of astrophysical environments is dust scattering. Dust and gas are present in the interstellar medium (ISM). Even if it represents only 10% of the total ISM mass, it has a big impact on observations because it is efficient in scattering, absorbing and re-emitting the incident light.

The main impact of dust is its obscuration of cosmic sources. A good example is the effect of the circumnuclear medium in AGNs (see chapter 2) in which dust hides the broad lines for type-2 viewing angles. Dust is responsible for most of the extinction, polarization and IR emission of AGNs.

Conventional models assume light scatters on dust particles shaped as spheres and composed of graphite and silicates. There are however other models like T-Matrix and Discrete Dipole Approximation (DDA) (Purcell and Pennypacker, 1973; Draine, 1988) which add more complexity to the shape of dust particle because they are no longer spherical but elongated.

When an electromagnetic wave interacts with dust, its interaction is at the end with charges, since matter is composed by electrons and protons. When dust is irradiated, the electromagnetic wave generates vibrational movement in the charges, which generates a secondary wave: the scattered electromagnetic wave. However, the vibrating charge can transform all or part of the incident energy in other forms such as thermal energy, resulting in absorption. The parameters involved are the

energy of the incident wave and the characteristic of the dust, as well as its homogeneity and the cross section of particles. The study of dust can be reduced to the calculation of a large number of dipoles interacting with electromagnetic waves. The matter, in this case dust, is characterized by its refraction index. This index can be measured in a laboratory, and there are tables providing this information. The dielectric indices for silicates and graphites, the component of the dust we used in this thesis, are taken from Draine and Lee (1984), and have been used to compute the effect of dust in the *STOKES* code (Chapter 4).

The challenge is to calculate the scattering and absorption cross section at different wavelengths. When the size of a particle of dust is small as compared to the wavelength, it is computed using the Rayleigh theory, which is relatively simple. When the grain size is larger, the interaction with radiation becomes more complex and it is necessary to apply Mie theory. What follows is based on Bohren and Huffman (1983).

3.2.3 Mie scattering

Mie theory is a way to solve the Maxwell equation for the incident light with particle modeled by spheres, using coefficients of the expansion series of the wave function. If we take an electromagnetic wave with a wavelength λ in interaction with a particle only consisting of a sphere with a radius a and a refraction index n, a secondary scattered and polarized electromagnetic wave will be emitted.

The wave function Ψ of the electromagnetic field $(\vec{E}, \vec{B})$ in homogeneous medium must obey the Maxwell equations:

$$\nabla \cdot \vec{E} = 0 \quad \nabla \cdot \vec{B} = 0 \quad \nabla \times \vec{E} = i\omega\mu\vec{B} \quad \nabla \times \vec{B} = -i\omega\varepsilon\vec{E} \tag{3.21}$$

where μ is the magnetic permeability and ε is the dielectric constant. Combining time-dependent Maxwell equations, wave equations for $\vec{E}$ and $\vec{B}$ are obtained, and:

$$\nabla^2\vec{E} + k^2\vec{E} = 0 \tag{3.22}$$

$$\nabla^2\vec{B} + k^2\vec{B} = 0 \tag{3.23}$$

In the following, we do not distinguish between $\vec{E}$ and $\vec{B}$ and we use the general form of:

$$\nabla^2\Psi + k^2\Psi = 0 \tag{3.24}$$

Using transformation of coordinates as shown in Fig. (3.4) the expression of 3.24 in spherical coordinate is:

$$\frac{1}{r^2}\frac{\delta}{\delta r}(r^2\frac{\delta\psi}{\delta r}) + \frac{1}{r^2 sin(\theta)}\frac{\delta}{\delta\theta}(sin(\theta)\frac{\delta\psi}{\delta\theta}) + \frac{1}{r^2 sin(\theta)}\frac{\delta^2\psi}{\delta\phi^2} + k^2\psi = 0 \tag{3.25}$$

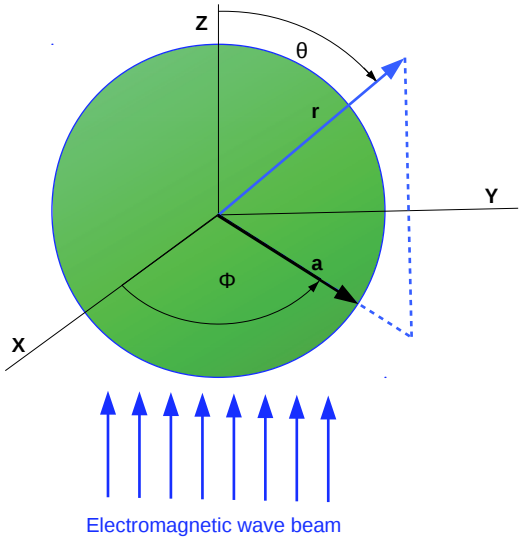

Figure 3.4: Scheme of a polar coordinate system centered on a spherical particle of radius a which is irradiated by a beam of light.

One solution to the wave equation is found by separating it in three functions (Eq. 3.26 and Eq. 3.27).

$$\psi = f(R\Theta\phi)e^{-iwt} \tag{3.26}$$

$$f(R\Theta\phi) = R(r)\Theta(\theta)\Phi(\phi) \tag{3.27}$$

Eq. 3.25, then, gives three different equations (Eq. 3.28, Eq. 3.29 and Eq. 3.30) for R, Θ and Φ. The details can be found in Bohren and Huffman (1983):

$$\frac{d}{dr}(r^2\frac{dR}{dr}) + [k^2r^2 - n(n+1)]R = 0 \tag{3.28}$$

$$\frac{1}{sin\theta}\frac{d}{d}(sin(\theta)\frac{d\Theta}{d\theta}) + [n(n+1) - \frac{m^2}{sin^2\theta}]\Theta = 0 \tag{3.29}$$

$$\frac{d^2\Phi}{d\phi^2} + m^2\Phi = 0 \tag{3.30}$$

The solution for Eq. 3.30 is either a cosine or sin of $(l\phi)$, while the solutions for Eq. 3.29 are the Legendre functions, $P_n^m(cos(\theta))$ of degree n and order m. The solution for Eq. 3.28 are the spherical Bessel functions, J_ν. So, the solution of the wave function is:

$$\psi = sin(l\phi)P_n^m cos(\theta)J_\nu(kr) \quad or \quad \psi = cos(l\phi)P_n^m cos(\theta)J_\nu(kr) \tag{3.31}$$

where k and l are constants.

The coefficient of the expansion in spherical harmonics of the vector field are represented by a_n (3.32) and b_n (3.33) for the scattering wave.

$$a_n = \frac{m\psi_n(m\beta)\psi_n^{'}(\beta) - \psi_n(\beta)\psi_n^{'}(m\beta)}{m\psi_n(m\beta)\xi n^{'}(x) - \xi n(\beta)\psi_n^{'}(m\beta)} \tag{3.32}$$

$$b_n = \frac{\psi_n(mx)\psi_n^{'}(\beta) - m\psi_n(\beta)\psi_n^{'}(m\beta)}{\psi_n(m\beta)\xi_n^{'}(x) - m\xi_n(x)\psi_n^{'}(m\beta)} \tag{3.33}$$

with $\beta = 2\pi a/\lambda$ while ψ_n and ξ_n are the Riccati-Bessel functions.

The total scattering cross section σ_{sca} is given by integration over all solid angles of the fraction between the energy scattered per unit of time and per unit solid angle, and the total incident energy flux per unit time and per unit area. The scattering cross section σ_{sca} in terms of the coefficients of expansion a_n and b_n is:

$$\sigma_{sca} = \frac{2\Pi}{k^2}\sum_{n=1}^{\infty}(2n+1)(|a_n|^2 + |b_n|^2) \tag{3.34}$$

and the extinction cross section σ_{ext}, represents the total losses of energy from the incident beam. Written in terms of the coefficients of expansion a_n and b_n, it is:

$$\sigma_{ext} = \frac{2\Pi}{k^2}\sum_{n=1}^{\infty}(2n+1)R_e\{a_n + b_n\} \tag{3.35}$$

The absorption cross section σ_{abs} is simply:

$$\sigma_{abs} = \sigma_{ext} - \sigma_{sca} \tag{3.36}$$

The matrix that relates the incident and scattered Stokes parameters is shown in 3.37

$$\begin{bmatrix} I^{'} \\ Q^{'} \\ U^{'} \\ V^{'} \end{bmatrix} = \frac{1}{k^2r^2}\begin{bmatrix} S_{11} & S_{12} & 0 & 0 \\ S_{12} & S_{11} & 0 & 0 \\ 0 & 0 & S_{33} & S_{34} \\ 0 & 0 & -S_{34} & S_{33} \end{bmatrix}\begin{bmatrix} I \\ Q \\ U \\ V \end{bmatrix} \tag{3.37}$$

where:

$$S_{11} = \frac{1}{2}(|S_1|^2 + |S_2|^2) \tag{3.38}$$

$$S_{12} = \frac{1}{2}(|S_2|^2 - |S_1|^2) \tag{3.39}$$

$$S_{33} = \frac{1}{2}(S_1S_2^* + S_2S_1^*) \tag{3.40}$$

$$S_{34} = \frac{1}{2}(S_1S_2^* - S_2S_1^*) \tag{3.41}$$

$$S_1 = \sum_n \frac{2n+1}{n(n+1)}(a_n\pi_n + b_n\tau_n) \tag{3.42}$$

$$S_2 = \sum_n \frac{2n+1}{n(n+1)}(a_n\tau_n + b_n\pi_n) \tag{3.43}$$

The terms π_n and τ_n are angle-dependent functions and are related to the incident and scattering angle θ as shown in (3.44):

$$\pi_n = \frac{P_n^1}{sin(\theta)}, \quad \tau_n = \frac{dP_n^1}{d\theta} \tag{3.44}$$

The *STOKES* code computes the scattering induced polarization of light propagating in a region full of dust, like in the circumnuclear region in AGNs, using the Mie scattering algorithm.

3.2.4 Rayleigh scattering

The Rayleigh regime applies when the size of the particle is smaller than the wavelength, i.e. $2\pi a << \lambda$, where a is the radius of the particle. Rayleigh scattering is present in the circumnuclear region (see subsection 2.3.5), or in the BLR (see subsection 2.3.4) (Gaskell and Goosmann, 2013; Korista and Ferland, 1998), where the grains become smaller. In the *STOKES* code, Rayleigh's scattering is used to calculate the polarization arising from regions filled with small particles.

Rayleigh scattering is similar to Thomson scattering; however, in this case the electrons are not free but bound to atoms or molecules, and should be treated as in Mie scattering with the advantage that Rayleigh scattering allows us to simplify by using the small particle approximation. The Rayleigh approximation consists of the elastic dispersion of low energy photons. The electrons oscillate at the same frequency as the incident wave and produce a radiation at the same frequency, as in Thomson scattering. The cross section is the atomic cross section but with the addition of the bound energy of the electron to compute the energy and the momentum of the system.

We can reduce the problem to an electromagnetic wave characterized by its electromagnetic field $\vec{E}$ and frequency ω that interacts with an oscillating bound electron at frequency ω_0 and charge e_0. The equation of motion for a bound electron is given by:

$$\vec{a} = \frac{d^2\vec{x}}{dt^2} = -\omega_0^2\vec{x} - \frac{e_0}{m_e}\vec{E} \tag{3.45}$$

$\vec{a}$ being the electron acceleration and $\vec{x}$ is the electron position.

The total energy, per unit area per second, radiated by an accelerating charge is given by the square of the electric field (generated by the accelerated charge), like

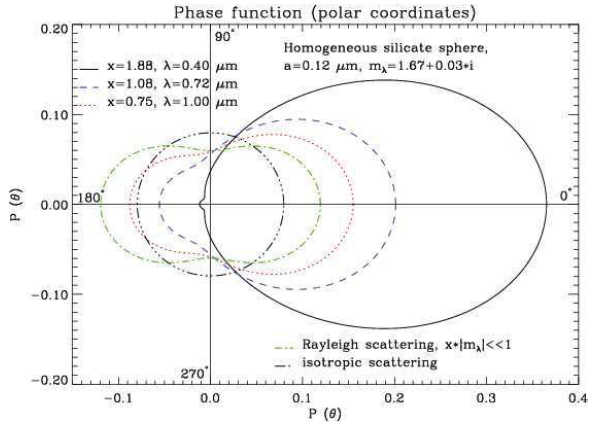

Figure 3.5: Scattering phase function in polar coordinates for homogeneous spherical silicate particle of size $a = 0.2$ μm, where m_λ is the refractive index and $x = 2\pi a/\lambda$, from Steinacker et al. (2003).

the area is a fraction of an sphere. Integrating over the complete solid angle we obtain the radiated power P:

$$P = \frac{2}{3}\frac{e_0^2}{c^3}|a|^2 = \frac{1}{3}\left(\frac{e_0^2}{m_e c^2}\right)^2 \left(\frac{\omega^4}{\omega_0^2 - \omega^2}\right)^2 cE^2 \tag{3.46}$$

The cross section is $\sigma = P/I$ with $I = cE_0^2/8\pi$; resulting in the Rayleigh scattering cross section:

$$\sigma_R = \frac{8\pi}{3}(\frac{e_0^2}{m_e c^2})^2(\frac{\omega^2}{\omega_0^2 - \omega^2})^2 \tag{3.47}$$

Note that for free electrons $\omega_0 = 0$ and σ_R takes the form of the Thomson cross section (Eq. 3.18). The scattering phase function in polar coordinates is shown in Fig. 3.5, the plot is the findings of Steinacker et al. (2003) for spherical silicates particle of size $a = 0.12$ μm and diffraction index m_λ for $\lambda = 0.40, 0.72$ and 1.00 μm.

Chapter 4

STOKES

This chapter introduces *STOKES*, a Monte Carlo radiative transfer code used to model multi-wavelength polarization. The first sections present a review of the radiative transfer and the Monte-Carlo method as a way of solving the radiative transfer problem. Then we focus on *STOKES*, and how to use it with a focus on the parts of the algorithm used in this thesis.

4.1 Radiative transfer

The radiative transfer theory is a mathematical tool that describes the interaction between radiation and matter. Radiation is described by four observables: energy flux, direction, frequency and polarization. The energy flux, F, defined as the quantity of energy per unit time and unit area is:

$$F = \frac{dE}{dtdA} \tag{4.1}$$

The specific intensity I_ν, is the quantity of energy per unit time, per area, per solid angle and frequency:

$$I_\nu = \frac{dE}{dtdAd\Omega d\nu} \tag{4.2}$$

Radiative transfer describes the changes in a specific intensity of the radiation when it propagates. When radiation travels through vacuum, the change in I_ν is null, but when radiation interacts with matter, I_ν changes because of absorption, emission and scattering.

The differential of the radiative flux in a specific direction crossing the effective area $\cos(\theta)dA$ is:

$$dF_\nu = I_\nu \cos(\theta) d\Omega \tag{4.3}$$

We can see that the radiative flux obtained by integrating over all solid angles is a moment of I_ν:

$$F_\nu = \int I_\nu \cos(\theta) d\Omega \tag{4.4}$$

The emission can be spontaneous or stimulated by radiation. The spontaneous emission coefficient, j_ν, is defined as the energy emitted per unit time per unit solid angle and per unit volume

$$j_\nu = \frac{dE}{dtdVd\Omega} \tag{4.5}$$

For an isotropic emitter, it would take the form:

$$j_\nu = \frac{1}{4\pi} P_\nu \tag{4.6}$$

where P_ν is the radiated power per unit volume per unit frequency.

The absorption coefficient α_ν is defined as the loss of energy of radiation when it travels a distance dl; relation (4.7) shows the intensity for a radiation which goes through matter. By convention α_ν is positive for the energy taken out of radiation:

$$dI_\nu = -\alpha_\nu I_\nu dl \tag{4.7}$$

The radiative transfer equation is the combination of emission and absorption and it is as follows:

$$\frac{dI_\nu}{dl} = -\alpha_\nu I_\nu + j_\nu \tag{4.8}$$

It is usually written as:

$$\frac{dI_\nu}{d\tau_\nu} = -I_\nu + S_\nu \tag{4.9}$$

where $S_\nu = j_\nu/\alpha_\nu$ is the source function.

The optical depth τ_ν is the measure of the absorption along the path of a ray:

$$\tau_\nu = \int \alpha_\nu dl \tag{4.10}$$

Any matter is considered to be optically thick or opaque when the typical path integrated through the entire length satisfies $\tau_\nu > 1$, and it is optically thin or transparent when $\tau_\nu < 1$.

If the source function $S(l) = S(\tau)$ is constant, the radiative transfer equation is relatively simple to solve:

$$I = I(0)e^{-\tau} + S(1 - e^{-\tau}) \tag{4.11}$$

However, when scattering is present, the solution becomes much more difficult because the source function is no longer constant, depends on the intensity and one must consider absorption and re-emission. For example, the transfer equation for thermal radiation in thermodynamic equilibrium and in the absence of scattering is:

$$\frac{dI_\nu}{d\tau_\nu} = -I_\nu + B_\nu(T) \tag{4.12}$$

where $B_\nu(T)$ is the Planck function.

Furthermore, for more complex geometries where scattering and absorption are present, solving the classical radiative transfer equation becomes extremely difficult. In this case the Monte-Carlo method is a good approximation, using iterations approach featuring single photons to solve it. The scattering process should be described as an absorption plus an emission.

4.2 Monte-Carlo method

As we have seen it is not trivial to solve radiative transfer equations. With computers it is possible to overcome this and acquire fast and reliable results. One efficient and well-known technique is the Monte-Carlo method, an algorithm based on statistics to solve mathematical problems, using the abilities of a processor to retrieve solutions using random sampling.

Examples of the Monte-Carlo method are widely used in *STOKES*. Some of them are: generating and defining the source photons, computing the probability of interaction (scattering or absorption) of the photons with electrons and/or dust grains. It is also used to sample the path length between the scattering region.

4.2.1 Monte-Carlo method and the radiative transfer problem

Instead of attempting to solve the equation of radiative transfer, the problem can be approached by considering the radiative transfer of individual photon packets in their interaction with matter. The role of the Monte-Carlo method is to provide the solution, using iterative methods, of the probability of a packet of photons being absorbed or scattered when they interact with matter. Each packet of photons has a specific direction of travel and specific energy related with the specific intensity I_ν. The interaction of the packet of photons with matter obey probabilistic laws depending of the absorption and scattering cross sections of the particles in the medium.

If we have a number n of scattered or absorbed photons in a medium, with a cross section σ, the number of photons scattered/absorbed per area per second is $I_\nu n\sigma dl$ and (4.7) should be written as:

$$dI_\nu = -I_\nu n\sigma dl \tag{4.13}$$

The term nσ is called the volume absorption coefficient and is related to the opacity κ by:

$$n\sigma = \rho\kappa \tag{4.14}$$

where ρ is the mass density.

The probability that a photon travels a length dl without interaction is $(1-n\sigma dl)$. Considering a length L divided in N segments, then this probability is:

$$P(L) = (1 - n\sigma dl)^N = e^{-n\sigma L} = e^{-\tau} \tag{4.15}$$

To find the probability of a packet of photons to be scattered or absorbed, it is useful to introduce the albedo A, such as:

$$A = \frac{n_s\sigma_s}{n_s\sigma_s + n_a\sigma_a} \tag{4.16}$$

where n_s and σ_s are the scattering number density and scattering cross section, while n_a and σ_a are the absorber number density and absorber cross section. Now it is possible to follow the trajectories of the photons through absorption and scattering.

4.3 *STOKES* Code

STOKES is a radiative transfer code based on the Monte-Carlo method that solves the radiative transfer problem for all four *Stokes* parameters. The versions used in this work focuses on scattering-induced polarization and includes dust and electron scattering.

The remaining task is to solve the trajectory of a photon, that is emitted from the source and to follow its path and its interactions with matter (dust or free electrons), independently if the photon is absorbed or re-emitted. The first task for *STOKES* is to generate photons with random directions. To then solve the radiative transfer problem, when the photon interacts with matter in the scattering regions. For instance, the path length between the dispersion regions is sampled using the Monte-Carlo method.

The user creates various emission and scattering regions inside the model space and the code then follows individual photons between these regions until they are absorbed or escape from the model region. Different geometries for the emitting and scattering structures are possible: toroidal, cylindrical, spherical or conical shapes.

In the context covered in this thesis the emission region should be a point-like or a disk-like source. The scattering regions are a torus, an extended flared disk, a double-cone and spheres. The emission and scattering geometries are described

by mathematical equations (of up to the fourth order) relative to a Cartesian coordinate system. Parameters to include in the definition of scattering media are the density, the group velocity, the number of viewing angles and the spectral resolution. The version used in this work also accounts for time resolution, and provides (time-dependent) spectra.

Several codes have been developed to solve the problem of radiative transfer in AGNs, using the Monte Carlo method and many of them include polarization (Wolf and Henning, 1999; Watanabe et al., 2003; Stalevski, 2012; Grosset et al., 2018). *STOKES* continues to improve and new tasks have been incorporated since its conception. It also has the advantage of addressing time-dependent polarization.

4.3.1 Overview

STOKES was developed by Goosmann and Gaskell (2007) with the aim to simulate the polarization in the central regions of AGN. Using Monte Carlo routines the code computes the trajectory of a photon generated by a central source (with unpolarized emission). On its way inside the model space the photon may be absorbed, scattered or it can escape. In the latter case it is registered by the virtual web of detectors located around the model. After the initial development of the code, several upgrades have been made (Marin et al., 2012, 2015; Marin, 2018). For example, significant improvements for computational speed and polarization imaging has been implemented, and the last upgrade was to include spectral energy distribution (SED) templates for a set of representative host galaxies.

The aim of the Monte-Carlo method is to sample the probability distribution function (PDF). From it, *STOKES* produces random numbers, r_i, defined in the interval 0 to 1, while $i = 0, 1, 2, ...$

To generate the initial photon model, its position, direction of travel and wavelength must be defined. The position is set as a random position considering constant density of the emission region. The travel direction is given by the angles θ and ϕ of the polar system, which sampling equations are:

$$\theta = \arccos(1 - 2r_1) \tag{4.17}$$

$$\phi = 2\pi r_2 \tag{4.18}$$

where r_1 and r_2 are two random numbers between 0 and 1.

The wavelength is calculated to be within the range $[\lambda_{min}, \lambda_{max}]$, as:

$$\lambda = \begin{cases} \left[\lambda^{\alpha_{min}} + r_3\left(\lambda^{\alpha}_{max} - \lambda^{\alpha}_{min}\right)\right]^{\frac{1}{\alpha}} & \text{for } \alpha \neq 1, \\ \lambda_{min}\left(\frac{\lambda_{max}}{\lambda_{min}}\right)^{r_3} & \text{for } \alpha = 1 \end{cases} \tag{4.19}$$

where r_3 is again a random number in the range [0,1].

To compute the interaction between the photons and the matter, after having generated a set of photons with random energy and initial trajectories, *STOKES* calculates the polarization features and their change during scattering events. The initial photon is unpolarized, and the polarization vector is the one described in the previous chapter (see Eq.3.8).

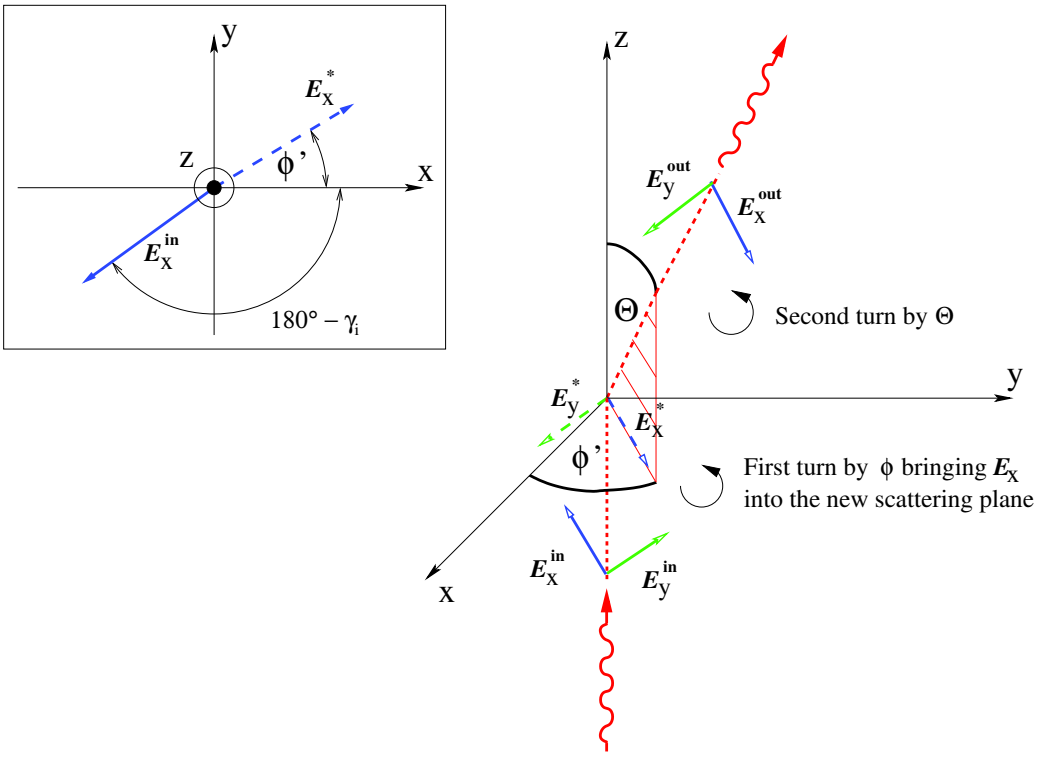

Figure 4.1: Schema of the electric field vector variation in a scattering event (Goosmann and Gaskell, 2007).

Each time the photon is affected by a scattering event, the resulting Stokes vector S' will be the result of the rotation on the azimuth axis ϕ, followed by a rotation on the scattering angle θ (Fig. 4.1), while the change determined by the scattering

region, as we saw in the previous chapter, is represented by the Mueller matrix [M]. In this way the Stokes parameters of the resulting photon will be:

$$\begin{bmatrix} I' \\ Q' \\ U' \\ V' \end{bmatrix} = [R(\phi)]\,[R(\theta)]\,[M] \begin{bmatrix} I \\ Q \\ U \\ V \end{bmatrix} \tag{4.20}$$

where [R] denotes the rotation matrix.

When the scattering region is full of dust, Mie scattering is used to compute it (see subsection 3.2.3), and when the region is full of electrons, Thompson scattering is used (see subsection 3.2.1).

4.3.2 Emission regions

STOKES offers the possibility to choose between a cylindrical and a double cone geometry for the emission region. It is designed to emulate the three main regions of AGN: the accretion disk the continuum, the BLR and the NLR. The continuum is defined by a power law $F_\nu \propto \nu^{-\alpha}$, and the user choose the value for the spectral index α. For the BLR and the NLR the user defines the lines. For all prescriptions, there are a series of parameters that can be included as dimensions, spectral index, speed and for the case of lines, the width and wavelength. For details see Table 4.1.

Each photon emitted from the source region has a random direction and wavelength, according to the parameters chosen. For the line photons a Lorentzian profile is applied. The initial direction of the photon is determined by the polar angle, θ, and the azimuthal angle, ϕ, defined with respect to spherical coordinate system (Fig. 4.2- Top).

4.3.3 Scattering regions

The code allows the user to define three geometries for scattering (Fig. 4.2-Bottom): cylindrical, torus, and double conical. All of them are constructed in a Cartesian coordinate system. One can also define a sphere (or multiple spheres) that are not centered at (0,0,0).

All scattering regions may be filled with free electrons or dust, both characterized by the optical depth (τ), which is user-defined. Electron scattering is taken into account as Thomson scattering, dust scattering is computed from Mie theory.

The code assumes spherical dust grains of radius a and with a size distribution following a power law a^s as prescribed for the standard dust for the Milky Way or

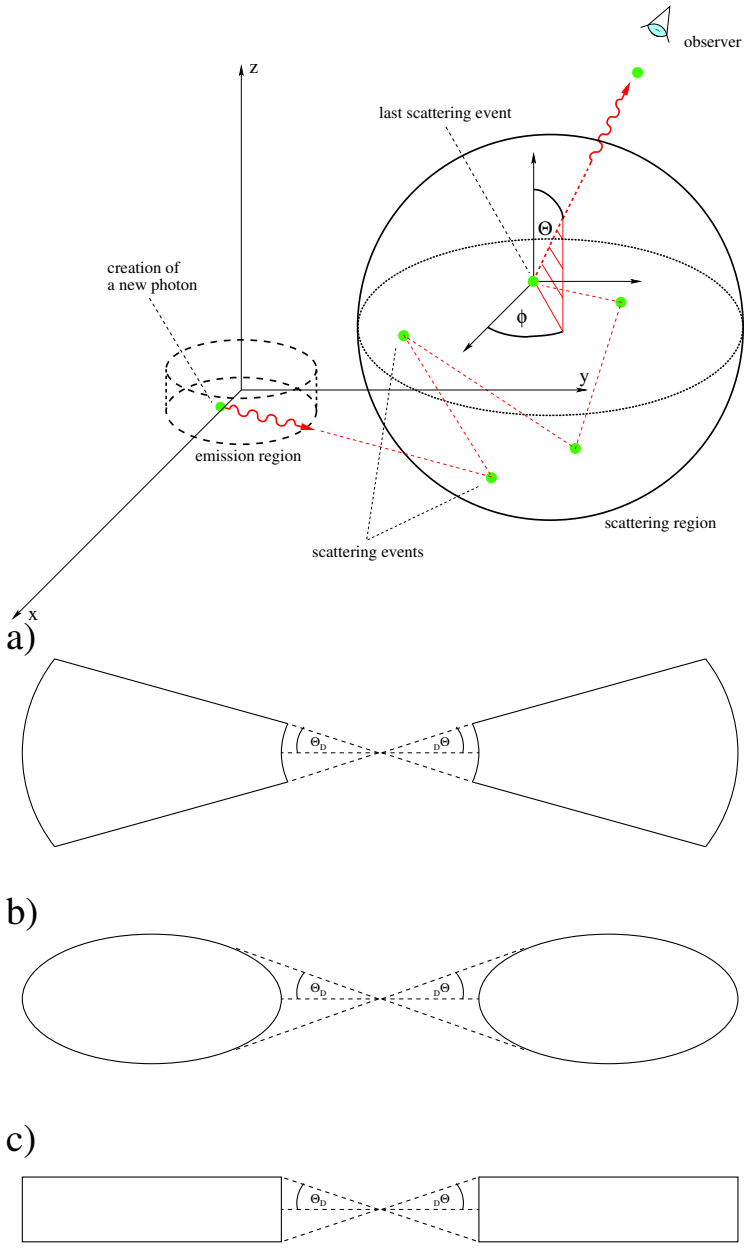

Figure 4.2: *STOKES* geometries (Goosmann and Gaskell, 2007). *Top:* Scheme of the coordinates system, the source region, the scattering region and the photon trajectory. *Bottom:* Scheme of *STOKES* scattering geometries: a) flared-disk, b) classical torus, c) cylinder.

the Magellanic Clouds (Mathis et al., 1977), that are based on silicates and graphite. The user chooses the size of the grains (maximum and minimum), the power law index s and the abundance of graphite and silicates. The Mie data was computed using the code of Bohren and Huffman (1983) and the dielectric functions for graphite and silicates are taken from Draine and Lee (1984).

4.3.4 The time-dependent modeling

The versions of the *STOKES* code we use here have the advantage of counting the time it takes for all scattered photons to reach the detectors, for all viewing angles. To calculate the time-lag, the code compares the path between the direct flux from the central source and the photons that have scattered from the region of dust and/or electrons. In this way a photon that does not experience scattering will result in a null time delay. *STOKES* compute the average time and allows the user to set the size of the time interval to be recorded. The delay is expressed in pc/c and represents the light travel distance.

4.3.5 Other parameters and outputs

The user selects the spectral range and the corresponding resolution, θ and ϕ viewing angles. The angle θ is measured between the line of sight and the z-axis, while ϕ is measured between the projected line of sight onto the xy-plane and the x-axis (Fig.4.2-Top). *STOKES* also requires to declare the resolution of the photons' arrival time. The total number of photons to be sampled needs to be defined, the higher this number the better statistics and the larger total CPU time to invest. A summary of the input parameters of *STOKES* are shown in Table (4.1).

The code output is a set of files containing the Stokes parameters as function of wavelength, time and viewing directions. This set of files is processed by the auxiliary routine "Analyze" to also obtain the total and polarized flux, the polarization position angle, the percentage of polarization, the time lag, and the number of dust and electron scattering.

For computational reasons it is necessary to also define a 'Gap' parameter. This is an additional spatial shift along the flight direction that is systematically added when photons enter or leave scattering regions. It accounts for numerical inaccuracies in the computation of the limiting surfaces of the scattering regions that otherwise may lead to a wrong judgment on the photon's position being either inside or outside the region. The Gap parameter must be small with respect to the spatial extension and optical depth of the scattering region in order not to influence the results.

Table 4.1: *STOKES* Parameters. From Table 2.3 of the *STOKES* v1.2 manual.

***STOKES* PARAMETERS**

DUST PRESCRIPTION

Command	**Parameters**	**Function**
GrainRadMin	r_{min}	minimum grain radius of the dust model
GrainRadMax	r_{max}	maximum grain radius of the dust model
GrainSizeInd	α_s	grain size index of the dust model
DustComp	*graph-orth graph-para silicate*	Abundances for the dust components (percentages)
GrainRadNum	N_{rad}	number of grain radii considered for the dust model
GrainLambdaNum	N_λ	spectral resolution considered for computing the dust model
DustModel	dust-file-name	file name of the dust model

PARAMETERS FOR SOURCE REGIONS

Command	**Parameters**	**Function**
PhotonNum	photon-number	number of photons to sample
ContSource	R a b c α v_{type} $v_{r,\rho}$ v_ϕ $v_{\theta,z}$	define continuum emission region, set spectral index α and 3D velocity
BLSource	R a b λ_θ Γ strength v_{type} $v_{r,}$, v_ϕ, $v_{\theta,z}$	define broad line region, set line centroid, width (both in Å), relative strength (percentage), and 3D velocity
NLSource	r_1 r_2 θ_0 λ_0 Γ strength v_{type} $v_{r,}$ v_ϕ $v_{\theta,z}$	define narrow line region, set line centroid, width (both in Å), relative strength (percentage), and 3D velocity

GENERAL PARAMETERS

Command	**Parameters**	**Function**
OuputFile	output file name process	set output file name and number of process
ThetaViewAng	number-theta	set number of viewing angles in i
PhiViewAng	number-phi	set number of azimuthal viewing angles
LambdaMin	min-wavelength	minimum continuum wavelength in Å
LambdaMax	max-wavelength	maximum continuum wavelength in Å
SpectRes	number-channels	number of channels for each detector
ResX	x-resolution	horizontal detector resolution
ResY	y-resolution	vertical detector resolution

PARAMETERS FOR SCATTERING REGIONS

Command	**Parameters**	**Function**
Cylinder	R a b c "dust"/"electrons" ρ v_{type} $v_{r,\rho}$ v_{ϕ}, $v_{\theta,z}$	define cylindrical scattering region with dust/electron density ρ, and 3D velocity
Torus	R a b c "dust"/"electrons" ρ v_{type} $v_{r,\rho}$ v_{ϕ}, $v_{\theta,z}$	define toroidal scattering region with dust/electron density ρ, and 3D velocity
Double-cone	r_1 r_2 θ "dust"/"electrons" ρ v_{type} $v_{r,\rho}$ v_{ϕ}, $v_{\theta,z}$	define double-conical scattering region with dust/electron density ρ, and 3D velocity
Flared-disk	r_1 r_2 θ "dust"/"electrons" ρ v_{type} $v_{r,\rho}$ v_{ϕ}, $v_{\theta,z}$	define flared-disk scattering region with dust/electron density ρ, and 3D velocity
Sphere	x_0 y_0 θ "dust"/"electrons" ρ v_{type} $v_{r,\rho}$ v_{ϕ}, $v_{\theta,z}$	define spherical scattering region with dust/electron density ρ, and 3D velocity
Gap	dx	computational parameter: photon displacement, must be small compared to dimensions and mean free path lengths of scattering regions

Chapter 5

Radiative transfer in different geometries

The work of this thesis consists of a set of radiative transfer simulations for different geometries of the internal region of an AGN, considering the time dependence on polarized radiation in the UV and optical bands. In this chapter the reader will find a set of simulations with the aim of analyzing the response to radiative transfer, between photons and the scattering regions, including time-dependent polarization.

Following the observational example of Gaskell et al. (2012), we attempt here to investigate the details of the inner AGN structure by studying the expected time lag between the total and the polarized continuum flux. The presence of the obscuring torus on the line-of-sight and, eventually, its geometrical shape and composition may be derived from the time lag.

The goal of this research is to investigate this new methodology, namely the reverberation in polarized radiation to indirectly resolve the most internal regions of AGNs. For this purpose different components were modelled, such as the circumnuclear region, polar winds and BLR, studying their temporal response in polarization as a function of inclination and/or wavelength. We applied an extended version of the radiative transfer code *STOKES* that includes the time information of a registered photon.

The first models give us an example of how polarization responds to different regions considering non standard parameters and simple and isolated geometries. Complexity was gradually added until a model based on the characteristics observed (or inferred), for the archetype of type-1 AGN NGC 4151, was developed.

5.1 Geometry models

The first step was to consider two types of geometries for the circumnuclear region: the so-called "dusty-torus", which is a toroidal region with an elliptical cross section; and a "flared-disk", with a wedge shape cross-section. As a second test, the flared-disk model was split into two zones to compare different densities. After that both geometries were tested, torus and flared-disk, with two kinds of dust prescriptions and two kinds of dust distribution: uniform and clumpy. When increasing

complexity, we added ionized winds filled with electrons in the form of a polar cone, the so called "polar outflows". Finally, the last part of the investigation consisted in incorporating a "scattering ring", a small region in the equatorial plane found between the central source and the circumnuclear region. We shown below in Fig. 5.1, a scheme of the different regions and geometries.

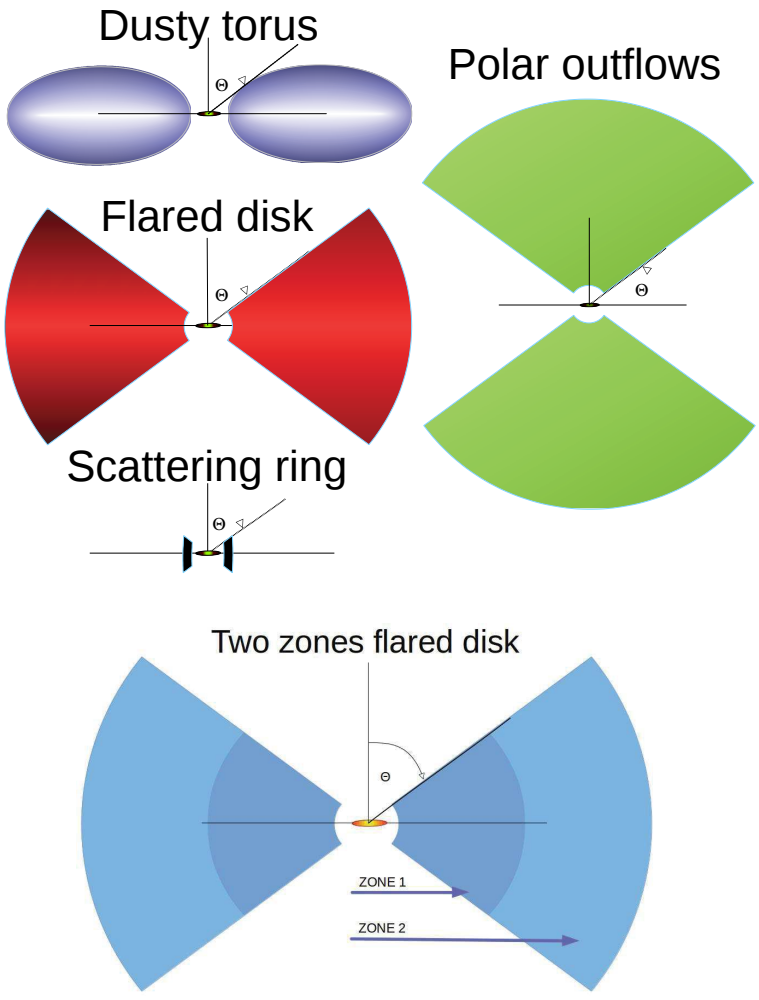

Figure 5.1: Geometry models scheme.

For all dust regions, we assumed an inner radius of 8 light days as found by Gaskell et al. (2012) for the case of NGC 4151, albeit without detailed modeling. The outer radius of the torus and its half opening angle were based on the findings by Ruiz et al. (2003) who conducted near-IR polarimetry observations of the same object. The outer radius of 15.0067 pc and the half opening angle of 60° were defined

from the disk symmetry axis. For all models, a point source at the center that emits an unpolarized flux with a power law spectrum $F_\nu \propto \nu^{-\alpha}$ with $\alpha = 1$ was considered.

5.1.1 Model 1: Torus and flared geometry

The initial test model was defined with two kinds of geometries, the "dusty-torus" and the "flared-disk". The region was filled with dust grains with an optical depth of ~ 1. The dust was defined by the so called AGN-dust (Gaskell et al., 2004) which consists of 85% silicates and 15% of graphite with a grain size between 0.005 μm and 0.2 μm.

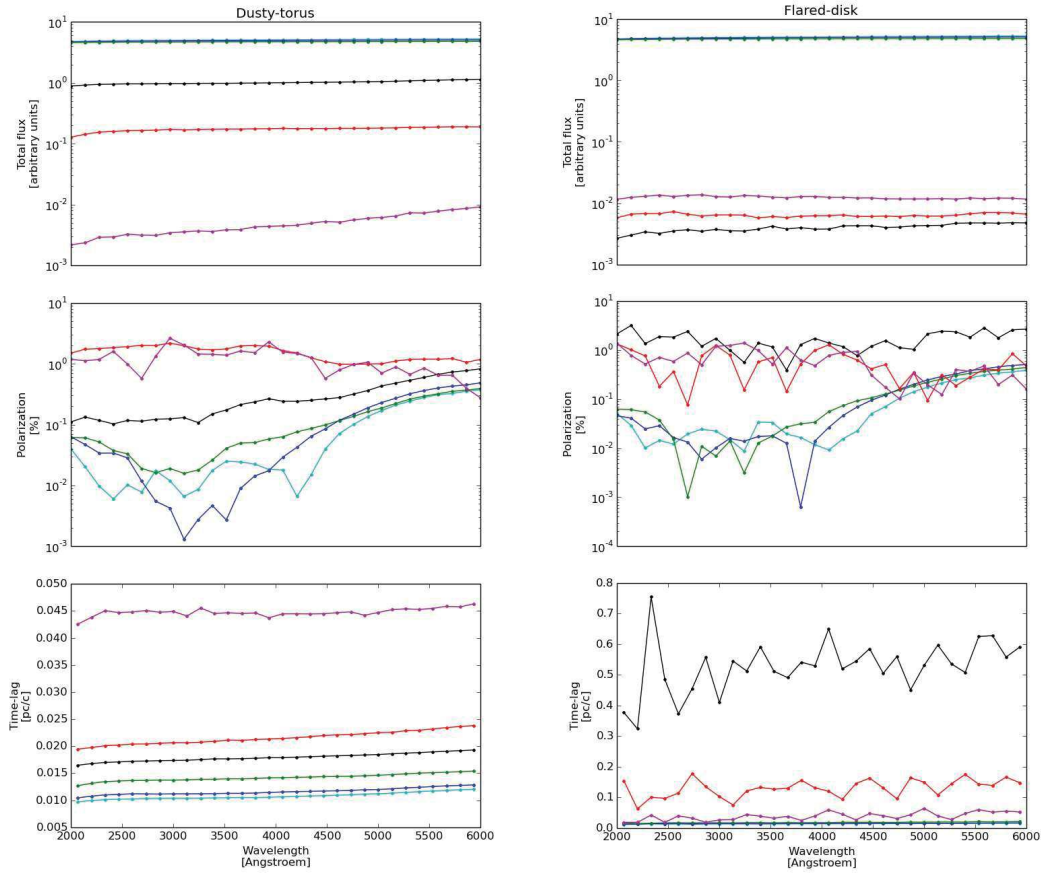

Figure 5.2: Results from *STOKES* for torus and flared geometries. *Left:* a uniform-dusty-torus model. *Right:* a uniform flared-disk geometry. For both geometries, total flux, degree of polarization and time lag for different viewing angles are shown. The magenta dots denote $\theta = 79.9$ °, the red dots $\theta = 71.0$ °; both represent a type-2 view. The black dots show $\theta = 61.64$ °, a view close to the torus horizon. Type-1 views are shown in green ($\theta = 51.3°$), blue ($\theta = 39.19°$) and cyan ($\theta = 28.9°$).

Fig. 5.2 shows the result from *STOKES* for both the dusty-torus (left) and the flared-disk (right) as a function of wavelength. For both models, the flux declines and the time delay increases from face-on (cyan, blue and green) to edge-on (red and magenta) viewing angles. However, the change is much more dramatic for the flared-disk geometry.

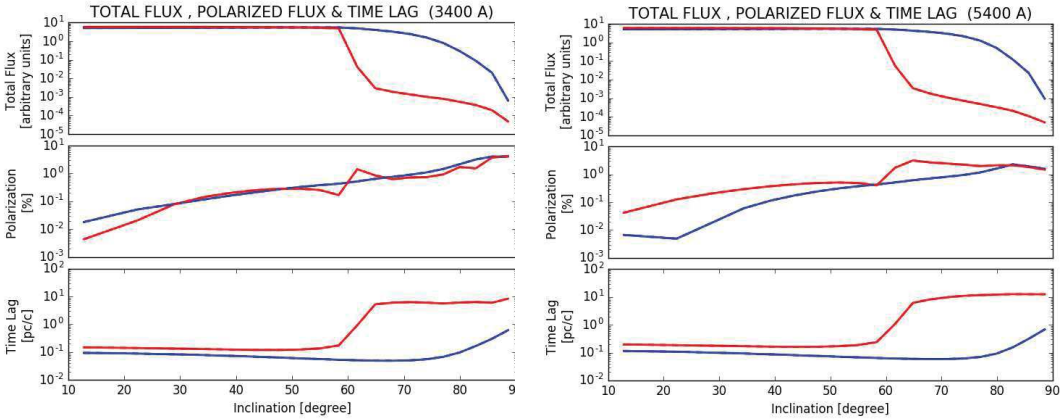

Figure 5.3: Comparison for *STOKES*' results between uniform dusty-torus (blue line) and uniform flared-disk (red line) geometries. Top to bottom: Total flux, polarization degree, and time lag as a function of viewing angle. *Left:* U band (3400Å). *Right:* V band (5500Å).

Fig. 5.3 shows the results of *STOKES* but, this time as a function of viewing angles for the U (left) and V (right) bands. The graphs show total flux, percentage of polarization and time-lag for different inclinations. This way, the difference in total and polarized flux for type-1 or type-2 is even more clear. While for low inclination, both models present almost the same level of total and polarized flux, the change around the surface of the scattering region (60°) is much more abrupt for the flared-disk, reaching higher delay values and lower flux rates at higher inclinations, while the torus model presents a more gradual change, reaching a lower delay and a higher total flux rate.

At face-on viewing angles, both models show the same shape for total flux, polarization degree and time lag. The total flux is almost the same for torus and flared geometries because, at these viewing angles the radiation predominantly comes from the central source.

At edge-on, we observe a decreasing flux level with a rising inclination. The obscuration is more efficient for the flared-disk than for the dusty-torus dust region. The polarization degree gains slowly with an increasing viewing angle. This difference is related to the shape of the inner surfaces. For a torus, the inner surface is convex, while for the flared-disk it has a concave shape. As discussed in Goosmann and Gaskell (2007) when comparing the obscuration efficiency between a compact

and an extended dusty-torus, it turns out again that a convex shape of the inner surface makes it more likely for a photon to escape after only a few scattering events. Therefore the accumulated time lag for the case of toroidal dust distribution remains low.

5.1.2 Model 2: Flared geometry with two zones of different densities

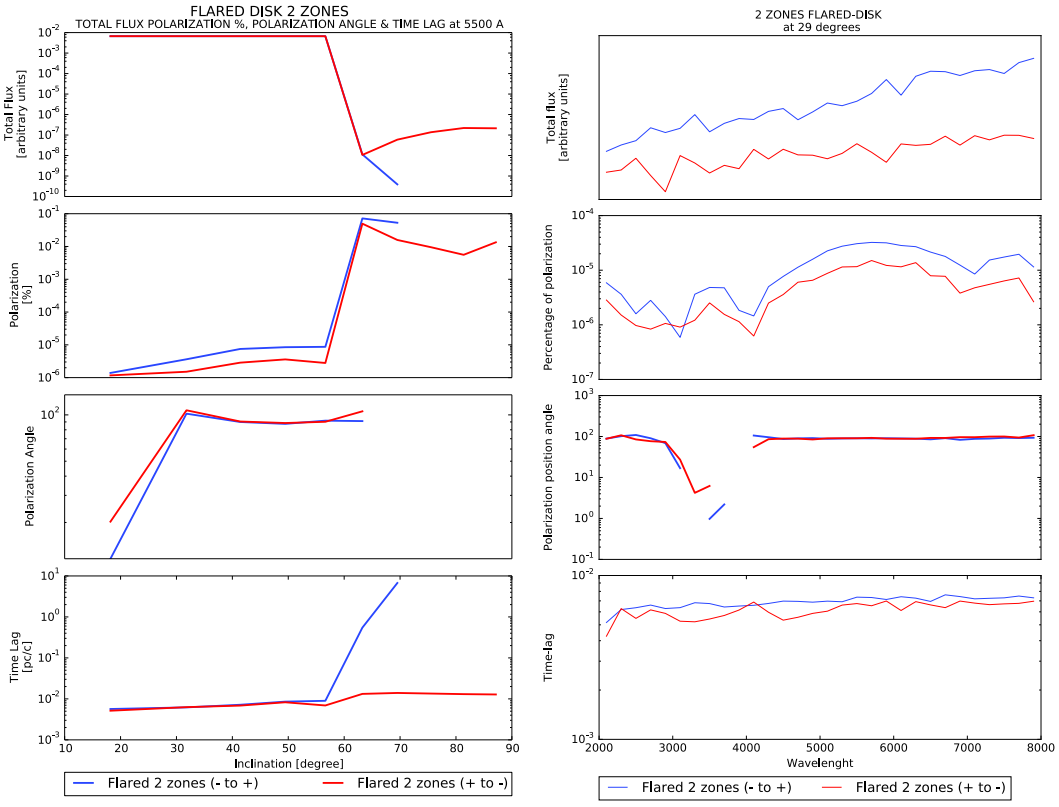

Figure 5.4: Results from *STOKES* for the 2-zone model. *Left:* Total flux, percentage of polarization, polarization angle and time lag for different viewing angles in the V band. *Right:* Total flux, percentage of polarization, polarization angle and time lag for different wavelengths at $\sim 29°$. The blue line represents the model with low dust density close to the source and a dense region in the outer parts. The red line represents the model where the first zone is denser than the outer one.

This model consists of a flared disk composed of two regions of different dust density. The flared disk is defined by a half opening angle of 60°, an inner radius of 0.0067 pc, an intermediate radius of 7.5 pc and an outer radius of 15.0067 pc. The total optical depth is τ—0.88. For this geometry, two scenarios were tested: in the first one, the inner zone was five times denser than the outer one; in the second one,

the outer zone was five times denser than the inner one.

The results are shown in Fig. 5.4. The flux is higher for type-1 views that are seen face-on because we can see directly the emission region. The inclinations obscured by the torus (type-2, edge-on to the observer) show less flux due to scattering and absorption. Comparing both models, there are almost no differences in the response of the system in terms of total flux, polarization percentage and polarization angle. This means that most of the scattering is produced close to the inner radius of the circumnuclear region. However, the response in time lag is different: for the second model with high density in the outer region, the time lag does not depend on inclination.

At face-on inclination, the flux and time lag are almost the same for both dust density distributions. This is due to almost all photons coming directly from the source, which can also be inferred by the low level of polarization. The difference in flux, as shown on the right hand side of Fig. 5.4 for an inclination of 29°, is small; the flux is larger for the model with a less dense inner zone because photons are then less absorbed near the core.

At edge-on viewing angles, the time-lag increases with inclination for the model with a less dense inner zone. More scattering is produced inside the zone-1 due to its low density which allows photons to go inside this region. Exactly the opposite happens when the dense region is in zone-1, a smaller number of scattering events are registered and the inflection point happens at around 60° where the circumnuclear region is defined.

5.1.3 Model 3: Torus and flared geometries with two kinds of dust prescription

The flared-disk and toroidal geometries were modelled as shown in Fig 5.1 assuming uniform-density dust distributions. The dust is opaque, with a radial optical depth of ~ 150 inside the equatorial plane. The modeling results can be evaluated over the optical wavelength range and as a function of the observer's viewing angle.

For the circumnuclear region two types of dust model were used: the AGN and the classical MRN (Mathis, Rumpl and Nordsieck from Mathis et al., 1977) also named Milky Way-dust. AGN-dust is composed of 85% of silicates and 15% of graphite, the grain radius lies between 0.005 μm and 0.2 μm with a distribution $n(a) \propto a^s$ with $s = -2.05$, while Milky Way-dust is composed of 62.5% of silicates and 37.5% of graphite. The grain radius lies between 0.005 μm and 0.25 μm with $s = -3.5$.

The new simulated observable added in this work, the time lag of the polarized emission, is not much affected when modifying the dust prescription (Fig. 5.5). The

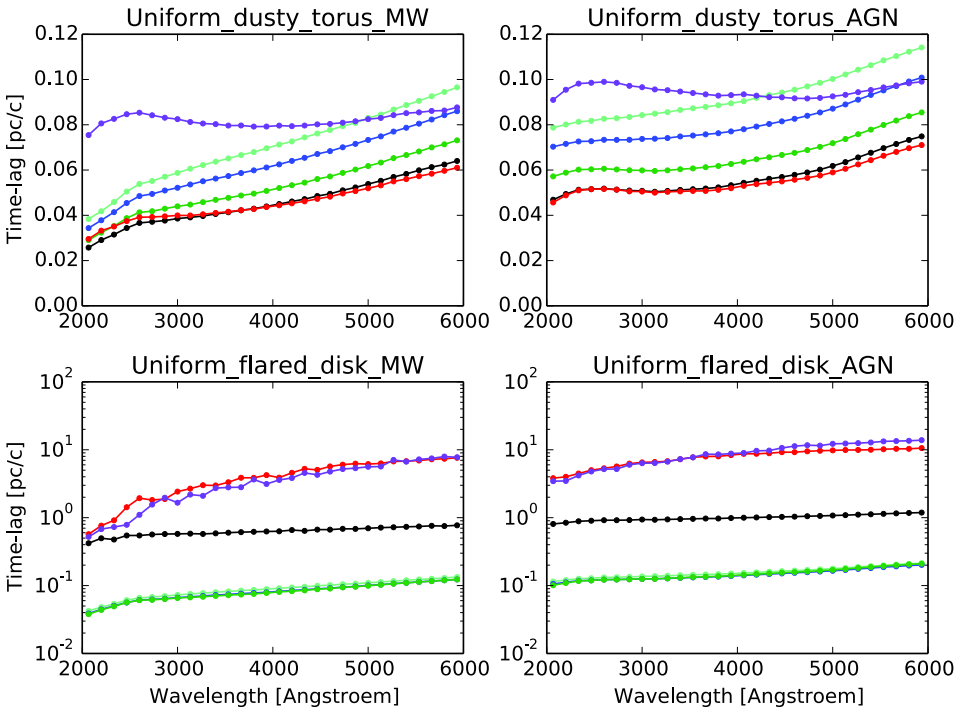

Figure 5.5: Comparison of the time lags induced by Milky Way and by AGN dust prescriptions for the case of a uniform dusty-torus and a uniform flared-disk. The plots show time-lags as a function of wavelengths for different viewing angles: the magenta dots denote $\theta = 79.9$ °, the red dots $\theta = 71.0$ °, which represent a type 2 view. The black dots show $\theta = 61.64$ °, a view close to the torus horizon. Type 1 views are shown in green ($\theta - 51.3°$), blue ($\theta - 39.19°$) and cyan($\theta - 28.9°$) (Rojas Lobos et al., 2018).

small differences between both cases are due to the specific albedo and scattering phase functions of both dust types. Since there is no major impact on the results, from now on we restrained ourselves to use the standard Milky Way-dust.

5.1.4 Model 4: Torus and flared geometries with uniform and clumpy dust distribution

After the existence of circumnuclear dust was established by the unified model, the idea that this dust was distributed in the form of molecular clouds was soon suggested (Krolik and Begelman, 1986; Krolik and Lepp, 1989; Fukue and Sanbuichi, 1993; Loska et al., 1993). Several models including clouds have been studied and observational evidence is largely consistent with a fragmented torus (López-Gonzaga and Jaffe, 2016, and references therein). For this reason we incorporate clouds in the

form of spheres as allowed by *STOKES* and as implemented by Marin et al. (2015).

Keeping the same geometry as defined previously, the circumnuclear region was, this time, filled with two types of dust distributions: uniform and clumpy. Once again, for both types of distribution, the dust is opaque, with a total radial optical depth of $\tau \sim 150$ inside the equatorial plane. The dust distribution in the clumpy model is made up of thousands of spheres. Each one has a filling factor of 25% (Marin et al., 2015). The radius of the spheres is 0.2 pc for the torus geometry, while for the flared geometry it is 0.65 pc.

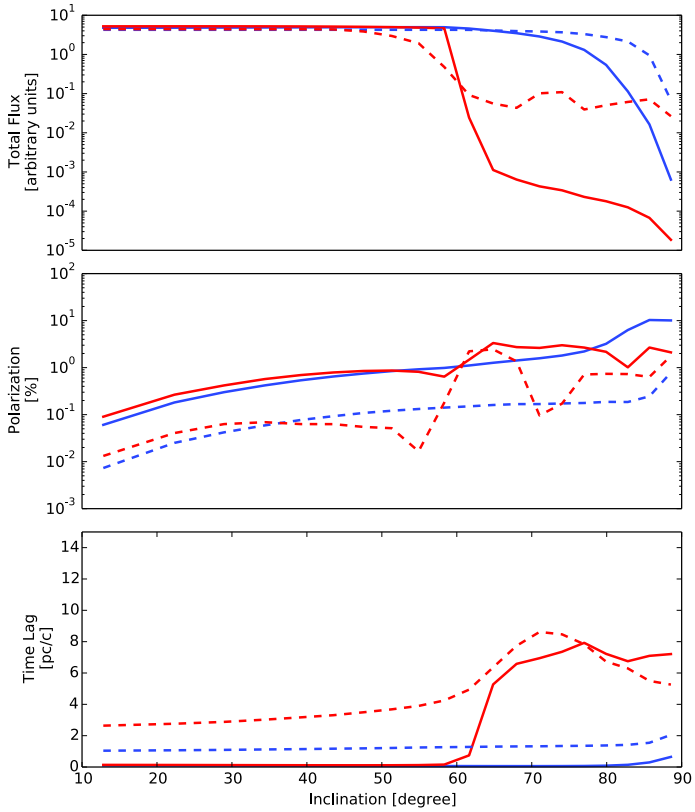

Figure 5.6: *STOKES* result for uniform and clumpy dust distribution. The plots shows integrated flux, percentage of polarization and time lag for different viewing angles. The blue line represents the uniform dusty torus model, the blue dashed line the clumpy dusty torus, the red line the uniform flared disk and the red dashed line represents the clumpy flared-disk.

The results of our models are plotted in Fig. 5.6. At face on inclinations, all four models show roughly the same spectral shape in total flux, polarization degree and time lag. The flux is almost the same for all four morphological setups because at these viewing angles radiation predominantly comes from the central source. Still,

a face-on observer finds a higher time-lag and a lower polarization degree for the clumpy dust distribution than for the uniform density cases. This is due to radiation scattered into the type-1 lines of sight. In a clumpy circumnuclear environment, the escaping photons, on average, go through a higher number of scatterings before they end up on a type-1 line of sight (Marin et al., 2015). For optically thick, uniform-density regions, the scattered radiation at face-on viewing angles is mostly dominated by the first-scattering component that is more strongly polarized and accumulates less of a time lag.

At edge-on viewing angles, we see a decreasing flux level. The obscuration is more efficient for the clumpy distribution than for uniform-density dust regions. The polarization degree increases slowly with an increasing viewing angle for all four geometries. With all type-2 viewing angles, the time lag accumulated for a clumpy or uniform torus geometry is much lower than for the case of a flared dust distribution. This difference is related to the shape of the inner surface, as discussed previously (end of 5.1.1). Therefore, the accumulated time lag for the case of toroidal dust distribution remains low even when the distribution is clumpy.

In the case of the flared geometry, the inner surface is parametrized as a sphere segment against which the photons are injected from the inside. In general, multiple backscatterings inside this sphere segment are necessary for photons to finally escape; if they go through, the escape cone is strictly limited by the half-opening angle of the flared-disk as measured from its symmetry axis.

Fig. 5.6 shows that the increase in time-lag and polarization degree is steep around this inclination for the flared dusty disk while for the toroidal geometry the increase is much shallower. For clumpy dust distributions, the horizons of the torus and of the flared-disk are more blurry, which diminishes the slope of the polarization degree and the time lag as a function of inclination even further.

5.1.5 Model 5: Changing the half opening angle of the torus and flared geometries

At this point, we used the same parameters for torus and flared-disk geometries as before, but with now half opening angles of 45° and 30° as measured from the disk symmetry axis.

In Fig. 5.7, we show the results from *STOKES* for these two half opening angle. The left side plot is for a half opening angle of 45° and the right one for 30° as measured from the disk symmetry axis, while Fig. 5.6 shows the case of a half opening angle of 60°. In the face-on case, that is of course reduced as the half opening angle has been decreased, the shape and values are almost the same, with only a few limited changes, such as the decrease in percentage of polarization for

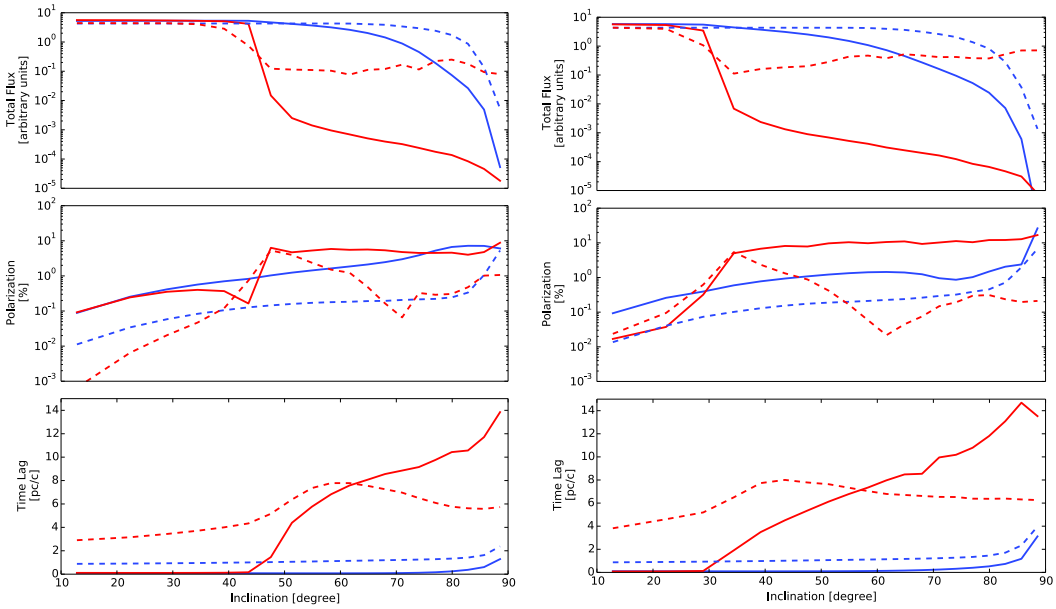

Figure 5.7: Comparison of the *STOKES* result for two different half opening angles of the circumnuclear region. The plots shows integrated flux, percentage of polarization and time lag for different viewing angles. The blue line represents the uniform dusty-torus model, the blue dashed line the clumpy dusty-torus, the red line the uniform flared disk and the red dashed line represents the clumpy flared disk. *Left:* half opening angles of 45°. *Right:* half opening angles of 30°.

the uniform flared geometry and a small increase in time lag for the clumpy flared geometry. A similar result is obtained for edge-on inclinations, with small changes in shapes or values of the flux, percentage of polarization and time-lag, but of course the region is more extended according to the circumnuclear region half opening angle.

5.1.6 Model 6: Adding polar winds to torus and flared geometries

We add an ionized wind stretched along the symmetry axis of the baseline model. The wind geometry was realized by a double cone filled with electrons having a ra dial optical depth of 0.03 or 0.3 (see Fig. 5.1). The wind has a common interface with the circumnuclear dust at the inclination of its horizon.

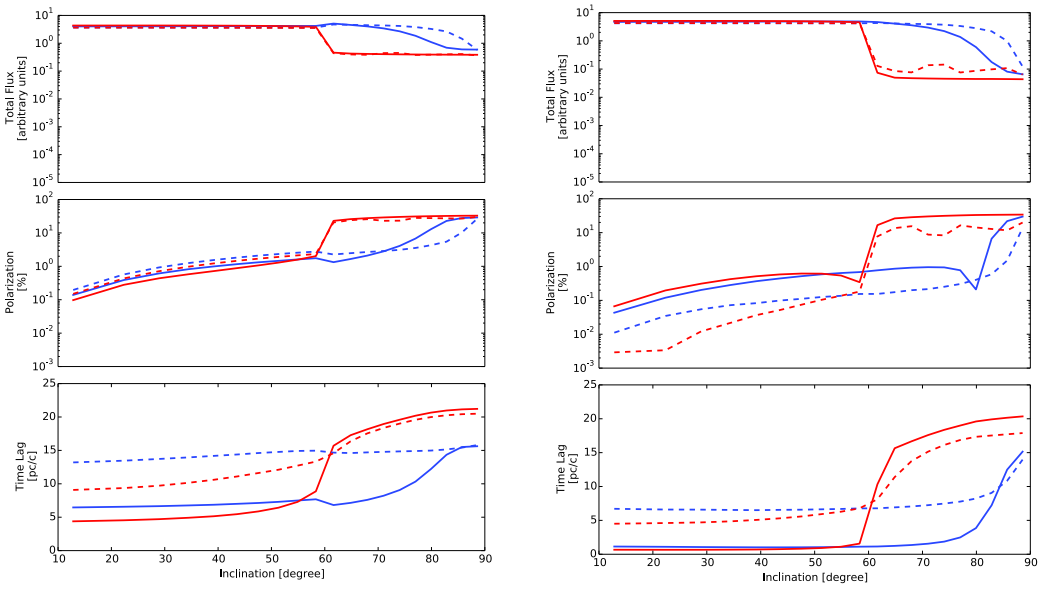

Figure 5.8: Comparison of the *STOKES* result for two densities for the polar winds. The plots show integrated flux, percentage of polarization and time lag for different viewing angles. The blue line represents the uniform dusty-torus model, the blue dashed line the clumpy dusty torus, the red line the uniform flared disk and the red dashed line represents the clumpy flared disk. *Left:* Baseline model with polar cones of optical depth $\sim \tau = 0.03$. *Right:* Baseline model with polar cones of optical depth $\sim \tau = 0.3$.

When adding a low density wind, the type 1 cases exhibit almost the same spectral flux level and polarization degree as for the baseline models (see Fig. 5.8). The additional scattering in the polar direction has a more significant impact on the time lag recorded at face-on viewing angles. It increases by a factor of roughly 2 when compared to the case without polar winds.

At edge-on, even a low-density wind scatters a significant fraction of the radiation surrounding the circumnuclear dust, and, therefore, decreases the strong absorption efficiency of the flared disk.

When we add winds, we find larger time delays with a smaller dependence on the viewing angle than for the base model. This is a consequence of the fact that before escaping, the photons pass through a second region of scattering that adds more scattering. and increases the path of the light.

5.1.7 Model 7: Torus and flared geometries with polar outflows and scattering ring

In this last model we use the same geometries for the circumnuclear region as previously, dusty-torus and flared-disk. We however, use slightly different parameters in order to better fit the observational constraints.

For the baseline model, the inner radius was extended to the region of sublimation. Using observational constraints provided by Kishimoto et al. (2013) for NGC 4151 in the near IR, we fixed the inner radius at 0.061 pc, and a new scattering region was added. As mentioned previously, this scattering ring represents the BLR. The outer radius is taken to be 15.061 pc in order to conserve the total length. The polar outflows have the same dimension as before; as this region is fully ionized, it should survive at a small distance to the center. The new element, the equatorial ring, is a flared geometry in the equatorial region between the central source and the circumnuclear dust, also fully ionized with a Thomson optical depth $\tau \sim 1$. The inner radius, according to the distance found by Gaskell et al. (2012) is ~ 8 ldys ($\sim$0.0067 pc). The outer radius was calculated to allow for a small gap between this and the circumnuclear region. The parameters of the models are summarized in Table (5.1). In Fig. 5.9 we plot the baseline model, the baseline model with polar wind, the baseline model with scattering ring and finally the baseline with both polar wind and scattering ring.

As for the previous models, the transition between type-1 and type-2 viewing angles is clearly visible in the total flux. The flux gradually decreases with a steepness that depends on the geometry and dust distribution. In all cases the flared-disk with uniform dust distribution shows the steepest drop, while the most moderate change corresponds to a torus geometry with clumpy dust distribution. Intermediate cases are obtained for clumpy-flared-disk and torus with uniform dust distribution.

The degree of polarization is almost invariant in all the configurations. However the time-lag and polarization angle are highly dependent on the dust distribution and the geometries. The polarization position angle remains at 90° (i.e. parallel to the projected symmetry axis) over all viewing angles for the baseline model and stays at 90° for models with a scattering ring. When we add polar winds, the polarization angle remains at 0° for all viewing angles. However for the model with polar wind and scattering ring, the polarization angle changes from 90° (parallel) at face-on view to 0° (perpendicular) at edge-on viewing angle.

We now include a third scattering region, an equatorial, ionized disk located between the source and the circumnuclear region. Compared to a model without an equatorial electron disk (Fig. 5.9 left), our new model shows that only the polarization properties of light and its time lag are affected (see Fig. 5.9 right). An additional scattering component that does not absorb radiation has almost no effect

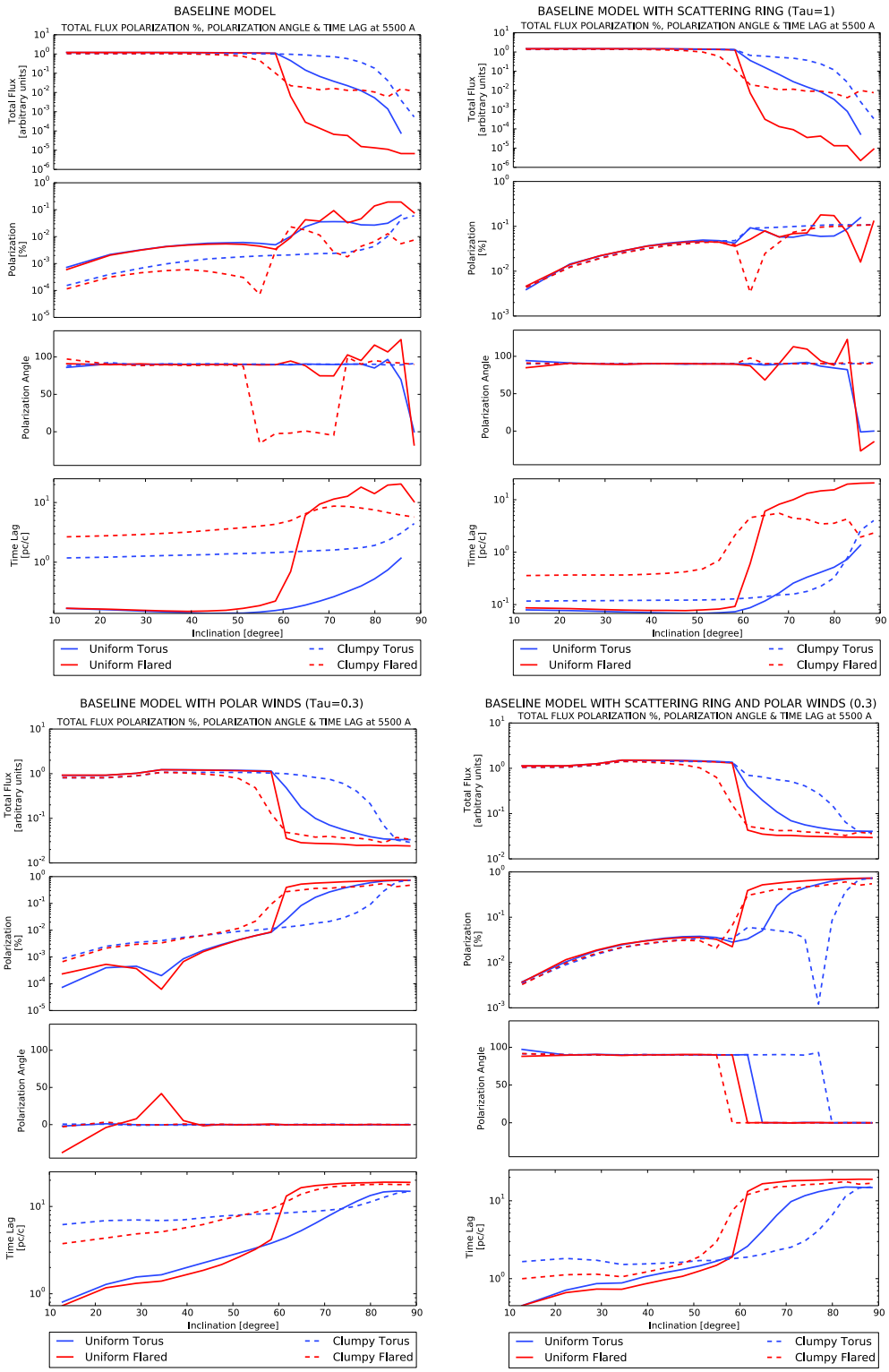

Figure 5.9: Result of *STOKES* for V band normalized flux, percentage of polarization, polarization angle and time lag for different viewing angles. The blue line represents the uniform dusty-torus model, the blue dashed line the clumpy dusty-torus, the red line the uniform flared disk and the red dashed line represents the clumpy flared disk. *Top left:* Baseline model. *Top right:* Baseline model with equatorial ring. *Bottom left:* Baseline model with polar wind. *Bottom right:* Baseline model with equatorial ring and polar winds (Rojas Lobos et al., 2018).

Table 5.1: Model setup, baseline. Parameters of three scattering regions with uniform and clumpy dust distribution for the Mie scattering and free electron distribution for Thomson scattering (Rojas Lobos et al., 2018).

MODELS	**TORUS**	**FLARED DISK**	**SCATTERING RING**	**POLAR WIND**
DUSTY				
Inner radius (pc)	0.061	0.061	0.0067	0.0067
Outer radius (pc)	15.061	15.061	0.0577	30.0067
Half opening angle	60°	60°	60°	30°
Equatorial optical depth	150	150	1	0.03 / 0.3
Scattering	Mie	Mie	Thomson	Thomson
CLUMPY				
Inner radius (pc)	0.061	0.061		
Outer radius (pc)	15.061	15.061		
Half opening angle	60°	60°		
Optical depth per clouds	50	50		
Clouds radius (pc)	0.2	0.65		
Filling factor	25%	25%		
Scattering	Mie	Mie		

on the flux level observed at various inclinations. However, the electron disk stabilizes the degree of polarization observed in type-1 viewing angles, independently of the circumnuclear dust structure. The disk also sets the polarization of radiation to 90° at type-1 orientations, as observed (Smith et al., 2004). More importantly, the proximity of this region to the central source means that the observed time lags are shorter for type-1 inclinations. A fraction of the input radiation, depending on the solid angle covered by the opening angle of the electron ring, is directly scattered towards the observer, inducing a shorter time lag. For higher inclinations, radiation passes through the optically thin medium and scatters inside the optically thick dust structure, so that the effect of the equatorial ring becomes almost undetectable.

When we include polar outflows in addition to this scattering ring (see Fig. 5.9 bottom right), we reach similar conclusions. The addition of an equatorial electron ring remains marginal in terms of total fluxes, but strongly helps the polarization degree and angle to stabilize at typical values seen for local AGNs (see Marin (2014)). The degree of polarization remains lower than 1% for type-1 inclinations and sharply rises for type-2 orientations. The polarization angle rotates from parallel to perpendicular as soon as the observer's line of sight is obscured by the circumnuclear dusty region. The effect of the scattering ring on the time lags at type-1 views is even stronger: the time lags are 5 10 times shorter.

5.1.8 Conclusions

We have developed a series of models of the different scattering regions, studying them separately and finally combining them to obtain a much more complex structure as a group, resembling what we understand to be the innermost region of AGNs. The new feature in this study, the temporal response of polarization, has proved to be an interesting tool, in our effort to identify and establish a dimensional scale of the components nearest to the core of the system.

The first result we obtain, although obvious, is the anticorrelation between the total flux and time delay. One can also recognize the difference in these two observables for face-on or edge-on viewing angles for almost all models. The photons that are scattered and/or absorbed decrease the total flux, while those that are scattered increase the time delay. The number of scatterings will depend on the geometry and the observation angle. At face-on viewing angles, more direct and less scattered flux reaches the observer.

We further saw that the time delay increases significantly for models with a clumpy circumnuclear region. This is because in this geometry, photons are more likely to encounter scattering regions, the clouds, which also allows the photons to pass inside the circumnuclear region before being scattered and experience multiple scattering.

The presence of the BLR modeled by an equatorial ring scattering region, decreases the time-lag and stabilizes the polarization angle. This is explained by the proximity of the inner radius to the central source, generating a polarized flux that has a reduced traveling path and in likelihood of a single scattering. The disk also sets the polarization of radiation to 90° at type-1 orientations, as has been observed (Smith et al., 2004).

With this study, we were able to understand the contribution to the time delay between the direct flux and the polarized flux provided by the different components. We found that when all components are included, with the parameters used here, the equatorial scattering ring imprints a dominant signature.

However, this study is not complete, as it cannot be directly verified by observations. Modelling allows us to discriminate between regions and to have an overview of all inclinations, which we cannot do in practice.

Nevertheless, the time dependent polarization gives us a new tool, which, together with other observables, including other parameters of polarization, allows us to elucidate the innermost regions of the AGNs.

Chapter 6

Reverberation and cross correlation

6.1 Reverberation in polarization

The concept of reverberation comes from acoustic where this effect takes places when a sound is reflected and the delayed wave interacts with the original one. Reverberation occurs when the reflected wave reaches the receptor before the original sound wave is over. It is different to the echo phenomenon, which happens when the reflected sound reaches the receptor after the original wave has gone. The time delay depends on the geometry and on the characteristics of the reflection surface. Following the same principle, Bahcall et al. (1972) suggested to use the time dependence of emission lines to determine the geometry of a photoionized nebula. It was soon realized that this technique could also be applied to quasar and Seyfert galaxies. But the first to use the term "reverberation" were Blandford and McKee (1982). They proposed that the lag between the continuum and the emission lines in Seyfert galaxies are due to light travel time effects.

As mentioned before (subsection 2.2.7), AGNs have large variability in almost all wavelengths (Sartori et al., 2018) and this variability is a key factor in the reverberation technique. The continuum emission, in the UV, optical, and near-IR, is produced by the accretion disk, and varies on scales ranging from hours to days, which are those that matter to us in this work, and can reach years. The same variability is observed in the broad emission lines (generated in the BLR), with a time delay due to the light travel time between the source, the BLR and the observer. As the accretion disk is very small ($<$0.01 pc for a 10^8 $M_\odot$ BH, Kishimoto et al., 2005), this delay corresponds approximately to the difference in distance traveled by photons, between the source of emission of the continuum and the region of emission of the broad lines, which is of order of the distance between the accretion disk and the BLR.

Since Gaskell and Sparke (1986) used the cross correlation function for the first time to compute the delay between the continuum and several spectral lines to determine the size of BLR for three Seyfert-1s, NGC 4151, Ark120 and Mrk 509, the reverberation mapping has been the most used and proven technique to determine the size of the BLR and the BH mass of several AGNs (Fausnaugh et al., 2017; Peterson et al., 2004; Wu et al., 2004; Peterson and Horne, 2004). Moreover,

using cross correlation between the continuum and several spectral lines, Gaskell and Sparke (1986) demonstrated the stratification of the BLR, in other words, they showed that the BLR is in itself divided into regions with a different ionization index.

One further step was made by Gaskell et al. (2012) who applied the reverberation mapping between the optical and polarized continuum of AGN NGC 4151. Using cross correlation techniques, they found a delay of $\sim$ 8 days between the source and the scattered emission. These authors suggested that scattering is produced by electrons in the low ionization zone of the BLR.

This was the inspiration of this research. Following Gaskell's work, the goal of this thesis project was to generate the numerical predictions of the polarization induced by the different components of the AGN (see chapter 5) in order to compare them with future observational campaigns of reverberation in polarization. The results and procedure are explained below.

Figure 6.1 shows the trajectory taken by the photons to reach the observer located in an arbitrary face-on angle in our "flared-disk" geometry. As before, θ is the angle defined from the symmetry axis and the scattering region, the "half opening angle". The blue line represents the photons that come directly to the observer from the source, and defines the viewing angle ϕ. The red lines represent the trajectory of the photons that has deviated as a result of an interaction in the scattering region. The angles between these two lines from the origin is α, as shown in the lower panel of Fig. 6.1 . Scattered photons travel a greater distance than direct photons, which causes a time delay. If we can determine the time delay (Δt) we can deduce the difference in the length (Δl) by simply using the speed equation $\Delta t = \Delta l/c$. The difference in distance Δl can be simply determined by trigonometry, as seen in Fig. 6.1. The path difference, for the flared-disk geometry, will be given by: $\Delta l = r(1 - \cos\alpha)$, as seen in the lower panel of Fig. 6.1. One can see that α depends on the viewing angle and its value ranges from $(\pi/2 - \phi)$ to $(\Theta - \phi)$. The minimum Δl for flared-disk geometry is obtained when $\alpha = \Theta - \phi$.

There are however some assumptions required for reverberation mapping to be effective: the continuum emission source is considered to be a point source; it must vary; and the light travel time is the source of the delay (Peterson and Horne, 2004).

6.1.1 The transfer function obtained with STOKES

In simple word, the standard reverberation mapping study constrains the structure and kinematics of the BLR by analyzing the response of the broad emission lines to the continuum. The key is to determine the transfer function, which is the response of the system to a single pulse. It is not always a simple task. For the classical case of reverberation mapping, assuming a linear response between the lines and

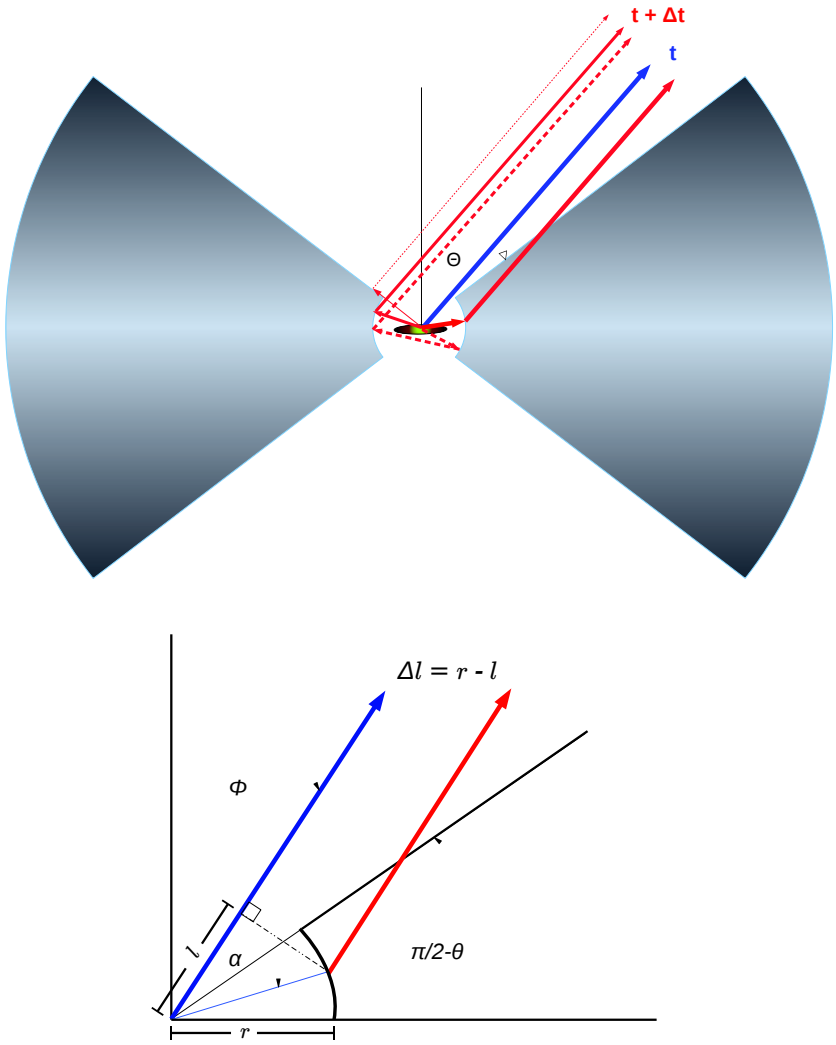

Figure 6.1: Diagram of the trajectory of the photons in reverberation.

the continuum, the line response, $L(v,t)$, as a function of time t and velocity v that corresponds to Doppler shift of the line, can be written as:

$$L(v,t) = \int_0^\infty \Psi(v,\tau)C(t-\tau)d\tau \tag{6.1}$$

where $\Psi(v,\tau)$ is the transfer function, and $C(t)$ is the continuum light curve.

In our case of reverberation in polarization, instead of the response of the lines, we simulate the response of the polarized flux with respect to the continuum. In this case, we know the transfer function which is the corresponding I, Q and U obtained from *STOKES*. From them, we can calculate the total flux, polarized flux, polar-

ization angle and so on. Note that the total flux, both for observational data and those obtained with our simulations, is the combination of the flux from the source and the polarized flux. It is not possible to observe the direct flux of the source in isolation; however when generating the light curves, we can distinguish between the source and the total flux as we will see in the following subsection.

The polarimetric results that have been presented in the previous chapter includes the average time lag. Let's remember that this average is calculated by *STOKES* by comparing the difference it takes to reach the observer between scattered photons and those that arrive directly from the source. This includes contributions from very different regions. Consequently, the time-lag obtained is due to the scattering average over all the volume of the regions studied. Note that this time lag average is not an observable, since it is not possible to determine the zero emission time, even at a type-1 viewing angle we also see a scattered component that adds to the direct flux.

With the aim to obtain a time lag that can be compared to observations, and therefore the minimum distance between the emission and scattering regions, it is necessary to apply the reverberation technique and build the corresponding light curves. I sought to establish the cross-correlation between them.

In order to determine the minimum distances we need to go one step further and increase the temporal resolution by focusing on short delays. To do this, *STOKES* was used to produce transfer function with a temporal resolution large enough to set a range of the light travel distance comparable to the distances of the internal structure of the AGN modeled here. The next step is to generate the light curves and then find the cross correlation between them.

It is worth pointing out that in the previous chapter we referred to time lag or time delay as the difference between the time it takes for photons to reach the observer directly from the source and those that are scattered. This is not an observable. In the following, we call time lag or time delay the difference obtained from the cross correlation between the light curves of direct flux and polarized flux. In this case this value is equivalent to that obtained from observations.

6.1.2 Generating artificial light-curves

The transfer functions of the Stokes parameters I, Q and U produced by *STOKES* must be processed to create the light curves. These functions are generated at time intervals of 0.0005 pc/c with a total sample of 4000 points. Again the Monte-Carlo method was used to generate the random source sampling.

The code reads I, Q and U (Fig. 6.2) as a function of time-lag and computes the light curves as follows:

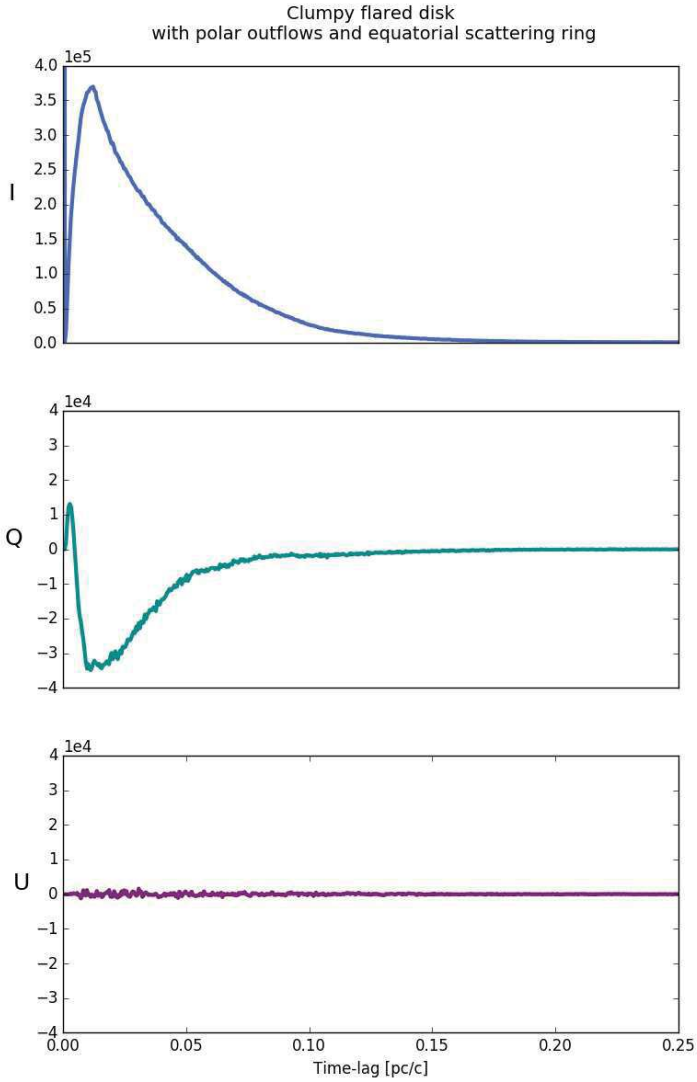

Figure 6.2: Transfer function from *STOKES* for a clumpy flared disk geometry with polar outflows and equatorial scattering ring. Top to bottom: Stokes parameters I, Q, U as a function of time-lag.

$$TF = \sum_i S_i \times I_{i+dt} \tag{6.2}$$

$$PF = \sum_i S_i \times \sqrt{(Q^2_{i+dt} \times U^2_{i+dt})} \tag{6.3}$$

where $S(t)$ is the source function generated by the Monte-Carlo method, which is a random light curve to represent the central source of the AGN. This step is

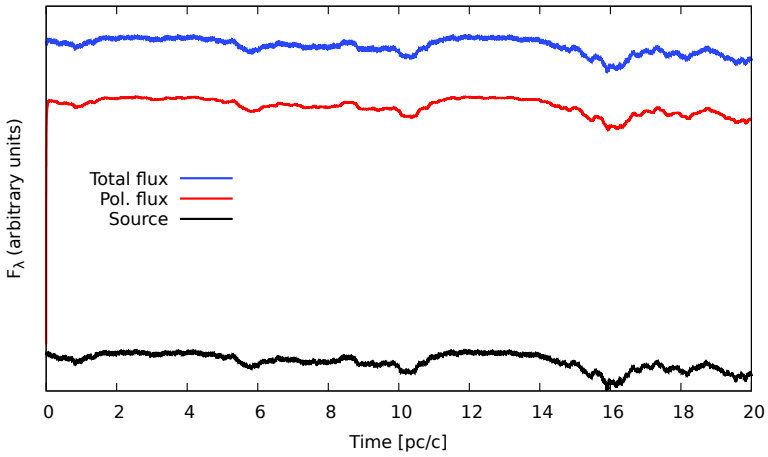

Figure 6.3: Total flux (blue), polarized flux (red) and source function (black) light curves, computed by the Monte-Carlo algorithm.

necessary to induce the variability observed in the AGN and also to detect the delay between the two light curves. To calculate the source function we use:

$$S_i(t) = S_{i-1} + r_i \times 2 \times var \tag{6.4}$$

where r_i are random numbers in the range [-0.5,0.5] and var is the variability factor, fixed at 0.07. We take N=40000 points over a time interval of 65.2 yr.

The timing properties (amplitude of the fluctuations in $S(t)$, characteristic noise) are, as can be seen from Fig. 6.3, in reasonable agreement with observations (see Fig. 2.3).

Fig. 6.2 shows the transfer functions I, Q and U resulting from *STOKES*. It can be seen that the total polarization is determined by Q and there is no contribution of U since we focus on electron scattering. Fig. 6.3 shows the source function (black line) and the respective light curves for the total flux (blue) and polarized flux (red). As said before, we have the light curve of the source since this is the curve generated randomly with the Monte-Carlo method.

6.1.3 The cross-correlation analysis.

Now that we have already generated our light curves, we are only left to find the cross correlation between them. The cross correlation function (CCF) represents the similitude between two time series. In our case it is the cross-relation between the light curve of the total flux, TF, and the light curve of the polarized flux, PF, which we can express as:

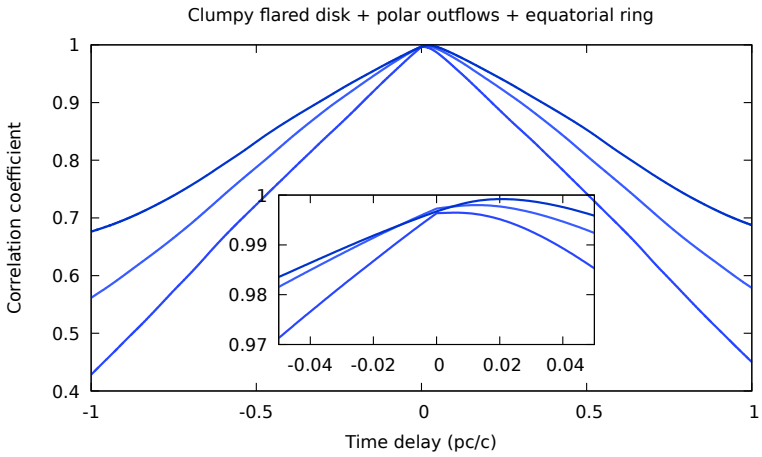

Figure 6.4: Cross correlations delays for clumpy flared disk geometry with equatorial ring and polar winds. Three CCF randomly generated for the same model are plotted.

$$CCF(\Delta t) = \int TF(t)PF(t+\Delta t)dt \tag{6.5}$$

As we have already calculated the TF (Eq. 6.2) and PF (Eq. 6.3) light curves, we now use the following to calculate the CCF curve in its discrete form:

$$CCF = \sum_i \frac{(TF_i - \langle TF\rangle) \times (PF_{i+dt} - \langle PF\rangle)}{\sqrt{(TF_i - \langle TF\rangle) \times (PF_i - \langle PF\rangle)}} \tag{6.6}$$

where $\langle\rangle$ denotes the mean value. It is interesting to note that we can also calculate the cross correlation between the source and the polarized flux, as well as compare it to the cross correlation between the polarized and total fluxes.

The maximum of the CCF curve was considered. The calculation was performed repeatedly, between ten and twenty times, because random fluctuations in the source curve also induces random fluctuations in the CCF. The final values provided in the next sections are the average, while the error corresponds to the standard deviation of the sample. An example is shown in Fig. 6.4, where three CCF curves corresponding to three different source light curves, for the same parameters of the model, of the same considered sample can be seen, as well as the differences between them.

6.2 Polarization reverberation in AGN models

The cross-correlation delays for the different geometries discussed in the previous chapter are presented in this section (see Fig. 5.1). Each region has been analyzed

separately, then together, to determine if it is possible to establish constraints on the geometry with this technique.

As in the previous chapter, the circumnuclear region has been modeled using two different geometries: "dusty-torus" and "flared-disk" and two kinds of dust distributions: uniform and clumpy. The dust prescription remains Milky Way-dust type. All results are presented for a type-1 inclination $\sim 29°$.

In the following, all geometries have the same dimensions and specifications as those used previously in model 7 (subsection 5.1.7); for details see Table 5.1.

6.2.1 Testing simulated polarization reverberation for ionized regions

We first considered scattering by a polar wind and an equatorial ring, both being ionized regions. The polar wind was tested with two optical depth: $\tau = 0.3$ and $\tau = 0.03$, while the equatorial ring was tested with $\tau = 1$ and $\tau = 3$. The result for V, B and UV bands are shown in Table 6.1.

Table 6.1: Cross-correlation delays for ionized regions

POLAR WIND AND EQUATORIAL RING (units: days)			
BAND	**V (5500Å)**	**B (4500Å)**	**UV (2500Å)**
Polar wind($\tau \sim$0.3)	870.2 ± 317.0	995.9 ± 373.9	533.7 ± 374.9
Polar wind($\tau \sim$0.03)	512.8 ± 305.2	1083.8 ± 221.0	437.2 ± 318.8
Equatorial ring($\tau \sim$1)	17.6 ± 4.4	21.4 ± 4.1	23.8 ± 5.0
Equatorial ring($\tau \sim$3)	10.9 ± 5.2	10.7 ± 3.6	12.8 ± 3.2

It is very interesting to analyze the response in polarization by comparing the two geometries that simulate a region of high ionization, treated in *STOKES* as Thomson scattering. On one hand, a polar wind with a very low optical depth and covering a large distance in the line of sight, and on the other hand, the equatorial region with a small size and an optical depth in the controversial limit $\tau \sim 1$.

The time delay obtained for the polar wind is far longer than the time scale considered in this study and decreases by a factor 2 when the distribution of dust is 10 times less dense. The polarization angle remains at 0° as expected when polarization is generated in the same direction as the line of sight. Note also that the polarization fraction is low, partly because of canceling of polarization for symmetry reasons and also due to the low density of the region. There are more photons that can cross it without being scattered. For this geometry the largest time delay is computed in the B band while it is much less in the UV band. In all cases we find a high dispersion of the average value.

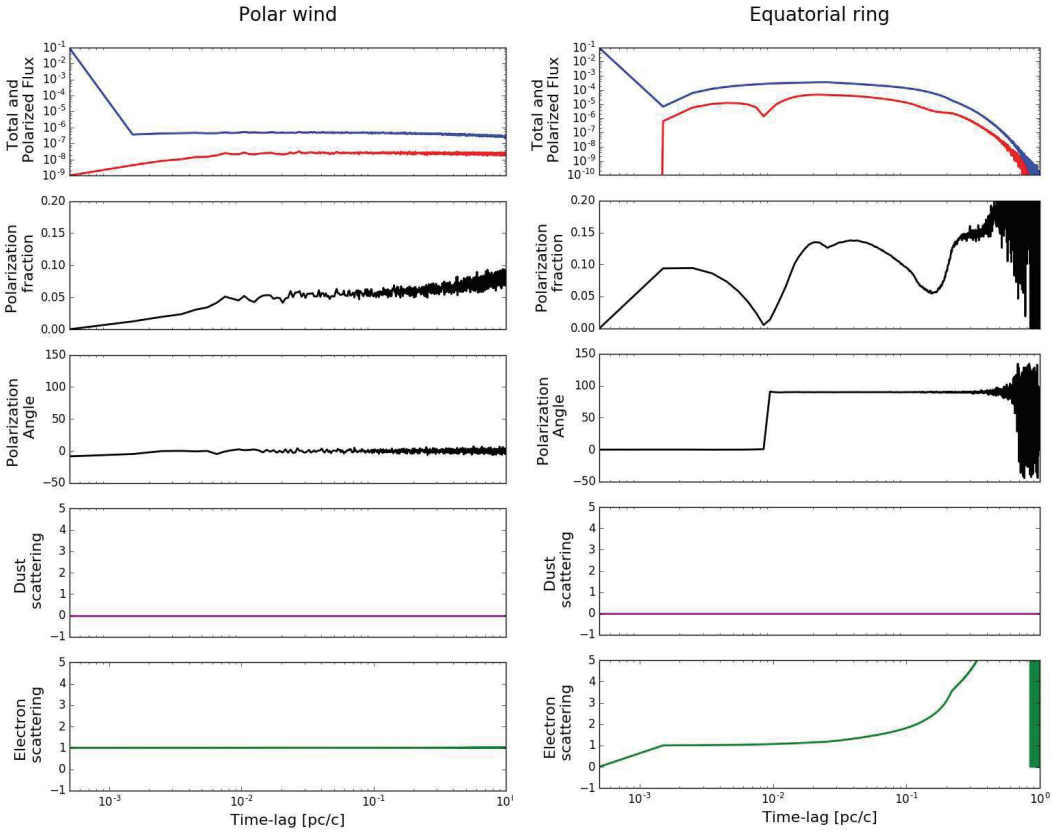

Figure 6.5: Transfer function obtained from *STOKES* for polar winds alone (left) and equatorial ring alone (right). *Top to Bottom*: total (blue) and polarized (red) flux, polarization fraction (black), polarization angle (black), number of dust scattering (magenta) and number of electron scattering (green) as a function of time-lag.

The opposite happens when scattering occurs in the equatorial region, the polarization angle is 90° at the peak of the CCF. It should be noted that the distance obtained by the CCF, 0.015 ± 0.004 pc/c (17.6 ± 4.4 light days)in the V band and 0.018 ± 0.003 pc/c (21.4 ± 4.1 light days) in the B band, is more than twice the distance from the inner radius of the model. This difference cannot be attributed to multiple scattering since, in this regime, only single scattering takes place as shown in Fig. 6.7. However, the answer seems to be in the density of the region and how far photons are able to penetrate before being scattered. When we increase the optical depth of the equatorial ring to $\tau \sim 3$, we can reproduce the internal radius of the model, 0.009 ± 0.004 pc (corresponding to 10.1 ± 5.2 light days) in the V band and 0.009 ± 0.003 pc (corresponding to 10.7 ± 3.6 light days) in the B band, (see Table 6.1).

6.2.2 Testing simulated polarization reverberation for dusty regions

We consider four configurations for the circumnuclear region: a uniform dusty torus, a clumpy dusty torus, a uniform flared disk and a clumpy flared disk.

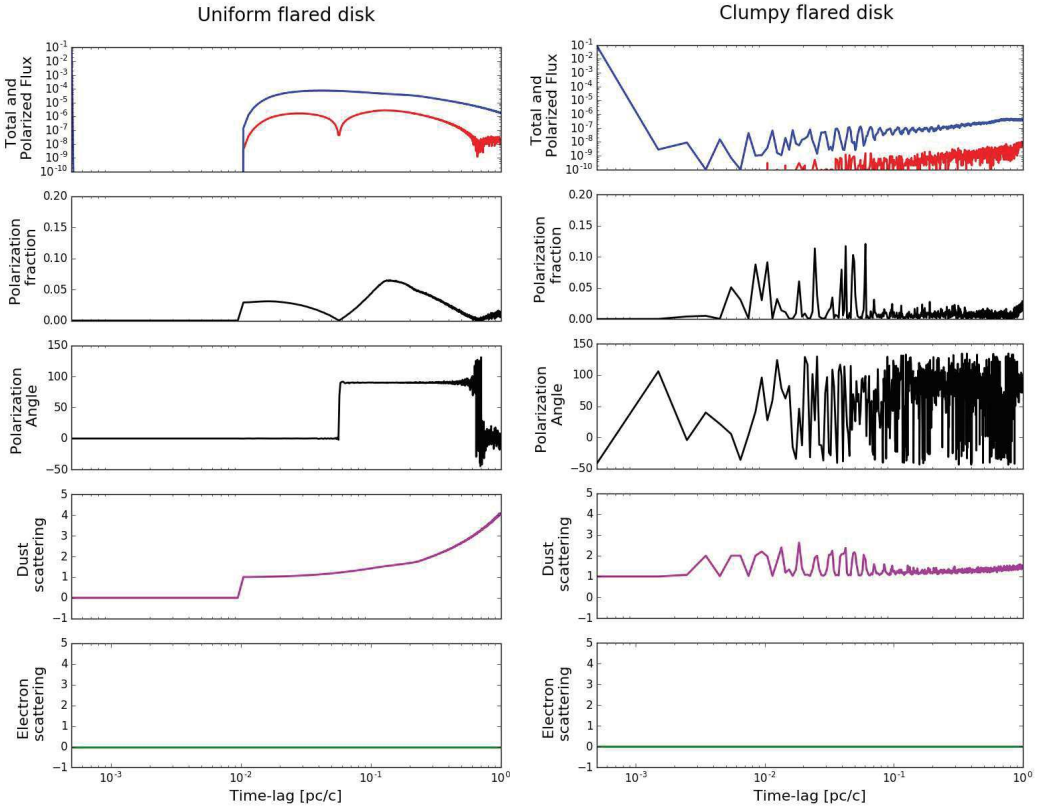

Figure 6.6: Transfer function obtained from *STOKES* for uniform flared-disk (left) and clumpy flared-disk (right). *Top to Bottom*: total (blue) and polarized (red) flux, polarization fraction (black), polarization angle (black), number of dust scattering (magenta) and number of electron scattering (green) as a function of time-lag.

Table 6.2: Cross-correlation delays for dust regions

CIRCUMNUCLEAR REGION (units: days)			
BAND	**V (5500Å)**	**B (4500Å)**	**UV (2500Å)**
Uniform dusty torus	75.3 ± 28.4	73.3 ± 19.0	49.7 ± 17.2
Uniform flared disk	67.6 ± 24.1	69.0 ± 20.8	49.4 ± 16.8
Clumpy dusty torus	587.3 ± 222.3	664.1 ± 101.1	616.5 ± 49.6
Clumpy flared disk	1571.3 ± 460.3	1574.9 ± 98.6	1507.6 ± 665.9

For both geometries with uniform dust distribution, the values obtained for the

cross correlation between the direct flux and the polarized flux are in perfect proportion with the size of the inner radius. Let us recall that the internal radius for the defined geometries is 0.061 pc while the inferred distances are 0.063± 0.024 pc (corresponding to 75.3 ± 28.4 light days)for the dusty-torus and 0.057± 0.020 pc (corresponding to 67.6 ± 24.1 light days) for the flared disk. Considering these results we can conclude that if the circumnuclear region was isolated, and the distribution of dust was homogeneous, it would be possible to determine its size by reverberation in polarization. The results for cross-correlation for the circumnuclear region are shown in Table 6.2.

However, the picture is totally different for both geometries if we consider dust distribution in the form of spherical clouds. In this case, the results obtained are of the order of 8 and 19 times larger than the inner radius, for the dusty-torus and flared-disk geometry respectively. In the case of a cloud distribution, there is no direct way to find the internal radius, since more parameters must be considered such as the number of clouds in the viewing path, their density and distribution. In this case, the photons can penetrate deep inside the circumnuclear region and experience several scattering events before reaching the observer, which explains such a high delay time.

For the scattering produced by dust, while there are no significant differences between the V and B bands, there is an important decrease in the time lag for the UV band, which is most evident for the uniform distribution of dust. This is because in this regime the wavelength approaches the size of the dust grains, favoring dispersion even from the boundary of the scattering region.

The transfer functions (Fig. 6.6) shows, in the case of a uniform distribution of dust, two peaks in the flux and also in the polarization fraction. The first one is defined by the surface of the scattering region, as more photons reach it we also begins to see a small cancellation effect by symmetry due to photons that reach both sides of the inner radius. This effect is repeated again with the photons that are able to get a bit deeper into the scattering region. The response is much less coherent for regions filled with clouds, due to their random distribution.

6.2.3 Towards a more realistic AGN model

We have already calculated the cross-correlation delays for the different isolated geometries and have seen how close they are to the inner radius of each region. At this point, the regions that were analyzed independently before were assembled together. In order to better evaluate the impact of each one of them in the final and more realistic model, the different regions were incorporated step by step, similarly to what was done in Marin et al. (2012).

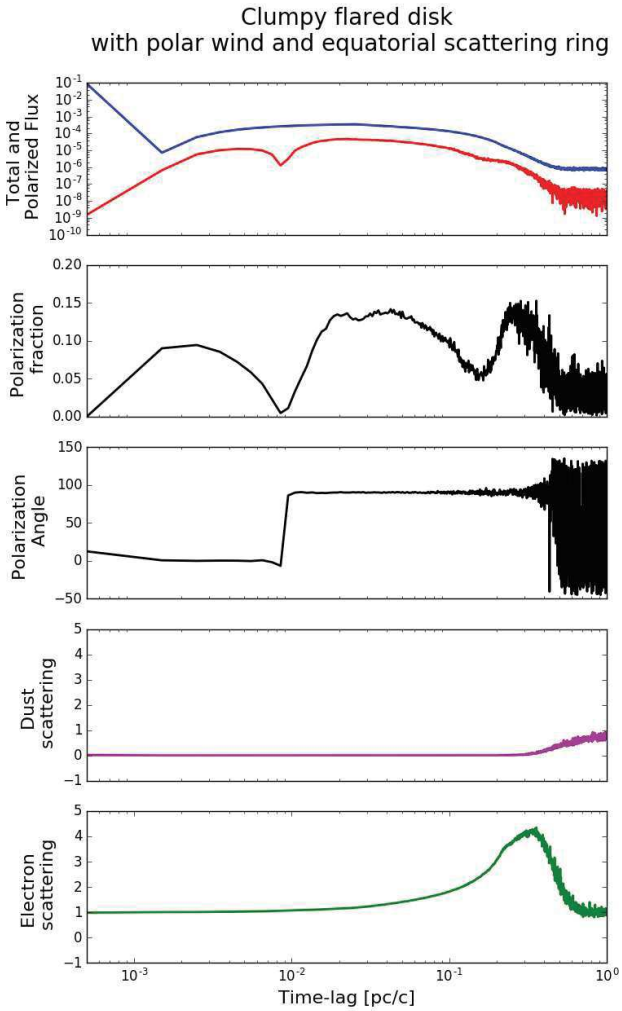

Figure 6.7: Transfer function obtained from *STOKES* for clumpy flared disk with polar winds and scattering ring. *Top to Bottom*: total (blue) and polarized (red) flux, polarization fraction (black), polarization angle (black), number of dust scattering (magenta) and number of electron scattering (green) as a function of time-lag.

Table 6.3 shows the result of the CCF for the uniform dusty-torus geometry, as the baseline model followed by the results obtained by adding one by one the different scattering regions. In the following we refer to the equatorial ring as BLR and as always as polar winds to the highly ionized cone in the polar region. The same results are shown in Tables 6.4, 6.5 and 6.6 for the uniform flared-disk model, clumpy dusty-torus model, and clumpy flared-disk model respectively.

The general trend is the same for all models. When we include the equatorial ring, the time delay decreases to a value close to the one obtained for the equatorial ring alone. As we saw before, the equatorial scattering region is a strong polarizer due to the 90° scattering angle.

Table 6.3: Cross Correlation between total flux and polarized flux.

UNIFORM DUSTY TORUS (UDT) (units: days)			
BAND	**V (5500Å)**	**B (4500Å)**	**UV (2500Å)**
UDT + BLR	19.1 ± 6.1	17.3 ± 6.4	16.1 ± 6.0
UDT + Polar-wind	80.4 ± 17.4	73.3 ± 22.5	53.9 ± 14.2
UDT + Polar wind + BLR	19.7 ± 7.7	14.3 ± 6.9	16.7 ± 22.5

Therefore, the equatorial disk has a strong impact on the polarized flux. If, on the other hand, we incorporate the polar winds to the baseline model, it leaves the results unchanged, as we observe the same response as for the baseline model alone. The polar cones are seen mostly in transmission and therefore polarize less.

Table 6.4: Cross Correlation between total flux and polarized flux.

UNIFORM FLARED DISK (UFD) (units: days)			
BAND	**V (5500Å)**	**B (4500Å)**	**UV (2500Å)**
UFD + BLR	22.0 ± 7.8	20.0 ± 7.1	18.5 ± 6.8
UFD + Polar-wind	71.8 ± 19.7	75.1 ± 22.0	54.8 ± 16.9
UFD + Polar wind + BLR	20.0 ± 8.1	20.3 ± 7.2	18.5 ± 5.5

Table 6.5: Cross Correlation between the total flux and polarized flux.

CLUMPY DUSTY TORUS (CDT) (units: days)			
BAND	**V (5500Å)**	**B (4500Å)**	**UV (2500Å)**
CDT + BLR	23.5 ± 7.1	3.0 ± 3.6	12.2 ± 6.7
CDT + Polar wind	534.3 ± 100.5	557.5 ± 97.0	610.5 ± 160.5
CDT + Polar wind + BLR	16.1 ± 5.4	14.4 ± 9.6	19.1 ± 4.5

Finally, when we incorporate all elements (the polar winds and the equatorial ring) to the baseline model, we come to the same conclusion for all baseline models: uniform dusty-torus, uniform flared-disk, clumpy dusty-torus and clumpy flared-disk. In all cases it is the equatorial ring that predominates and the time delay obtained from the CCF is almost the same as if this area were isolated with slight differences between the models considered. This is an important result. With this technique we get information on the closest region in the equatorial plane, independently of the rest of the other scattering regions, at least for type-1 viewing angles.

Although the results so far allow us to somehow characterize the geometry of the equatorial ring, until now the results obtained by correlation give us a value larger than the inner radius of this region. In order to reproduce the value found by Gaskell et al. (2012), we increased the density of the region. As we see in Table 6.7, with an optical depth of $\tau \sim 3$ we get a value in the expected range considering the

Table 6.6: Cross Correlation between the total flux and polarized flux.

CLUMPY FLARED DISK (CFD) (units: days)			
BAND	**V (5500Å)**	**B (4500Å)**	**UV (2500Å)**
CFD + BLR	17.0 ± 5.1	23.8 ± 3.6	22.0 ± 5.2
CFD + Polar wind	394.6 ± 416.9	388.4 ± 187.7	475.3 ± 74.2
CFD + Polar wind + BLR	20.3 ± 7.4	19.1 ± 5.5	22.0 ± 4.2

associated error, and even more precise is the CCF obtained for models that have a BLR with an optical depth of the order of $\tau \sim 10$, which corresponds to an electron density of the order of 10^8 cm^{-3}. This better agrees with the theoretical values for the BLR region: 10^9 cm^{-3} for an optically thick and 10^{14} cm^{-3} for optically thin regime (Popović, 2003).

Table 6.7: Cross Correlation for several electron density in the equatoral-ring.

CLUMPY DUSTY TORUS + POLAR WIND + EQUATORIAL RING (units: days)		
	V band	**B band**
BLR ($\tau \sim$1)	16.5 ± 5.4	14.4 ± 9.6
BLR ($\tau \sim$3)	13.7 ± 4.5	10.7 ± 4.2
BLR ($\tau \sim$10)	6.6 ± 1.5	6.0 ± 1.2

CLUMPY FLARED DISK + POLAR WIND + EQUATORIAL RING (units: days)		
	V band	**B band**
BLR ($\tau \sim$1)	20.3 ± 7.4	19.1 ± 5.5
BLR ($\tau \sim$3)	11.0 ± 2.3	10.7 ± 4.2
BLR ($\tau \sim$10)	4.8 ± 1.6	7.1 ± 1.2

6.3 Conclusions

In this chapter we have applied the technique of reverberation by cross-correlation between the total and polarized flux. We have analyzed the time-lag results for the various regions contributing to the polarized flux, separately and as a whole; we have also reviewed how the model responds when the region is full of dust or electrons. This has been done only for one viewing angle corresponding to a type-1 AGN.

The time delay obtained for the circumnuclear region set in the equatorial plane alone, uniformly filled with dust and with a thick optical depth, corresponds almost

exactly to the time it takes for a photon to reach the inner radius of this region.

The same result is obtained for the equatorial ring full of electrons, when the optical depth is high, while when it is close to or less than 1, the computed time delay is larger than the time it takes for a photon to reach the inner radius, because photons penetrate deep in the equatorial ring.

We also showed that the addition of a highly ionized polar cone with low optical depth does not impact significantly the calculated total time lag.

The most important result is that when we combine all scattering regions, the component that determines the time lag is the equatorial ring, thus validating this technique as a tool to find the distance from the emission region to the nearest scattering region. We also validated the results obtained by Gaskell et al. (2012).

Chapter 7

Conclusion and prospects

This thesis has addressed the question of how to learn about the structure of the innermost regions of AGNs. In the introductory chapter we saw that we cannot yet learn about their inner structure directly because of their small scale and their large distances from us, although new interferometry techniques today are starting to be able to observe at least the circumnuclear region of the nearest objects. As a result, sizes and spatial distributions of components in the inner regions are still far from clear. We have seen that the combination of reverberation mapping and polarimetry is a very useful tool for learning about the unresolved regions.

7.1 Overview of results

The temporal response of the various contributions to the polarization of different internal components of AGNs, such as the circumnuclear region, the ionizing polar region, and the BLR represented by a ring in the equatorial region, have been studied.

Starting from the circumnuclear region, we calculated the time delay of polarized light for two different dust geometries. We did not find a significant difference due to the dust composition, at least for the two prescriptions studied. The time delays introduced by ionized regions, both in the poles (the so-called polar wind), and in the equatorial plane of the AGN (our equatorial ring, which represents the BLR) were studied. From investigations of the time lag of the polarized emission as a function of viewing angle, it has been shown that, due to multiple scattering effects the polarized signal in type-2 objects lags further behind the total intensity than for type-1 sources. We have also found that for models with the dust distributed in the form of clouds, it significantly increased the time lag. When adding polar winds to the model, scattered radiation further increases the polarization time lag. The presence of a scattering equatorial electron disk naturally reduces the observed time lags for type-1 viewing angles since a fraction of the photon flux is reprocessed by electrons and escapes along the polar directions. By combining simple geometries, we succeeded in developing a more sophisticated model of the different regions of the innermost parts of an AGN, using as a pattern the archetypical type-1 AGN, NGC 4151.

It is worth pointing out that in Chapter 5, we called "time lag" or "time delay" the difference between the time it takes on average for the photons to reach the observer directly from the source and the time it takes for photons to reach the observer after scattering. Unfortunately it is not an observable. On the other hand, in Chapter 6 onwards we called to time lag or time delay the difference obtained from the cross correlation between the light curves of direct flux and polarized flux. In this case this value is equivalent to that obtained from observations.

From the transfer functions obtained with *STOKES*, we generate the corresponding polarization light curves for given total flux light curves. These can be compared with observations. We calculate the temporal difference between the total flux (source + polarized) with the polarized flux by cross correlating the two time series. This gives a weighted-mean difference in the distances travelled by the photons. We found that for type-1 viewing angles, the time delay of the polarized flux is set by the ionized region in the equatorial ring, the BLR. This is a strong polarizer due to its perpendicular scattering angle. On the other hand, the polar cones are seen mostly in transmission (i.e. forward scattering) and therefore polarize less. This allows us, through the technique of polarization reverberation mapping, to determine the size of the inner radius of the scattering region associated with the BLR. The most important thing is the possibility of determining the dimensions and characteristics of this scattering region from observational campaigns of only a few months for typical sizes of the regions studied.

We can conclude that the new technique of polarization reverberation mapping is an important step forward in our objective of understanding the internal regions of AGNs. It may also be used on other unresolved astrophysical objects. Treating polarization as a function of time also offers another independent way to constrain AGN model parameters. For this, it is important to combine the polarization time lag, polarization degree and position angle and compare these observables to the type of simulation results that are presented here.

7.2 Prospects

We have demonstrated that polarimetric reverberation mapping is a valid technique to gain information about the inner region of an AGN on the scale of the BLR, this being the region of scattering closest to the center of emission. This technique is able to identify internal or unresolved regions of other astrophysical objects, for example it would be interesting to exploit this technique to study the evolution of supernovae.

For the study of the internal region of the AGNs it is necessary to have appropriate observational data. The next step in this line of research is to make a list of existing data and then to organize new observational campaigns. These have the advantage that only a few months of observation are required instead of years.

With the appropriate data and careful systematic observations in short periods of time, it should be possible to apply the models presented here to find the appropriate parameters that fit the observations, and thus to obtain information on the size, distribution and density of the scattering region associated with the BLR.

Another area for future work is to add more sophistication to the models, for example generating the BLR regions of clouds with density stratification, such as those presented in Marin et al. (2018) for dust equatorial structures and incorporating the study of broad lines. We can also add the NLR and study the impact of a region of non-dense dust on the poles to bring the models even closer to the real AGNs.

Considering that in this case the scattering source is an ionized region, the time delay is independent of wavelength. For this reason, from the point of view of the physics of the AGN, it does not matter at what optical wavelength the observations are made. Therefore, in order to choose the best wavelength, we must apply criteria such as observational capacity, better signal-to-noise ratio and less contamination of the environment. For example, we can avoid infrared to avoid dust emission that will contaminate the signal.

Reverberation studies between the continuum and the lines have proven to be of great importance, because they allow to calculate the mass of the black hole. They give similar values for the radius of the BLR as those obtained in this study. Bentz et al. (2006) found a lag of 6.6 lt-days between the continuum and the broad Hβ line during an observation campaign in 2005 for NGC 4151. Different values, ranging from 3.3 to 6.6 lt-days (Gaskell et al., 2012, and therein) have been obtained using different lines (HeII, CIV. Hβ, Hγ). The smallest values correspond to the highest ionization potential. Xue and Cheng (1998) found a difference in size of the BLR comparing observational campaigns of 1993 and 1988, which can perhaps be interpreted in terms of dynamics of this region.

In summary, the study of time-dependent polarization adds a new and effective tool on our way to understanding the innermost regions of AGNs. The pioneers in using this technique were Gaskell et al. (2012) who made the first polarimetric reverberation mapping using data from a long series of observations of NGC 4151. Afanasiev et al. (2015) applied the technique to the radio-loud AGN 3C 390.3 and found a significantly smaller time lag for the polarized component with respect to the total continuum than for the Balmer lines. This suggests that the polarizing mirror would be smaller than the BLR. These studies are just beginning, we hope that many more studies will be carried out in the future and that we will be able to greatly increase our understanding of the internal regions of the AGNs.

Appendix A

Publications

A&A 611, A39 (2018)
DOI: 10.1051/0004-6361/201731331

Astronomy & Astrophysics

Modeling optical and UV polarization of AGNs

IV. Polarization timing

P. A. Rojas Lobos[1], R. W. Goosmann[1], F. Marin[1], and D. Savić[1,2]

[1] Observatoire Astronomique de Strasbourg, Université de Strasbourg, 11 rue de l´Université, 67000 Strasbourg, France
e-mail: parltest@gmail.com
[2] Astronomical Observatory of Belgrade, Volgina 7, 11060 Belgrade, Serbia

Received 7 June 2017 / Accepted 21 November 2017

ABSTRACT

Context. Optical observations cannot resolve the structure of active galactic nuclei (AGN), and a unified model for AGN was inferred mostly from indirect methods, such as spectroscopy and variability studies. Optical reverberation mapping allowed us to constrain the spatial dimension of the broad emission line region and thereby to measure the mass of supermassive black holes. Recently, reverberation was also applied to the polarized signal emerging from different AGN components. In principle, this should allow us to measure the spatial dimensions of the sub-parsec reprocessing media.
Aims. We conduct numerical modeling of polarization reverberation and provide theoretical predictions for the polarization time lag induced by different AGN components. The model parameters are adjusted to the observational appearance of the Seyfert 1 galaxy NGC 4151.
Methods. We modeled scattering-induced polarization and tested different geometries for the circumnuclear dust component. Our tests included the effects of clumpiness and different dust prescriptions. To further extend the model, we also explored the effects of additional ionized winds stretched along the polar direction, and of an equatorial scattering ring that is responsible for the polarization angle observed in pole-on AGN. The simulations were run using a time-dependent version of the STOKES code.
Results. Our modeling confirms the previously found polarization characteristics as a function of the observer's viewing angle. When the dust adopts a flared-disk geometry, the lags reveal a clear difference between type 1 and type 2 AGN. This distinction is less clear for a torus geometry where the time lag is more sensitive to the geometry and optical depth of the inner surface layers of the funnel. The presence of a scattering equatorial ring and ionized outflows increased the recorded polarization time lags, and the polar outflows smooths out dependence on viewing angle, especially for the higher optical depth of the wind ($\tau = 0.3$).
Conclusions. Together with other AGN observables, the polarization time lag places new, independent "seismological" constraints on the inner geometry of AGN. If we conduct time-dependent spectropolarimetric observing campaigns of AGN, this method has a high potential for a census of supermassive black holes.

Key words. galaxies: active – Galaxy: nucleus – polarization – scattering

1. Introduction

Active galactic nuclei (AGN) are very compact and high-luminosity engines located at the center of their host galaxies. Since the innermost structures of AGN cannot be resolved by current UV, optical, or IR observational techniques, morphological and kinematic models have to be derived indirectly, most often from broadband spectroscopy and variability studies.

In so-called thermal radio-quiet AGN, the emission is due to accretion onto a supermassive black hole (SMBH),with typical masses $M_{\rm SMBH} > 10^6\ M_\odot$ (Salpeter 1964; Lynden-Bell 1969). The accretion disk produces the optical and UV continuum radiation (see Shields 1978; Shakura & Sunyaev 1973; Pringle et al. 1973). The disk axis points out a preferred direction that for the remainder of this paper we call the polar direction of the system, to be distinguished from the equatorial directions that enclose the plane of the accretion disk. Observationally, thermal AGN can then be divided into two classes: type 1 sources are assumed to be viewed at a polar line of sight and show Doppler-broadened Balmer emission lines produced in the so-called broad line region (BLR), whereas type 2 sources are viewed at equatorial lines of sight, at which the optical view of the BLR is obscured by a dusty region commonly called the dusty torus (Antonucci 1993). It extends out to a spatial scale of a few parsecs for a $10^7\ M_\odot$ SMBH. Only in very few objects do the outer parts of the circumnuclear dust start to be resolvable by mid-IR interferometry techniques (Tristram et al. 2007, 2014; Raban et al. 2009).

Gaskell (2009) introduced the so-called bird's nest paradigm for the central region of thermal AGN, adopting the idea that its overall structure is clumpy. Clumpy models successfully reproduce the dust emission seen in the IR (Nenkova et al. 2008; Siebenmorgen et al. 2015; Hönig & Kishimoto 2010). The BLR is expected to be fragmented and turbulent, but radially stratified, as can be inferred from the velocity structure of low- and high-ionization emission lines (Gaskell 1982; Gaskell et al. 2008; Gaskell & Goosmann 2013). The BLR is expected to form inside the sublimation radius, possibly from inflowing torus material. It is therefore embedded in the torus funnel. Since the outer parts of the accretion disk around the SMBH must be self-gravitating, it is straightforward to identify it with the inner parts of the BLR. A coherent picture for the circumnuclear matter of AGN can be found with a morphology that is non-spherical, but symmetric with respect to the polar axis, while being fragmented on small spatial scales.

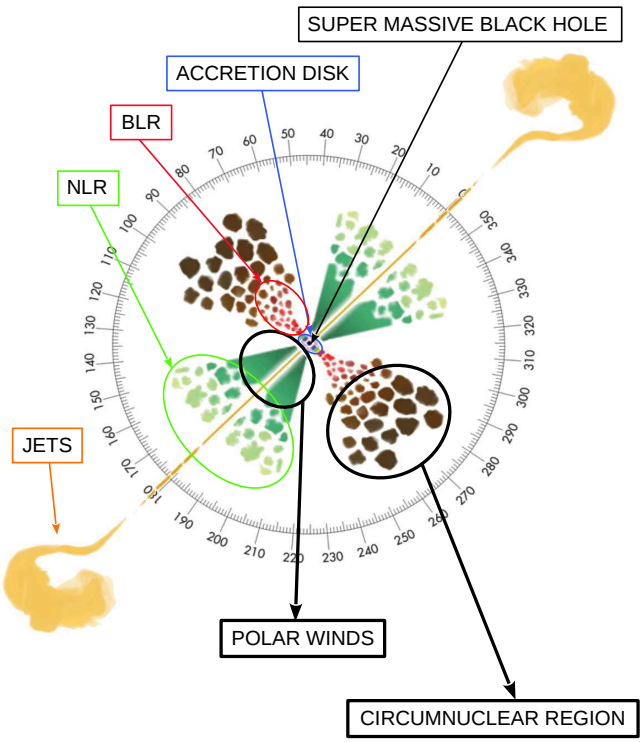

Fig. 1. Unscaled sketch of the unified model of AGN, taken from Marin (2016). The cartoon shows that AGN with narrow and broad Balmer emission lines (type 1, $i = 0{-}60°$) and those with only narrow lines (type 2, $i = 60{-}90°$) derive from the same morphology, but are viewed from different angles with respect to the AGN axis. This is the original basis of the unified model.

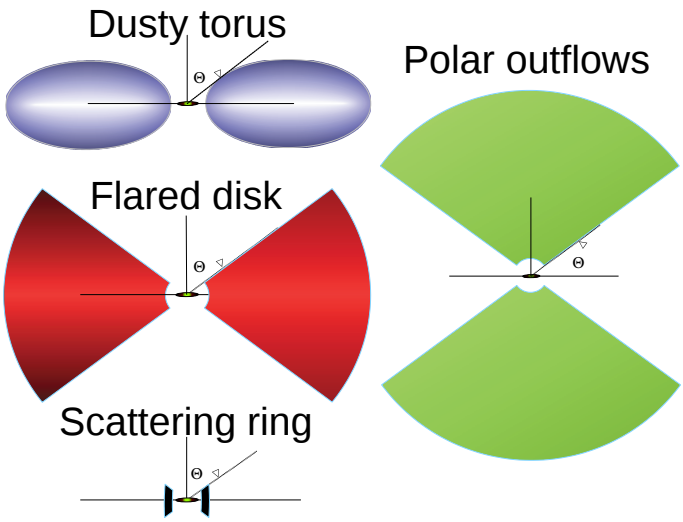

Fig. 2. Geometry scheme of the models. *Left top*: classical torus geometry (blue) with elliptical cross section. *Left middle*: the extended flared-disk geometry (red) with the wedge-shaped cross section. *Left bottom*: scattering ring (brown). *Right*: polar outflows (green).

Not all matter that is pulled in by the black hole is finally accreted. Depending on the accretion state of a given thermal radio-quiet AGN, a significant fraction of matter may be ejected along the polar directions as moderate to ultrafast winds (Pounds & Page 2006; King & Pounds 2003; Tombesi et al. 2012). Depending on the distance from the SMBH, these winds are mildly to strongly ionized and scatter much radiation that is emitted by the central black hole. The common picture of the inner structure of AGN was recently described by Marin (2016), and the reproduction in Fig. 1 depicts the regions inside the AGN (not to scale): the black hole sits at the center and is surrounded by the accretion disk, the BLR, and the circumnuclear dust. Along the polar directions, ionized winds and the narrow line region (NLR) are located, which in radio-loud objects may be pierced by collimated jets.

Polarimetry is a valuable tool to probe the innermost structures of AGN. In the past, optical spectropolarimetry gave proof of the unified theory of AGN when Antonucci & Miller (1985) discovered polarized broad Balmer lines in Seyfert 2 galaxies and thus pointed out a relation between the observer's inclination with respect to the polar axis and the position angle of optical continuum polarization in type 1 and type 2 AGN. It was shown in that the typical polarization properties in type 1 objects can be produced by scattering in a flattened distribution of material situated around the accretion disk (Antonucci 1984; Smith et al. 2004; Goosmann & Gaskell 2007).

More recently, AGN polarimetry has been brought to a different level by introducing the technique of polarization reverberation mapping (Gaskell et al. 2012 for the Seyfert 1 nucleus NGC 4151). In this method, the time-dependent total (polarized+unpolarized) continuum emission is cross-correlated with the polarized emission of a given AGN. A characteristic time delay is found between the two components. When we assume that the continuum polarization is induced by scattering of the continuum radiation by surrounding structures, the reverberation places constraints on the light travel distance between the emitting source and the reprocessing mirror(s).

In this work, we present initial modeling to compare with current and future campaigns of polarization reverberation mapping. We conduct radiative transfer simulations for the continuum radiation in different AGN geometries, taking the time dependence of the polarized radiation in the optical band into account. The goal of this research is to numerically explore the new method and indirectly resolve the innermost region in AGN by polarization reverberation. To do this, we provide simulated results for polarization time lags from different AGN constituents as a function of inclination. The paper is organized as follows: in Sect. 2 we present the details of our model and specific parametrization. In Sect. 3 we present and analyze our results. Finally, in Sect. 4 we discuss our results and follow-up projects.

2. Modeling the circumnuclear dust scattering

Following the observational example of Gaskell et al. (2012), we here attempt to theoretically investigate the details of the inner AGN structure by studying the expected time lag between the total and the polarized continuum flux. The presence of the obscuring torus on the line of sight should be derived from the time lag, together with its geometrical shape and composition. Figure 2 shows a sketch of our different modeling options. In the following, we call "dusty-torus" a toroidal region with an elliptical cross section, and "flared-disk" a region with a wedge-shaped cross section. We investigate polarization timing for four versions of a circumnuclear geometry: a uniform-density dusty torus, a uniform-density flared disk, a clumpy torus, and a clumpy flared disk. Every geometry is tested for two types of optically thick dust: AGN-dust (Gaskell et al. 2004) and Milky Way dust (so-called MRN dust, according to Mathis et al. 1977) at different optical depths. We increase the complexity of the model by adding ionized outflows in the polar direction in

Table 1. Model setup, baseline.

Models	Torus	Flared disk	Scattering ring	Polar wind
DUSTY				
Inner radius (pc)	0.061	0.061	0.0067	0.0067
Outer radius (pc)	15.061	15.061	0.0577	30.0067
Half opening angle	60°	60°	60°	30°
Equatorial optical depth	150	150	1	0.03 / 0.3
Scattering	Mie	Mie	Thomson	Thomson
CLUMPY				
Inner radius (pc)	0.061	0.061		
Outer radius (pc)	15.061	15.061		
Half opening angle	60°	60°		
Optical depth per cloud	50	50		
Clouds radius (pc)	0.2	0.65		
Filling factor	25%	25%		
Scattering	Mie	Mie		

Notes. Parameters of three scattering regions with uniform and clumpy dust distribution for the Mie scattering and free electron distribution for Thomson scattering.

Sect. 3.2 and a scattering ring, responsible for the specific polarization position angle seen in type 1 AGN (Smith et al. 2004), in Sect. 3.3. The latter region is fully ionized and is located between the source and the circumnuclear dust region. As the model setup becomes more sophisticated, we follow the evolution of the polarization time lags.

We applied an extended version of the Monte Carlo radiative transfer code STOKES. This version includes the timing information of the registered photons. The code was initially written by Goosmann & Gaskell (2007) and further developed by Marin et al. (2012) and Marin et al. (2015); an intermediate version of the code is publicly available[1]. It simulates radiative transfer in different geometries for emitting and scattering structures and determines the net Stokes parameters as a function of wavelength, time, and the observer's line of sight. Subsequently, it is possible to obtain the polarization fraction, position angle, polarized flux, and total flux from the Stokes parameters. For compatibility with Paper I (Goosmann & Gaskell 2007), we define the polarization position angle to be 0° when the polarization angle is perpendicular to the projected symmetry axis of the model. When the polarization angle is equal to 90°, it is said to be parallel to the projected symmetry axis of the model. To compute the time lags, the code compares the path between the direct flux from the source and the trajectory of the photons that have been scattered from the dust and/or electron regions. For each viewing direction, the time lag is measured relative to the plane of sky, which goes through the origin of the central source and is oriented perpendicularly to the line of sight. The lag is expressed in pc/c and represents the light traveling distance.

We modeled the flared-disk and toroidal geometries shown in Fig. 2 assuming uniform-density and clumpy dust distributions. Two types of dust were tested: AGN-dust composed of 85% of silicate and 15% of graphite, and Milky Way dust composed of 62.5% of silicate and 37.5% of graphite. The grain radii lay between 0.005μ (0.005μ) and 0.25μ (0.2μ), with a distribution $n(a) \propto a^s$ with $s = -3.5$ ($s = -2.05$) for Milky Way (AGN) dust. The filling factor of the clumpy regions was set to 25% (Marin et al. 2015). At the center we defined a point source with unpolarized flux that emitted a power law spectrum $F_\nu \propto \nu^{-\alpha}$ with $\alpha = 1$. For the ionized regions we assumed an inner radius of 8 light days such as found by Gaskell et al. (2012) in the case of NGC 4151, but without detailed modeling. In the case of the circumnuclear dusty regions, we adopted the observational constraints derived by near-IR observation of NGC 4151, namely 0.061 pc, according to Kishimoto et al. (2013).

The outer radius of the torus and its half opening angle were based on the findings by Ruiz et al. (2003), Table 2, who conducted near-IR polarimetry observations of the same object. We defined an external radius of 15.061 pc and a half opening angle of 60° from the disk symmetry axis. The dust is opaque, with a radial optical depth of ~150 inside the equatorial plane. The modeling results can be evaluated over the optical wavelength range and as a function of the observer's viewing angle.

In a second step of this study, we added polar winds to this baseline model. They have the geometrical shape of double-cones and are assumed to be ionized. In the model they are filled with electrons with a radial Thomson optical depth of 0.03 and 0.3. The winds have a common interface with the circumnuclear dust at the inclination of its horizon. Finally, we added a third region, an equatorial scattering ring located between the source and the circumnuclear dusty region. This area, modeled as a flared disk, was found to be necessary to reproduce the parallel polarization position angle observed in the majority of Seyfert 1s, see Smith et al. (2004). Following the composition constraints from Paper II, we opted for a radial optical depth of unity. The inner radius of the scattering ring was set to 0.0067 pc (i.e., eight lights days, Gaskell et al. 2012) and the outer radius to 0.0577 pc, so that the disk and the torus did not mix (see Table 1 for a summary of the parameters).

3. Results and analysis

All modeling cases were tested for the two different dust prescriptions: Milky Way dust (Mathis et al. 1977), and AGN-dust (Gaskell et al. 2004). A detailed comparison of the effect of the dust prescription on the polarization results was given in Goosmann & Gaskell (2007). The new simulated observable added in this work, the time lag of the polarized emission, is not much affected when the dust prescription is modified (Fig. 3). The small differences between the two cases are due to the specific albedo and scattering phase functions of the two dust types. Since there is no major effect on the results, we only present modeling for the case of standard Milky Way dust in this paper.

The response in terms of flux, polarization, and time lag only mildly changes with wavelength (Fig. 4). Only at type 2 viewing angles does the uniform dusty torus show a diminution in flux

[1] http://stokes-program.info/

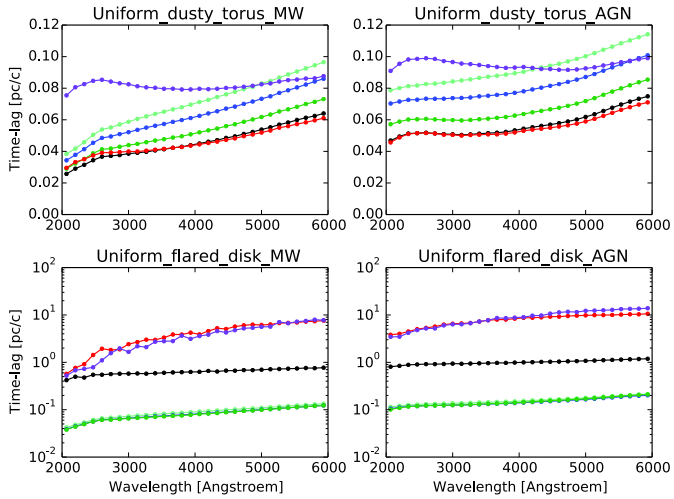

Fig. 3. Comparison of the time lags induced by the Milky Way and by AGN dust prescription for the case of a uniform dusty torus and a uniform flared disk. The plots show the time lag as a function of wavelength for different viewing angles: the magenta dots denote $\theta = 79.9°$, and the red dots $\theta = 71.0°$, which represents a type 2 view. The black dots show $\theta = 61.64°$, a view close to the torus horizon. Type 1 views are shown in green ($\theta = 51.3°$), blue ($\theta = 39.19°$), and cyan ($\theta = 28.9°$).

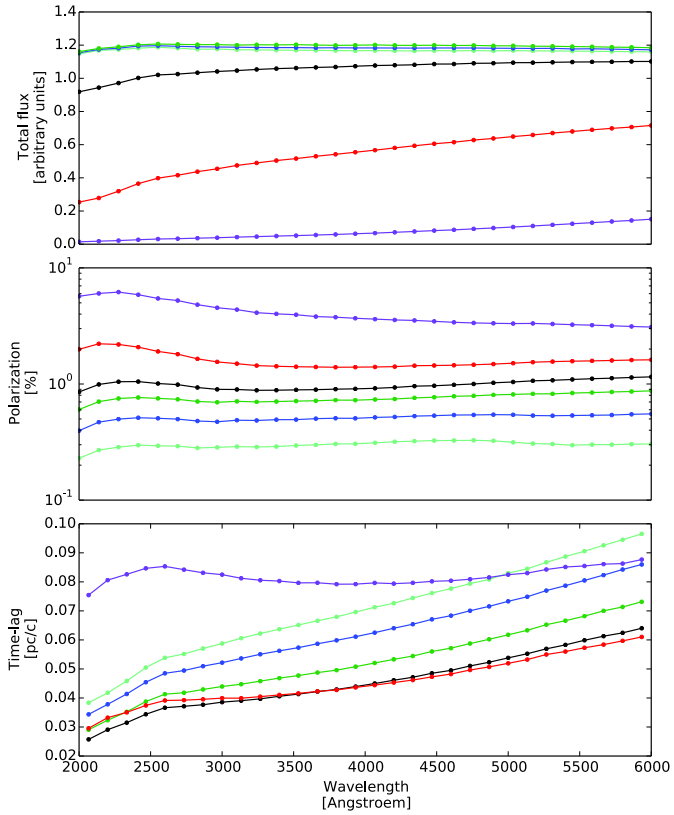

Fig. 4. Results of STOKES time-dependence version for the uniform dusty torus geometry. *Top*: total flux, polarization percentage, and time lag as a function of wavelength and for different viewing angles: the magenta dots denote $\theta = 79.9°$, and the red dots $\theta = 71.0°$, which represents a type 2 view. The black dots show $\theta = 61.64°$, a view close to the torus horizon. Type 1 views are shown in green ($\theta = 51.3°$), blue ($\theta = 39.19°$), and cyan($\theta = 28.9°$). *Middle*: percentage of polarization. *Bottom*: time lag.

and an increase in polarization around the 2175 Å absorption feature. Overall, the results shown in Fig. 4 confirm our previous work: for a type 1 inclination, we obtain a higher flux level

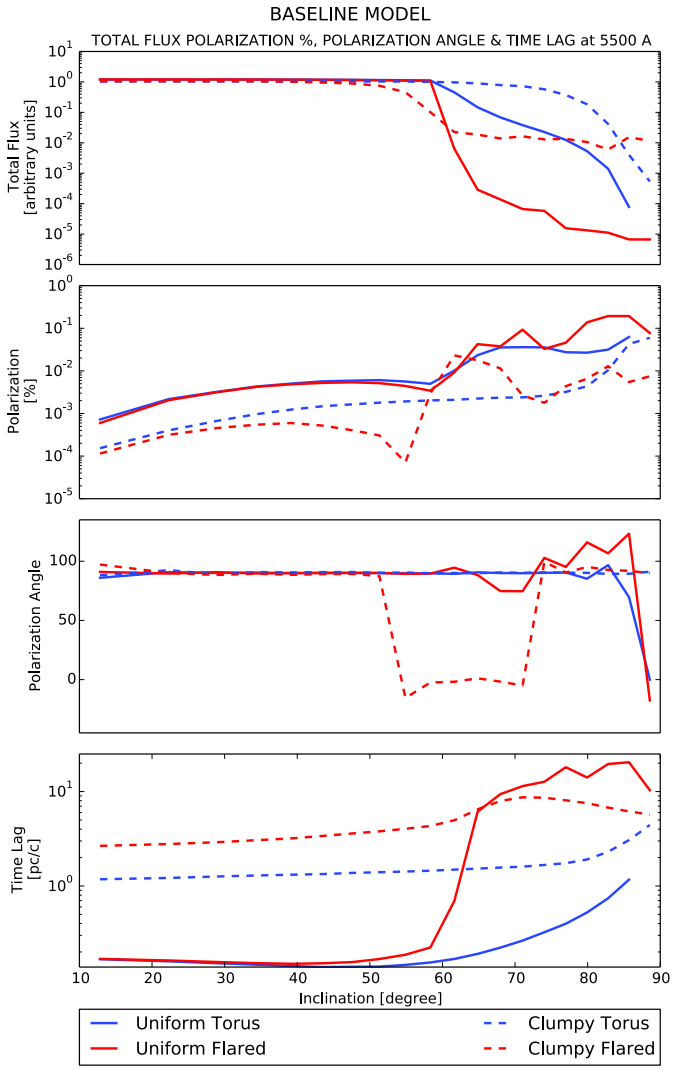

Fig. 5. Stokes results for V-band normalized flux, percentage of polarization, polarization angle, and time lag for different viewing angles. The blue line represents the uniform dusty torus model, and the blue dashed line the clumpy dusty torus, the red line the uniform flared disk, and the red dashed line represents the clumpy flared disk.

and lower polarization than at type 2 viewing angles. The new simulated observable in this work is the average time lag of the radiation. We note that this time lag is taken relative to the direct emission coming from the central source. The units are set to pc/c, which allows us to interpret the time lag in a straightforward manner in terms of light traveling distances. This time lag is always higher at type 2 viewing directions than for type 1, which is expected because below the torus horizon, we only detect (multiply) scattered radiation that has taken a non-direct path from the central source to the observer.

Except for these features, the results in terms of spectral flux, polarization, and time lag do not vary much with wavelength. For the remainder of this paper we therefore show our results for the V band centered on 5500 Å and as a function of viewing angle. All models show significant differences between face-on and edge-on views.

3.1. Baseline model for circumnuclear dust

Our baseline model contains the axisymmetric dust region with a half opening angle of 60° as measured from the axis (see Fig. 2). The modeling results are plotted in Fig. 5. At face-on

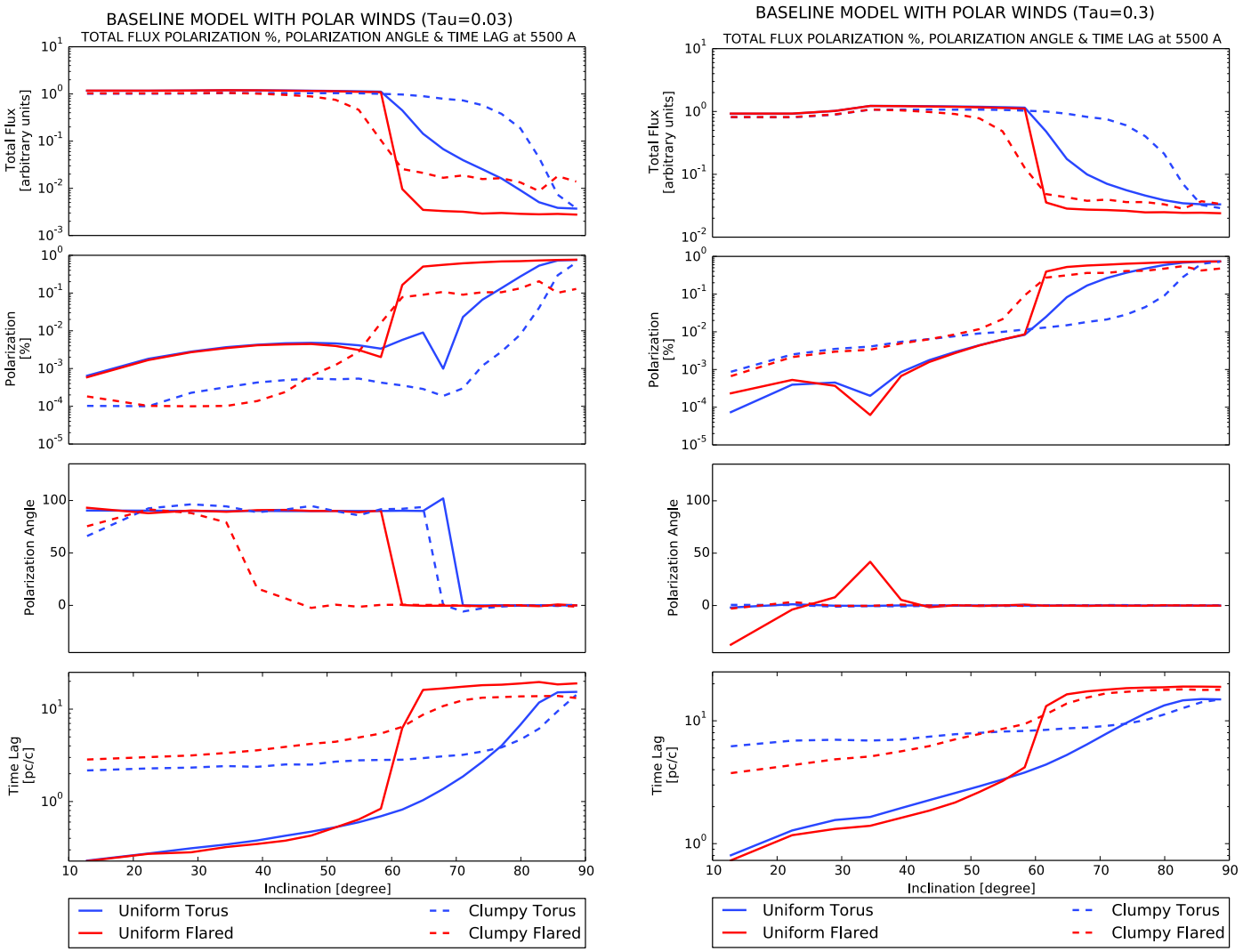

Fig. 6. Integrated and normalized flux, percentage of polarization, polarization angle, and time lag for different viewing angles for baseline model, with an ionized polar wind of 60° half opening angle Thomson optical depth of $\tau = 0.03$ (*left*) and $\tau = 0.3$ (*right*).

inclinations, all four models show roughly the same spectral shape in total flux, polarization degree, and time lag. The normalization of the spectral flux is almost the same for all four morphological setups because at these viewing angles the radiation predominantly comes from the central source. Still, a face-on observer finds a higher time lag and lower polarization degree for the clumpy dust distribution than for the uniform density cases. This is due to radiation scattered into the type 1 lines of sight. In a clumpy circumnuclear environment, the escaping photons experience on average a higher number of scatterings before they end up on a type 1 line of sight (see Marin et al. 2015). For optically thick uniform-density regions, the scattered radiation at face-on viewing angles is mostly dominated by the first-scattering component that is more strongly polarized and accumulates less of a time lag.

At edge-on inclination, the observer's line of sight is obscured by dust, and the flux strongly decreases. The polarization degree slowly increases with increasing viewing angle for all four geometries. At all type 2 viewing angles, the time lag accumulated for a clumpy or uniform torus geometry is much shorter than for the case of a flared dust distribution.

This difference is related to the shape of the inner surfaces. For a torus, the inner surface is convex, while for the flared disk it is parametrized as a concave shape. As discussed in Goosmann & Gaskell (2007), when comparing the obscuration efficiency between compact and extended dusty tori, we find again here that a more convex shape of the inner surfaces makes it more likely for a photon to escape after only a few scattering events. Therefore, the accumulated time lag for the case of a toroidal dust distribution remains short even when the distribution is clumpy.

For the case of our flared geometry, the inner surface is parametrized as a sphere segment against which the photons are injected from the inside. In general, multiple backscattering inside this sphere segment is necessary for the photons to finally escape, and if they do, the escape cone is strictly limited by the half opening angle of the flared disk as measured from its symmetry axis. Figure 5 shows that the rise in time lag and polarization degree is steep around this inclination for the flared dusty disk, while for the toroidal geometry, the rise is much more shallow. For clumpy dust distributions, the horizon of the torus and of the flared disk is more blurry, which decreases the slope of the polarization degree and the time lag even further. The polarization position angle remains at 90° (i.e., parallel to the projected symmetry axis, following the usual convention in this paper series) over all viewing angles for models without polar winds,

with the exception of a clumpy flared geometry, for which the polarization position angle stays at 90° at face-on viewing angles, then shifts to 0° (perpendicular polarization) around the transition between type 1 and type 2 to return to parallel polarization at more extreme type 2 viewing angles. We argue that this behavior is related to the actual size of the clumps and to their distribution along the line of sight.

3.2. Adding polar outflows to the baseline model

Next, we added ionized winds stretched along the symmetry axis to our model. As in previous work of this series, the wind geometry was realized by a double-cone filled with electrons of a radial optical depth of 0.03 or 0.3 (see Fig. 6). When adding a low-density wind, the type 1 cases exhibit almost the same spectral flux level and polarization degree as for the baseline models. The additional scattering in the polar direction has a more significant effect on the time lag recorded at face-on viewing angles. It increases by a factor of roughly 2 when compared to the case without polar winds. When we add low-density polar winds, the polarization angle changes from 90° (parallel) at face-on view to 0° (perpendicular) in face-on for uniform models, while for a clumpy distribution, the polarization anlge remains at 0° for both geometries at all viewing angles.

The situation is slightly more spectacular for the edge-on case. The presence of even a low-density wind scatters a significant part of the radiation "around" the circumnuclear dust and thereby diminishes the strong absorption efficiency of the flared dusty disk.

When the winds are added, we find longer time lags with a more shallow dependence on viewing angle than for the baseline model. This is related to the fact that before escaping, the photons cross a second scattering region that adds more scattering events and increases the light travel path. The polarization position angle remains at 0° over all viewing angles for models with higher-density polar winds. This behavior, linked to the optical depth of the polar outflows, is in agreement with the polarization state observed for six Seyfert 1 AGN by Batcheldor et al. (2011). Since Smith et al. (2002), it has been a well known fact that a small fraction of type 1s shows optical polarization spectra similar to those of Seyfert 2 galaxies in which polarized broad lines are detected. In the compendium of AGN presented in Marin (2014), it was shown that these peculiar objects are associated with polarizations of a few percent and represent a rather small subclass of Seyfert 1s.

Similarly to our previous conclusion on the dependence of optical depth versus inclination, we note that a clumpy dust distribution is not very sensitive to inclination angles. Across type-1 and moderate type 2 viewing angles, the time lag distribution remains rather flat for both geometrical clumpy configurations; the time lag only increases for extreme type 2 lines of sight. This ambiguity is stronger for the wind with higher optical depth. In contrast to this, the time lag remains a discriminator between type 1 and type 2 inclination for the flared-disk geometry and is far higher with a uniform dust distribution.

3.3. Adding a scattering ring to the baseline model

We now include a third scattering region, an equatorial, ionized disk located between the source and the circumnuclear region. Compared to a model without equatorial electron disk (Fig. 5), our new modeling shows that only the polarization properties of light and its time lags are affected (see Fig. 7).

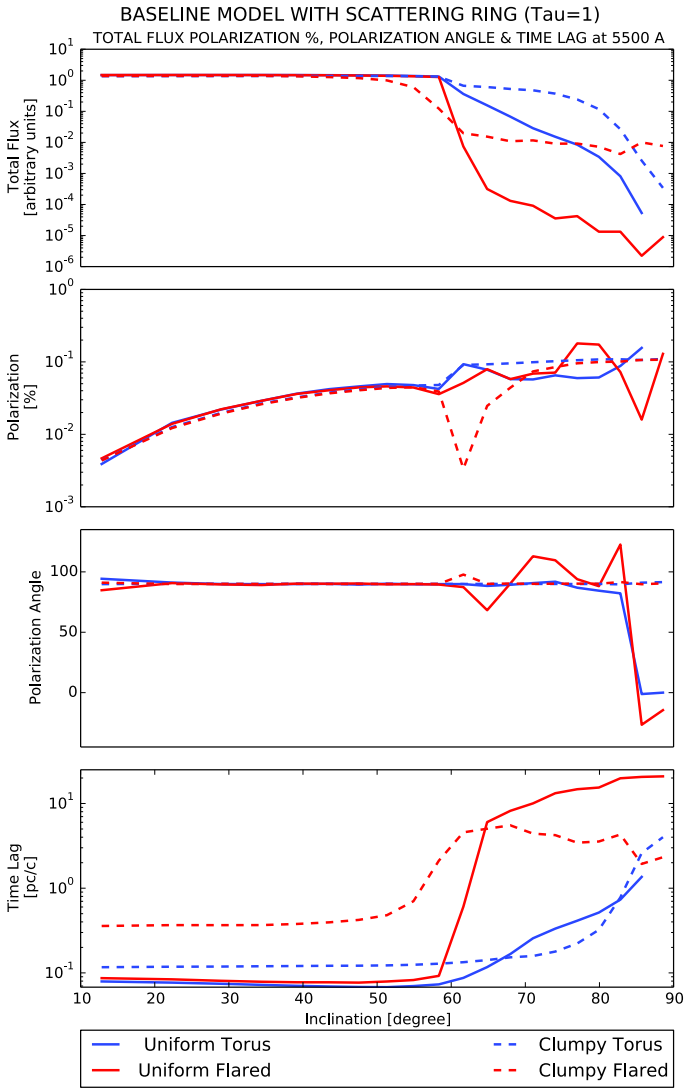

Fig. 7. Baseline model with equatorial ring. Stokes results for V-band normalized flux, percentage of polarization, polarization angle, and time lag for different viewing angles. The blue line represents the uniform dusty torus model, the blue dashed line the clumpy dusty torus, the red line the uniform flared disk, and the red dashed line represents the clumpy flared disk.

An additional scattering component that does not absorb radiation has almost no effect on the flux level observed at various inclinations. However, the electron disk stabilizes the degree of polarization observed in type 1 viewing angles, independently of the circumnuclear dust structure. The disk also sets the polarization of radiation to 90° at type 1 orientations, as has been observed (Smith et al. 2004). More importantly, the proximity of this region to the central source means that the observed time lags are shorter for type 1 inclinations. A fraction of the input radiation, depending on the solid angle covered by the opening angle of the electron ring, is directly scattered toward the observer, inducing a shorter time lag. For higher inclinations, radiation passes through the optically thin medium and scatters inside the optically thick dust structure, so that the effect of the equatorial ring becomes almost undetectable.

When we include polar outflows in addition to this scattering ring, see Fig. 8, we reach similar conclusions. The addition of an equatorial electron ring remains marginal in terms of total fluxes, but strongly helps the polarization degree and angle to

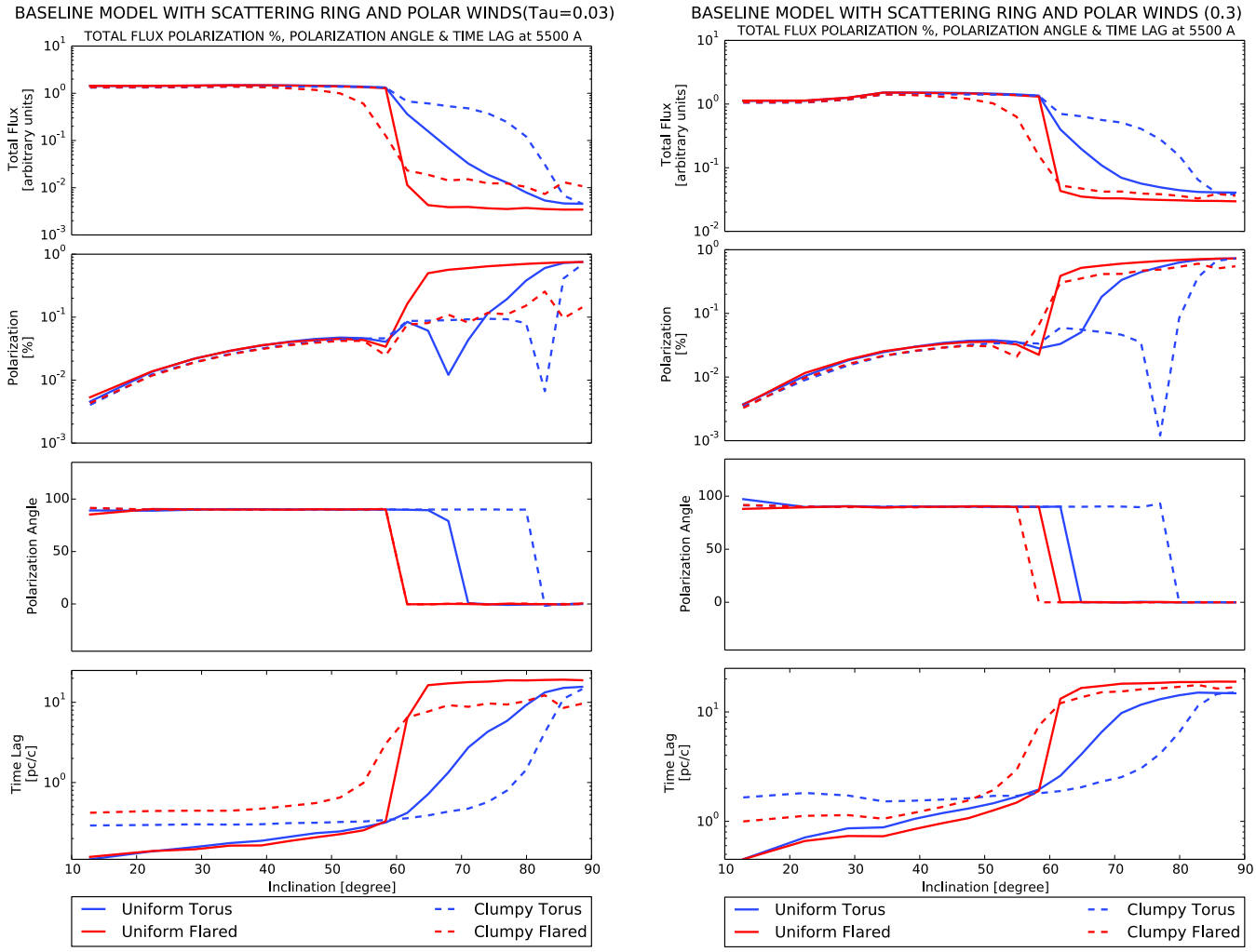

Fig. 8. Integrated and normalized flux, percentage of polarization, polarization angle, and time lag for different viewing angles for the baseline model with a scattering ring, with an ionized polar wind of 60° half opening angle, a Thomson optical depth of $\tau = 0.03$ (*left*), and $\tau = 0.3$ (*right*).

stabilize at typical values seen for local AGN (see Marin 2014). The degree of polarization remains lower than 1% for type 1 inclinations and sharply rises for type 2 orientations. The polarization angle rotates from parallel to perpendicular as soon as the observer's line of sight is obscured by the circumnuclear dusty region. The effect of the disk on the time lags at type 1 views is even stronger: the time lags are 5−10 times shorter, reflecting the presence of the ring. The effect of different wind optical depths on time lags is the same as what we described in Sect. 3.2.

4. Summary and conclusion

In this initial study, we extended polarization modeling of AGN into the timing domain. Investigating the time lag of the polarized emission as a function of viewing angle, we showed that owing to multiple scattering effects, the polarized signal in type 2 objects lags farther behind the total intensity than for type-1 sources. Furthermore, the geometrical shape of the dust distribution such as the shape of the inner surfaces and also their optical depth has an effect on the resulting time delay at type 2 lines of sight, and much less for type 1. A significant increase in time delay is recorded when the dust distribution is clumpy.

When adding polar winds to the model, scattered radiation further increases the polarization time lag. The presence of a scattering equatorial electron disk naturally reduces the observed time lags at type 1 inclinations since a fraction of the photon flux is reprocessed onto the electrons and escapes along the polar directions.

The overall picture thus remains complex and certainly still includes degeneracy. From the modeling we present here, it is not yet straightforward, for instance, to disthinguish between the density structure of polar outflows and the level of clumpiness in the torus. Nonetheless, treating polarization as a function of time offers another independent way to constrain the model parameters. For this, it is important to combine the polarization time lag, polarization degree, and position angle and compare these observables to the type of simulation results that we present here.

This study is inspired by the discovery of polarization reverberation mapping in NGC 4151 (Gaskell et al. 2012). In this paper we also refer to the initial modeling of polarization time lags with STOKES. The various uniform-density tori that were tested at that time revealed that the polarization time lag at type 1 viewing angles is only slightly longer than the light-crossing time of the inner torus radius. In the following the torus was ruled out as a reverberation source because the observed time lags were shorter by a factor of five. They instead corresponded to the light-crossing time of the BLR. Polarization reverberation contains important seismological information about AGN, but as for

polarization in general, careful modeling is required to correctly interpret it. Next, more central structures like the BLR and the outer parts of the accretion disk need to be included to recover shorter reverberation times. This work is currently underway and will be presented in a forthcoming publication, including dependencies on the density of the circumnuclear region and the cross correlation between polarized and unpolarized flux.

In the meantime, we would like to advocate systematic polarization monitoring campaigns of AGN such as those by Afanasiev et al. (2014, 2015). Although these are long-term projects, they have a high potential to reveal more details of the emission and scattering geometry in AGN.

Acknowledgements. We would like to thank the referee for useful comments and suggestions that improved our paper. We would also like to acknowledge Jean-Marie Hameury for his additional remarks. This research was supported by the CONICYT BECAS Chile grant No. 72150573 and the French Agence Nationale de la Recherche through the POLIOPTIX grant ANR-11-JS56-013-01 and the French Programme Nationale des Hautes Energies (PNHE). We are grateful to the French Government and the French Embassy in Serbia and the Ministry of Education and Science (Republic of Serbia) through the project Astrophysical Spectroscopy of Extragalactic Objects (176001).

References

Afanasiev, V. L., Popović, L. Č., Shapovalova, A. I., Borisov, N. V., & Ilić, D. 2014, MNRAS, 440, 519
Afanasiev, V. L., Shapovalova, A. I., Popović, L. Č., & Borisov, N. V. 2015, MNRAS, 448, 2879
Antonucci, R. 1993, ARA&A, 31, 473
Antonucci, R. R. J. 1984, ApJ, 278, 499
Antonucci, R. R. J., & Miller, J. S. 1985, ApJ, 297, 621
Batcheldor, D., Robinson, A., Axon, D. J., et al. 2011, ApJ, 738, 90
Gaskell, C. M. 1982, ApJ, 263, 79
Gaskell, C. M. 2009, New Astron. Rev., 53, 140
Gaskell, C. M., & Goosmann, R. W. 2013, ApJ, 769, 30
Gaskell, C. M., Goosmann, R. W., Antonucci, R. R. J., & Whysong, D. H. 2004, ApJ, 616, 147
Gaskell, C. M., Goosmann, R. W., & Klimek, E. S. 2008, Mem. Soc. Astron. It., 79, 1090
Gaskell, C. M., Goosmann, R. W., Merkulova, N. I., Shakhovskoy, N. M., & Shoji, M. 2012, ApJ, 749, 148
Goosmann, R. W., & Gaskell, C. M. 2007, A&A, 465, 129
Hönig, S. F., & Kishimoto, M. 2010, A&A, 523, A27
King, A. R., & Pounds, K. A. 2003, MNRAS, 345, 657
Kishimoto, M., Hönig, S. F., Antonucci, R., et al. 2013, ApJ, 775, L36
Lynden-Bell, D. 1969, Nature, 223, 690
Marin, F. 2014, MNRAS, 441, 551
Marin, F. 2016, MNRAS, 460, 3679
Marin, F., Goosmann, R. W., Gaskell, C. M., Porquet, D., & Dovčiak, M. 2012, A&A, 548, A121
Marin, F., Goosmann, R. W., & Gaskell, C. M. 2015, A&A, 577, A66
Mathis, J. S., Rumpl, W., & Nordsieck, K. H. 1977, ApJ, 217, 425
Nenkova, M., Sirocky, M. M., Nikutta, R., Ivezić, Ž., & Elitzur, M. 2008, ApJ, 685, 160
Pounds, K. A., & Page, K. L. 2006, MNRAS, 372, 1275
Pringle, J. E., Rees, M. J., & Pacholczyk, A. G. 1973, A&A, 29, 179
Raban, D., Jaffe, W., Röttgering, H., Meisenheimer, K., & Tristram, K. R. W. 2009, MNRAS, 394, 1325
Ruiz, M., Young, S., Packham, C., Alexander, D. M., & Hough, J. H. 2003, MNRAS, 340, 733
Salpeter, E. E. 1964, ApJ, 140, 796
Shakura, N. I., & Sunyaev, R. A. 1973, A&A, 24, 337
Shields, G. A. 1978, Nature, 272, 706
Siebenmorgen, R., Heymann, F., & Efstathiou, A. 2015, A&A, 583, A120
Smith, J. E., Young, S., Robinson, A., et al. 2002, MNRAS, 335, 773
Smith, J. E., Robinson, A., Alexander, D. M., et al. 2004, MNRAS, 350, 140
Tombesi, F., Cappi, M., Reeves, J. N., & Braito, V. 2012, MNRAS, 422, L1
Tristram, K. R. W., Meisenheimer, K., Jaffe, W., et al. 2007, A&A, 474, 837
Tristram, K. R. W., Burtscher, L., Jaffe, W., et al. 2014, A&A, 563, A82

A&A 613, A30 (2018)
https://doi.org/10.1051/0004-6361/201732464

Astronomy & Astrophysics

A near-infrared, optical, and ultraviolet polarimetric and timing investigation of complex equatorial dusty structures

F. Marin, P. A. Rojas Lobos, J. M. Hameury, and R. W. Goosmann

Université de Strasbourg, CNRS, Observatoire Astronomique de Strasbourg, UMR 7550, 67000 Strasbourg, France
e-mail: frederic.marin@astro.unistra.fr

Received 15 December 2017 / Accepted 23 January 2018

ABSTRACT

Context. From stars to active galactic nuclei, many astrophysical systems are surrounded by an equatorial distribution of dusty material that is, in a number of cases, spatially unresolved even with cutting edge facilities.
Aims. In this paper, we investigate if and how one can determine the unresolved and heterogeneous morphology of dust distribution around a central bright source using time-resolved polarimetric observations.
Methods. We used polarized radiative transfer simulations to study a sample of circumnuclear dusty morphologies. We explored a grid of geometrically variable models that are uniform, fragmented, and density stratified in the near-infrared, optical, and ultraviolet bands, and we present their distinctive time-dependent polarimetric signatures.
Results. As expected, varying the structure of the obscuring equatorial disk has a deep impact on the inclination-dependent flux, polarization degree and angle, and time lags we observe. We find that stratified media are distinguishable by time-resolved polarimetric observations, and that the expected polarization is much higher in the infrared band than in the ultraviolet. However, because of the physical scales imposed by dust sublimation, the average time lags of months to years between the total and polarized fluxes are important; these time lags lengthens the observational campaigns necessary to break more sophisticated, and therefore also more degenerated, models. In the ultraviolet band, time lags are slightly shorter than in the infrared or optical bands, and, coupled to lower diluting starlight fluxes, time-resolved polarimetry in the UV appears more promising for future campaigns.
Conclusions. Equatorial dusty disks differ in terms of inclination-dependent photometric, polarimetric, and timing observables, but only the coupling of these different markers can lead to inclination-independent constraints on the unresolved structures. Even though it is complex and time consuming, polarized reverberation mapping in the ultraviolet-blue band is probably the best technique to rely on in this field.

Key words. galaxies: active – polarization – radiative transfer – scattering – circumstellar matter – stars: general

1. Introduction

Dusty disks are detected in a variety of astronomical sources that range from stars to the innermost regions of active galactic nuclei (AGN). A disk[1] naturally forms when matter with sufficient angular momentum is accreted onto a central object, regardless if it is a star, a neutron star, or a black hole. We know that dust grains can form at the outer rim of AGN and young stars accretion disks (Mundy et al. 1993; D'Alessio et al. 1998, 1999; Czerny & Hryniewicz 2012) and the fact that disks are ubiquitous in the Universe naturally provides clues to the physics of accretion in various environments. By studying dust disks, we can put strong constraints on the formation mechanisms of dust grains, and how they survive and evolve.

Equatorial dusty mixtures can be probed locally, i.e., within the Galaxy, by observing stars. It is thought that almost all stars are born with circumstellar disks (Beckwith & Sargent 1996; Hillenbrand et al. 1998). Young stars often show protoplanetary disks, which are a collection of material left over from the stellar formation process. In Keplerian orbit, this circumstellar, flared region contains both gas and dust with a gas to dust ratio of ~100 (Beckwith et al. 1990). While the exact composition of dust in protoplanetary disks is poorly known, silicates and amorphous carbons covered by icy mantles are favored (e.g., Pollack et al. 1994 or, more recently, Jones 2016). After the accretion stage of the young stellar object, the dust mixture in the disk continues to evolve. The innermost grains start to collide and stick together, forming larger grains that sink toward the disk mid-plane due to the vertical component of gravity. Substantial dust settling can profoundly alter the geometry of the protoplanetary disk: the photosphere of the disk is dragged down with the dust (Dubrulle et al. 1995; Schräpler & Henning 2004). Turbulence, if any, tends to mix the grains back up again, resulting in non-homogeneous equatorial structures around the star that can be probed in the mid- and far-infrared, where dust thermally re-emits (Dullemond et al. 2007).

The infrared re-emission of dust was used to infer the existence of dusty disks around more evolved stars, such as cool, old white dwarfs in planetary nebulae (Farihi et al. 2009; Clayton et al. 2014). A dust-related infrared excess was first discovered around the Helix planetary nebula by Su et al. (2007) and later surveys have found several other dust-encircled candidates (Chu et al. 2011). The 24 μm flux densities of hot white dwarfs and central stars of planetary nebula are more than two orders of magnitude higher than their expected photospheric emission, revealing the presence of cold dust disks (Chu et al. 2011).

[1] Collimated polar outflows, quasi-spherical winds, and jets can also form during accreting periods, but these are beyond the scope of this paper.

The disk, in those cases, may derive from the AGB phase of the star evolution (Clayton et al. 2014) or collisions of Kuiper belt-like objects (Bilíková et al. 2012). It is not easy to distinguish between the two formation mechanisms as the system is not fully resolved. Disk sizes are hard to measure because the outer parts are cool and emit weakly, but it is thought that circumstellar disks extend up to a few hundreds of astronomical units (see, e.g., Vicente & Alves 2005). The inner part of the dusty disk is set up by the sublimation radius that depends on the dust composition and temperature of the central source (Kishimoto et al. 2007). Current millimeter and submillimeter/interferometers provide images of the dust and gas outer disks with an angular resolution better than 1″ (i.e., 150 AU at the distance of the nearest star forming regions). As an example, the Atacama Large Millimeter/submillimeter Array (ALMA) can reach a resolution of 0.5″ at 950 GHz in its most compact 12 m array configurations. Using longer baselines (up to 14 km), Andrews et al. (2016) have successfully traced millimeter-sized particles down to spatial scales as small as 1 AU (20 mas).

High angular resolution observations can also be obtained in the K and N bands with the Keck Interferometer (Eisner et al. 2007) and the Very Large Telescope Interferometer (Jaffe et al. 2004), respectively. The former authors successfully resolved the circumstellar material 2.2 μm emission within the first astronomical unit around young stars. The later spatially resolved a parsec-sized torus-shaped distribution of dust grains in the Seyfert galaxy NGC 1068. This circumnuclear dust region was invisible to our instruments for a long time and is now at the edges of the resolution capabilities of current telescopes (Beckert et al. 2008). However, the true morphology and composition of this equatorial region is still largely unknown; it would require us to resolve sizes inferior to a fraction of a parsec at mega-parsec distances. We thus need to find another observation technique to reveal the geometry of unresolvable dusty disks either around young stars or supermassive black holes.

Indirect techniques such as Doppler tomography (Marsh & Horne 1988) or eclipse mapping (see, e.g., Horne 1985) have widely been used for cataclysmic variables, but these are restricted to binary systems and cannot be applied to isolated stars or AGN. Another very successful method that can go beyond the resolution capabilities of current telescopes is the observation of polarized light. Polarization has proven to be independent of the size of the emitting/scattering region. Only the observed polarization degree and position angle are sensitive to the morphology, composition, and magnetic fields of the media that can emit, scatter, or absorb photons. Observing the polarized light of NGC 1068, Antonucci & Miller (1985) successfully unveiled the broad emission lines that were undetectable in the total flux spectrum. Those lines, obscured by the equatorial distribution of dust around AGN cores, were only revealed thanks to near-infrared, optical, and ultraviolet spectropolarimetry. They laid the foundations of the unified model of AGN (Antonucci 1993). Polarimetry is also extremely powerful in detecting dusty equatorial structures around bright stars. The polarized light, emerging from scattering of stellar photons on the disk surface, shaves off the unpolarized contribution from the central star. After correcting for stellar starlight dilution only the disk emission is detected thanks to its contrast. Imaging polarimetry then allows the disk inner regions to be revealed down to a few astronomical units (see, e.g., Gledhill et al. 1991; Apai et al. 2004).

Now that we are able to detect the polarized signatures of dusty disks (at least around stars, not yet for AGN), it is of prime importance to determine their true structure. Models from the literature almost systematically use plain, uniform, and constant density disks since they are easier to explore numerically. A simple geometry, reducing the model parameter space, is much less time consuming when radiative transfer or magneto-hydrodynamical simulations are used. Density variations have been sometimes included (see, e.g., Walker et al. 2004; Pinte et al. 2009) and have already revealed a number of photometric and spectroscopic differences with respect to constant-density disks. The same conclusion applies to the disk geometry (Nenkova et al. 2002; Marin et al. 2015). Flared or cylindrical disks are the two most common morphologies used in simulations but it has been shown that the structure of circumstellar and circumnuclear disks is more complex. Clumpy dusty structures have been detected around stars and brown dwarfs (e.g., in the σ Ori cluster, see Scholz et al. 2009) and from galactic structures (e.g., in NGC 4244, see Holwerda et al. 2012). Even if the parsec-scale dust disk around the core of AGN has not yet been resolved to the point of detecting individual clumps, hydrodynamical models predict that large homogeneous distributions of dust cannot be stable (Krolik & Begelman 1988). Various indirect evidences for the clumpiness of AGN tori are detected in the X-rays, where fluorescent line emission (Liu et al. 2016) and variations in the obscuring column density of edge-on Seyferts (Marinucci et al. 2016) strongly suggest a non-uniform equatorial torus morphology.

It is the aim of this paper to investigate in great detail the various morphologies and density stratifications of equatorial dusty disks. By doing so, we want to check whether near-infrared, optical, and ultraviolet polarimetry can shed light on the true geometry of those unresolvable regions. We consider disk parameters (in particular disk sizes) appropriate for AGN, but our results can be easily extrapolated to different environments. We thus study very realistic models of dusty environments that exist in accreting objects and present the radiative transfer code we used in Sect. 2. We compile and discuss our results in Sect. 3, where the photometric flux, polarization degree, polarization angle, and time lags for each of the 15 models are presented. We analyze the benefits, problems, and limitations of polarized time reverberation studies in Sect. 4 by comparing our conclusions to recent observations, and we conclude our paper in Sect. 5.

2. Models of equatorial dusty structures

In the following, we use a geometrical configuration that matches the observational constraints for AGN. Our goal is not to precisely model a circumstellar or a circumnuclear disk. We instead test the impact of different geometries and compositions onto the resulting photometric flux, polarization, and time lags. We consider throughout this paper a flared disk with inner radius 0.1 pc and outer radius 10 pc. The first value corresponds to the inner radius set by dust sublimation theories for a typical Seyfert galaxy whose dust is mainly composed of graphite and silicate grains (Kishimoto et al. 2007). The outer radius is the typical torus extension set by modeling constraints based on spectroscopic and interferometric observations and is of order of 5–10 pc (Meisenheimer et al. 2008; Burtscher & Tristram 2013; Netzer 2015; López-Gonzaga & Jaffe 2016). The half-opening angle of the flared disk is set to 45°. This corresponds to the estimated torus height derived from quasar observations (Sazonov et al. 2015), numerical modeling (Marin et al. 2012; Gnedin et al. 2015), and statistical analyses (Marin 2014, 2016).

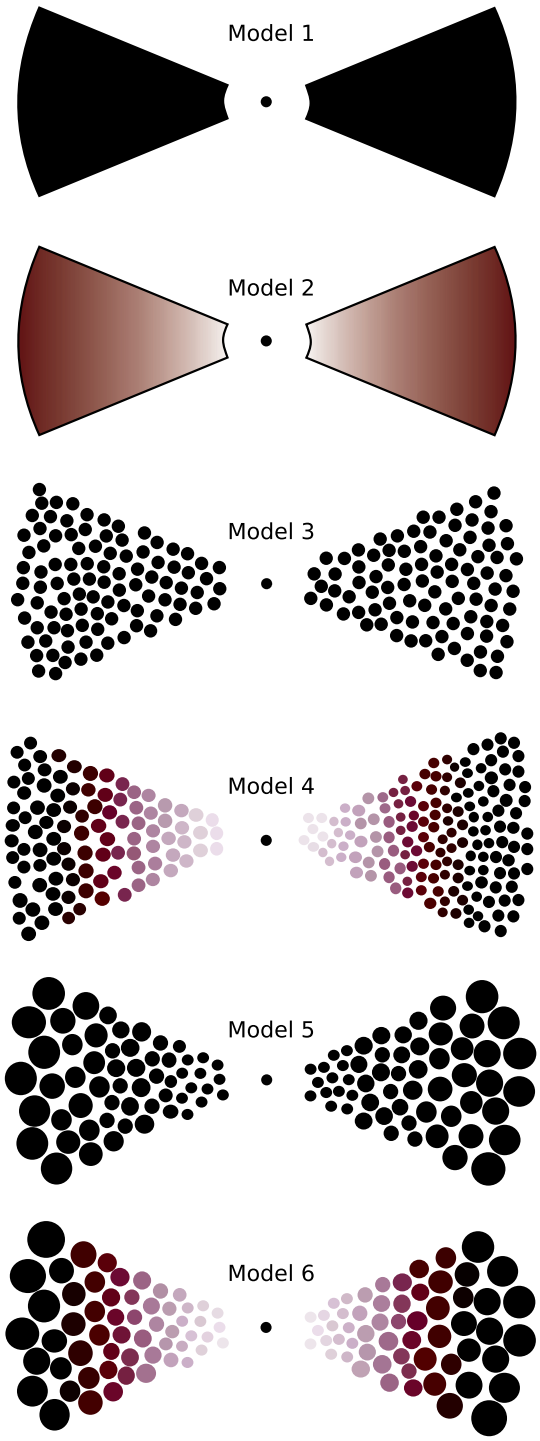

Fig. 1. Unscaled geometrical and density variations for our models of dusty disks. The first two panels show a model with a uniform geometry and the last four panel a set of fragmented disks. A uniform red filling indicates a constant optical depth, while a color gradient indicates a variation in the dust density with increasing radial distances from the central source. Details are given in the text.

2.1. Dusty disks with increasing complexity

We show in Fig. 1 the six different disk geometries we investigate in this paper. We consider first a plain flared disk that is uniformly filled with dust. Its radial optical depth in the V band is larger than 100 to ensure a strong obscuration along the equatorial plane (Antonucci 1993). This is the simplest configuration

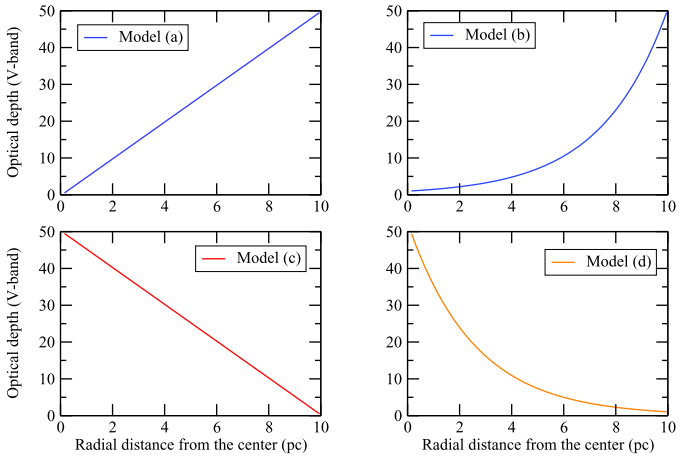

Fig. 2. Theoretical dust distributions corresponding to heterogeneously filled dust disks. Each model is color-coded and shows a different variation of the radial optical depth (in the V band) with increasing distance from the central source. Details are given in the text.

and it is one of the most used in numerical simulations. Model number 2 is also a plain flared disk but its dust density varies with radial distance from the central source. The third model is a clumpy flared disk with clumps of equal sizes and density. Each clump has an optical depth of 50 (Siebenmorgen et al. 2015) and seven to ten clumps are obstructing the line of sight of the observer along equatorial views, ensuring a total optical depth equal to or larger than 100. The non-homogeneously filled counter-part of this disk is model 4, where the dust density varies with the radial distance from the center. Finally, model number 5 is a clumpy disk with clump sizes becoming bigger and bigger as we move away from the center. A clump located at the outer part of the structure is ten times larger than a clump located at the inner edge. In this model the dust density is inversely proportional to the clump radius so that each cloud has a constant optical depth of 50 in the V band. The last model is the same as model 5 but the dust optical depth is no longer constant.

The different distributions of dust used in models 2, 4, and 6 are presented in Fig. 2. We consider four dust distributions, defined by their optical depth in the V band plotted as a function of the radial distance from the central black hole. As the size of the disks is the same for all models, the change in optical depths is only due to variations in dust densities. Model (a) corresponds to a linear increase of the optical depth with increasing distances from the central source. Model (b) is for an exponential growth. Model (c) and (d) follow the inverse trend, model (c) is a linear decrease of the dust optical depth with increasing distances from the center, and model (d) is an exponential decrease. We therefore have 15 different test cases: model 1, models 2(a–d), model 3, models 4(a–d), model 5, and models 6(a–d).

We sample 2000 clumps for each clumpy model, equating to a disk filling factor of ∼25%. The impact of the number of clumps has been studied in Marin et al. (2015) and it was found that the lower the filling factor, the lesser the observed polarization and the higher the total flux. Using a filling factor of ∼25% allows for a flux decrease between the polar and equatorial inclinations of, at least, one order of magnitude. For all models, we fix the dust composition to the Milky Way mixture (Wolf & Henning 1999). This is the standard dust composition observed in the solar neighborhood, but different mixtures can reside in different systems, such as postulated by Gaskell et al. (2004) and Li (2007). In the Milky Way, the dust is essentially composed of

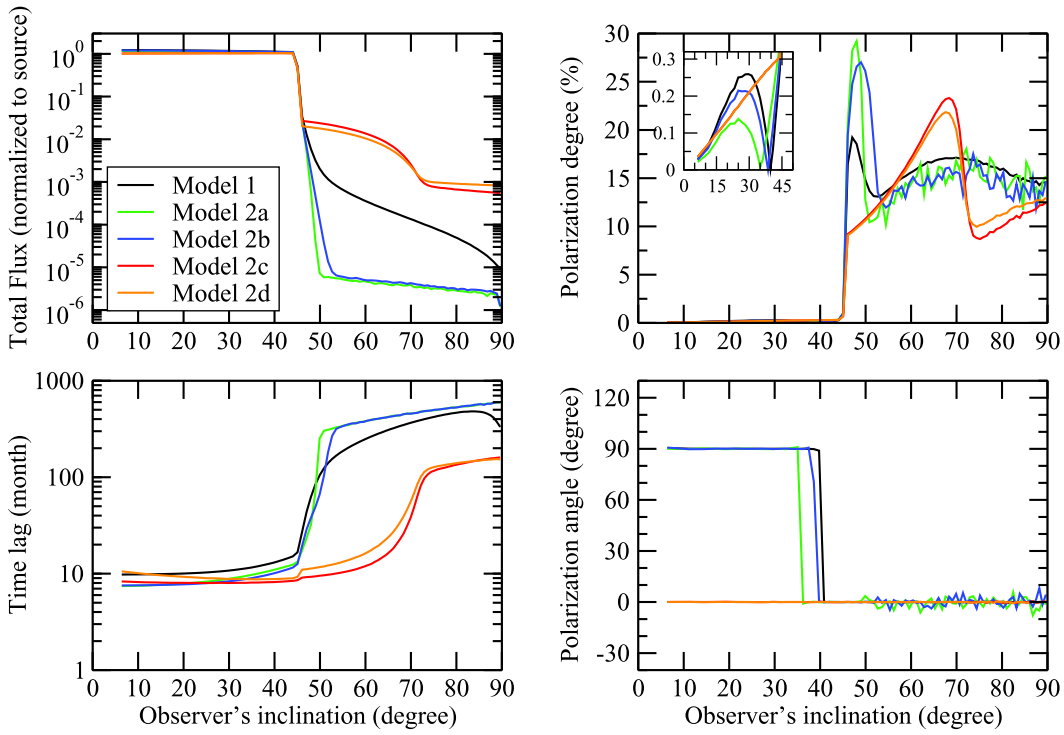

Fig. 3. Near-infrared (10 000 Å) total flux (normalized to the source emission), polarization degree, polarization angle, and time lag (normalized to the size of the disk) as a function of the inclination of the observer. Five plain flared disk models with various dust distributions are presented (see Sect. 2.1 for details).

62.5% carbonaceous dust grains and 37.5% astronomical silicate. Both ortho- and para-graphite are considered with twice as much para-graphite as ortho-graphite (Wolf & Henning 1999). The grain size distribution ranges from 0.005 to 0.250 μm in radii; the distribution $n(a) \propto a^s$ and $s = -3.5$. Varying the dust grain radius distribution or the dust composition results in a different albedo, hence different scattered/absorbed fluxes and polarization. However, in the following, we always compare models with the same dust mixture. The exact dust prescription is then of no importance since we are looking at model differences and not quantitative values. Finally, i is the disk inclination, i.e., the angle between the observer line of sight and the symmetry axis of the disk. Pole-on view corresponds to $i = 0°$, edge-on view to $i = 90°$.

2.2. Polarized radiative transfer

We used the radiative transfer code STOKES to achieve our simulations. Developed by Goosmann & Gaskell (2007) and upgraded by Marin et al. (2012, 2015), STOKES is a Monte Carlo code that simulates the propagation of radiation in a user-defined three-dimensional environment. The code is extensively detailed in the three papers of the series and we only give here a brief summary of its important features. A list of applications of STOKES can be found in Marin & Goosmann (2014).

The STOKES code can model a large range of geometrical shapes that can be filled with electrons, dust grains, atoms, and molecules. Emitting regions can be parametrized as sources with a given spectral shape. Photons, once emitted, travel along straight lines until a reprocessing event happens, depending on the optical depth of the media; this is calculated as $\tau = \int_0^l \sigma n(z)\,\mathrm{d}z$, where $n(z)$ is the number density of that material at z, and σ the attenuation cross section. Photons can be scattered, absorbed, and re-emitted in all directions according to the Mie, Rayleigh, Thomson, or Compton laws. Multiple scattering can occur and the four components of the Stokes vector are modified at each scattering event. A spherical web of virtual detectors registers each escaping photon, saving its polar and azimuthal coordinates together with the intensity, polarization (linear and circular), and time lag. The polarization we measured is the scattering-induced, linear, continuum polarization degree ranging from 0% (unpolarized) to 100% (fully polarized). The code can be parallelized and it takes a few days on a basic computer for a computation such as presented in this paper to sample 10^{10} photons.

In the following, we ran our models for three different wavebands: near-infrared (mono-energetic photon emission centered at 10 000 Å), optical (5500 Å), and ultraviolet (2000 Å). Since the scattering phase function of dust is energy dependent, we aim to find which is the best suited waveband for a polarimetric detection of the specific features of complex dusty disks. The polarimetric results we present are entirely from scattering. We do not account for external dilution by the host galaxy, stellar starlight, or thermal reprocessing by dust grains. This might have an effect on the polarization signatures, particularly in the infrared domain where dilution by the host galaxy is much more important than in the ultraviolet band (see, e.g., Bolzonella et al. 2000), and this is discussed in Sect. 4. We registered the flux, polarization, and time lag along 40 polar directions, from the symmetry axis of the model to the equatorial plane, equally spaced in cosine. We azimuthally integrated the signal to get better statistics. It was shown in Marin et al. (2015) that, even for a clumpy distribution, an azimuthally averaged value is representative of the system provided it is not highly non-axisymmetric.

3. Results

3.1. Uniform disks

We present our first results in Figs. 3–5 for the near-infrared, optical, and ultraviolet bands, respectively. These results corresponds to models 1 (plain, uniformly filled dusty flared

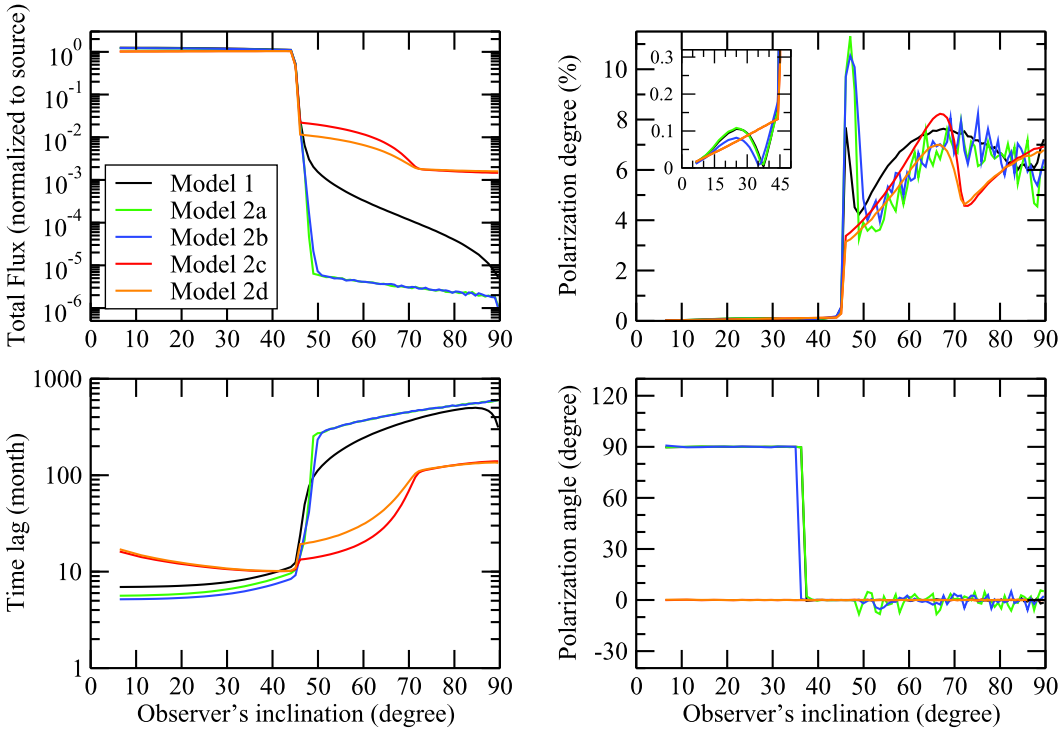

Fig. 4. Same as Fig. 3 but in the optical band (5500 Å).

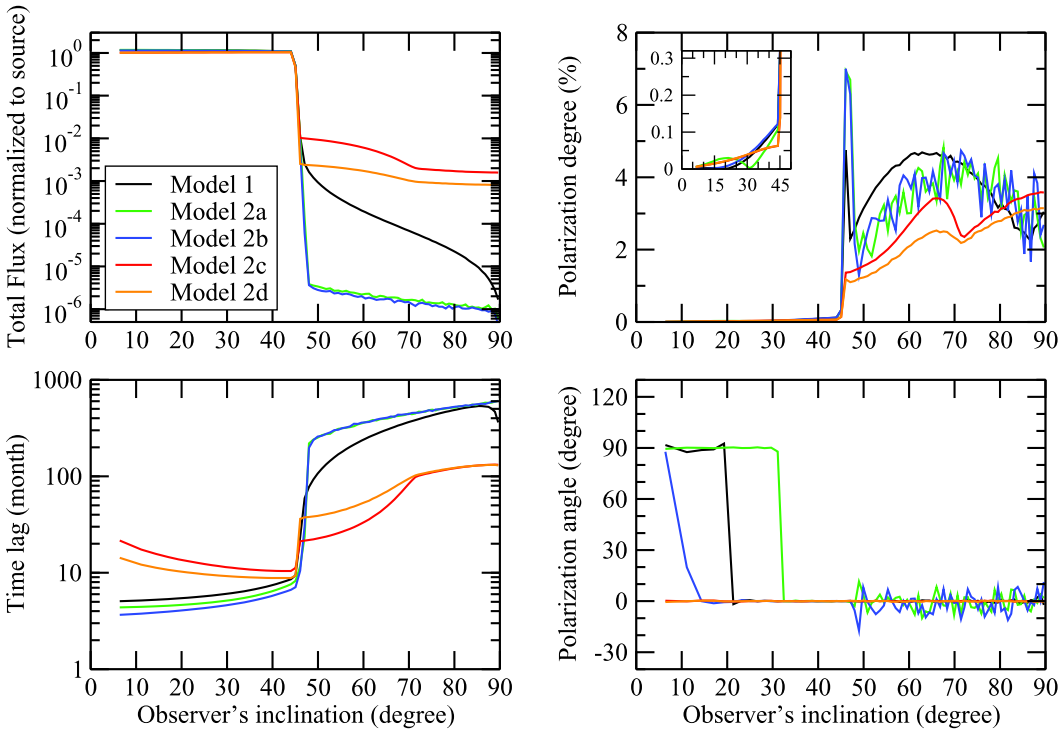

Fig. 5. Same as Fig. 3 but in the ultraviolet band (2000 Å).

disk) and 2 (plain disks with radial dust stratification). We investigate, in model 2, all four dust prescriptions (a), (b), (c), and (d) according to Fig. 2.

3.1.1. Radiation path

Because of the large disk optical depth resulting in multiple scattering, the radiation path is not straightforward. Photons may scatter more than twice before reaching the observer, especially if the disk is clumpy. We illustrate in Fig. 6 the various trajectories the photons can have.

The top panel illustrates the case of an observer situated almost along the symmetry axis of the system, i.e., along the polar direction. In this case, there is a direct view of the central source and photons may travel freely toward the observer (dotted orange line). This is the direct flux, which is unpolarized. If photons are emitted along the equatorial plane, they encounter the disk funnel (dashed pink line). If not absorbed, these photons may scatter backward and be reprocessed onto the opposite funnel side until they are absorbed or able to escape. Because of the non-isotropic scattering phase function of Mie scattering, photons can also penetrate further into the disk (long-dashed cyan

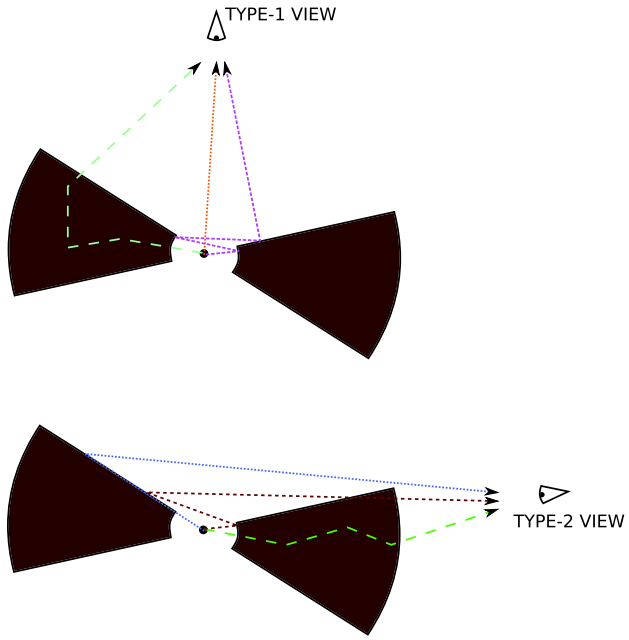

Fig. 6. Illustration of different photon paths due to multiple scattering. See text for details. *Top*: pole-on (type-1) view is shown and *bottom*: edge-on (type-2) view is shown.

line). Radiation scatters at various positions before escaping at large distances from the central source. Depending on the position of the last scattering event, its polarization position angle can be either parallel or perpendicular. For the remainder of this paper, we consider that a polarization position angle of 90° indicates a polarization angle parallel to the projected symmetry axis of the disk. This is the signature of equatorial scattering. A polarization angle of 0° is thus perpendicular to the model axis and traces scattering event happening preferentially close to the pole of the model. We note that when a model is perfectly axisymmetric, the polarization angle can only take two values, 0° or 90°. Otherwise, as in the case of a distribution of clumps, various polarization angles can be obtained, related to the statistics of the clumps.

The bottom panel of Fig. 6 illustrates the case of an almost edge-on inclination. The central source is obscured by dust and no longer visible. Photons can escape via multiple scattering along the equatorial plane if the dusty medium is not too optically thick or if there are gaps between the clouds (green long-dashed line). The majority of radiation preferentially scatters onto the disk surface opposite to the observer and then reach the detectors. This could happen with only one scattering event, where photon is emitted at an angle coincident to the half-opening angle of the disk (dotted blue line) or due to multiple scattering (dashed red line). When the inclination of the system is close to 90°, the obscuration is maximal and the amount of photons that have backscattered onto the disk surface opposite to the observer (blue and red lines) is minimal.

3.1.2. Total flux

Focusing first on the normalized photon flux (top left panel of Figs. 3–5), we see an almost inclination-independent flux value until the line of sight of the observer becomes obstructed by the dusty disk. Because the central source is unobscured, there is little contribution from the flared disk that absorbs/scatters a small fraction of radiation. Nonetheless, models 2(c) and 2(d) present a slightly smaller (by a factor 1.3) flux at those inclinations. As the optical depth is maximum at the inner disk radius (see Fig. 2), radiation is more heavily absorbed. Thus, there is less photon scatter toward the polar axis than for the other cases. Once the dusty material intercepts the line of sight of the observer, the flux drops by several orders of magnitude. For a plain disk where density decreases with radial distances from the center (models (c–d)), the minimum flux is about three orders of magnitude lower than at face-on inclinations. Radiation that successfully crossed the first, dense layers of the inner disk region can freely propagate toward the disk outer radius. The number of photons is thus higher than in the case of a disk with a constant-density profile (model 1). Here, the flux drops by five orders of magnitude and the attenuation is almost linear with inclination. The attenuation is even stronger for the last two models (a–b) for which when the dust density increases with radial distances from the source, the flux obscuration is very efficient. Between $i = 45°$ and $i = 50°$, the flux sharply drops by five orders of magnitude and then stays constant at edge-on inclinations. In this specific case, photons have traveled far inside the dusty material before encountering the densest layers of dust. Radiation then becomes trapped inside the dust disk and naturally suffers from heavy absorption caused by multiple scattering. The emerging flux at edge-on inclinations is thus extremely weak as compared to the source.

As the photon energy increases, models (c–d) with decreasing radial optical depth from the center of the disk show a slightly higher edge-on normalized flux, while it is the opposite for the other cases. This complex behavior is related to the albedo and the scattering and extinction cross sections of dust. The albedo is flat in the optical band but decreases in the ultraviolet and infrared regimes. On the other hand, the scattering cross section decreases regularly with wavelength. An illustration is given in Fig. 3 in Goosmann & Gaskell (2007). The combination of the two factors allows ultraviolet radiation to cross a thicker layer of dust close to the inner radius of the disk: more ultraviolet photons can penetrate the disk, but these photons get more scattered or absorbed than optical or infrared photons. However, in the case of a model with increasing dust density with radial distance from the source, the first layers of dust are optically thin, and the same ultraviolet photons travel farther inside the dusty material before they are absorbed or scattered. Scattered photons more easily escape along the polar direction, where the remaining optical depth is smaller, rather than toward the equatorial plane where the optical depth is higher. This results in a decrease of the observed flux even at higher photon energies.

3.1.3. Polarization properties

The polarization properties of the five models (right panels of Figs. 3–5) strongly differ both in terms of polarization degree and polarization position angle. At polar inclinations, the degree of polarization is always small, less than a percent. This is due to the strong dilution effect of the unpolarized primary source that outshines the reprocessed component. The polarization degrees are marginally dependent on the half-opening angle of the disk (Marin et al. 2012) but are very sensitive to its composition. There are however differences between models, even for low inclinations. As it can be seen in the small zoom-box inside the polarization degree panels, a uniformly filled dusty disk produces the highest polarization degrees, while a disk with a linear increase of the dust density with radial distance from the center has the lowest continuum polarization. If the dust

density decreases with radial distances (models (c) and (d)), the degree of polarization linearly increases with inclination until $i = 45°$. From 0° to 45°, the other three models show a nonlinear variation of their polarization properties, which is a behavior that is strongly impacted by the amount of reprocessed flux, hence by the model itself. This can be clearly seen when considering the intrinsic polarization position angle. When the dust density is constant or increases with radial distance from the center, the polarization angle is 90° whereas it is 0° otherwise. The first three models are dominated by scattering along the equatorial plane, producing a parallel polarization angle, until the line of sight of the observer is obscured by the dusty medium. Scattering then occurs along the polar directions, where photons reprocess on the flared disk surface opposite from the position of the observer; see Fig. 6. The polarization angle naturally rotates and the transition between the two polarization states causes the polarization degree to decrease around $i = 45°$ (the half-opening angle of the flared disk). When the disk optical depth decreases with radial distances from the source, the inner edge of the disk is similar to a thick wall of dust and radiation preferentially scatters along the polar direction if it is to escape from the disk, hence the perpendicular polarization angle.

As soon as the source is no longer directly visible by the observer, the polarization angle is fixed for all models (0°) and the polarization degree rises due to Thomson laws. In the case of a uniformly filled plain flared disk, the maximum infrared polarization degree is ∼20% at $i = 50°$, where polar scattering dominates. The polarization then decreases with increasing inclinations because it becomes more and more difficult for radiation to escape the dust funnel; this the case with the exception of multiple scattering, which induces a natural depolarization effect. In the case of models 2(a) and 2(b), the maximum of polarization (27–29%) is reached for inclinations close to 45°. The polarization degree then decreases for the same reasons as before, but the final edge-on value is lower than in the previous case. This is due, as explained above, to the confinement of radiation inside the flared disk and the subsequent heavy absorption. It also explains the lower statistics at edge-on inclinations. Finally, for the last two models in which the dust density decreases with radial distances from the center, the polarization degree peaks at inclinations close to 70°. The maximum infrared polarization is as high as 23%, and then decreases at equatorial orientations, and has a polarization level similar to the uniformly filled case. We thus see that the maximum polarization degree from a plain flared disk occurs for various inclinations and strongly depends on the radial distribution of dust. We see similar behaviors in terms of polarization angles and polarization degrees for all three wavebands considered here, and the polarization degrees decreases at bluer wavelengths. We also note that the rotation of the polarization position angle of model 2(a) occurs at slightly different inclinations for different energies. Those two phenomena are due to the increase of the dust scattering cross section with decreasing wavelengths.

3.1.4. Time lags

The last panel of Figs. 3–5 (bottom left) represents the averaged time lag between actual photons reaching the observer and photons emitted by the central source that would not have suffered any scattering. Direct emission has a time lag of zero. This quantity, with respect to the previous values, is not directly observable as real cosmic photons are emitted at different times. The true averaged time lags must be reconstructed from observations by comparing polarized and primary light curves through theoretical transfer functions. The time lags we present therein are to be used as time indicators of the complexity of the radiation paths and the difficulty photons can have to escape from the dusty disk.

We see that the time lag is rather small for pole-on inclinations. The continuum is directly seen by the observer (zero time lag) and polarized radiation mainly scatters on the inner disk funnel before reaching the observer, lagging the continuum by about ten months. In the infrared band, the uniformly filled model shows the longest times lags but the increase with respect to the other models between 0° and 45° orientations is merely detectable. The five models only become truly unique in terms of temporal signatures at inclinations larger than 45°. When the dust density increases with radius, the time lag abruptly increases, and at that point the inclination becomes slightly larger than 45° and then becomes stable. Since there is a very small number of photons that can escape from the densest outer layers of the disk (see the flux plot), most of the radiation detected at those angles is due to the backscattering of photons onto the opposite disk edge. Because the photon travel length is almost similar at all edge-on inclinations, the time lag stabilizes at 400–600 months. A model with a constant-density dust prescription has a similar behavior but the time lags are less important since radiation faces a constant, high optical depth and thus scatters many times before escaping but is not trapped in the outer regions, in contrast with the previous cases. The time lag slightly drops at perfect equatorial inclinations since photons that have backscattered on the opposite disk funnel are not longer able to reach the observer and thus do not delay the averaged time response. Finally, for models with decreasing radial dust densities, time lags remain very constant before and after the transition angle, solely showing a small increase a inclinations larger than 70°. This is also due to the amount of backscattered photons that outnumbers those that have traveled through the equatorial plane (i.e., with a smaller time lag).

We finally note that the time lags differ in the near-infrared and the optical/ultraviolet bands, when energetic radiation can penetrate further in the dust material. For models with denser dust layers close to the source, IR photons mainly scatter onto the dust funnel while UV photons penetrate more easily in the material, increasing their time lag. The change in waveband affects the three other models in the opposite way: their time lag at polar views is lower. This is due to the combination of albedo and scattering/absorbing cross-section variations, as explained above.

Summarizing what we have found for the plain flared disks, we have shown that different dust prescriptions result in specific inclination-dependent attenuations of the flux. If the dust layers become thicker with increasing distances from the central source, fewer photons are detected toward the equatorial regions. It is not the case for the other configurations that allow more radiation to be detected at high inclinations. The variations of the polarization degrees and angles are also very characteristic; the polarization is maximum for models with radially increasing dust densities. Those same models also provide the highest time lags at equatorial views at all three wavebands. We note that the differences are less pronounced for type-1 (pole-on) inclinations, where the structure of the equatorial distribution of dust has a lesser impact on the averaged time lags. This prevents a very clear determination of the morphology of the disk from time reverberation studies that can be achieved only for low inclination objects, showing the importance of coupling timing and polarimetric studies to break degeneracies.

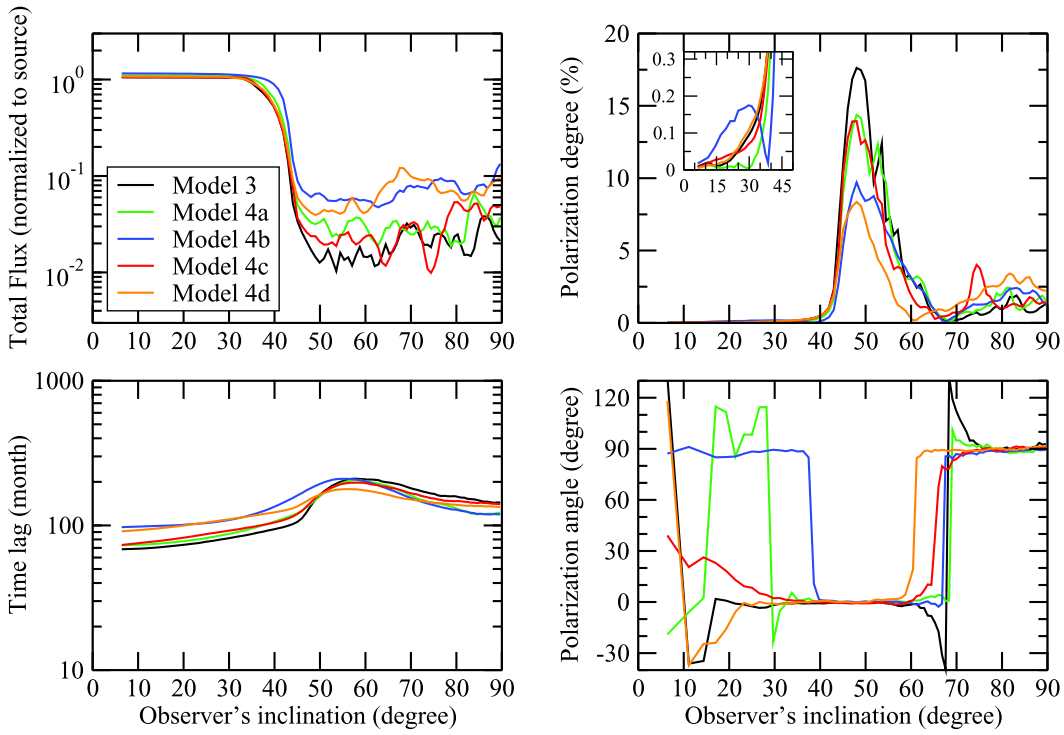

Fig. 7. Near-infrared (10 000 Å) total flux (normalized to the source emission), polarization degree, polarization angle, and time lag (normalized to the size of the disk) as a function of the inclination of the observer. Five clumpy flared disk models with clumps of constant radius but different dust distributions are presented (see Sect. 2.1 for details).

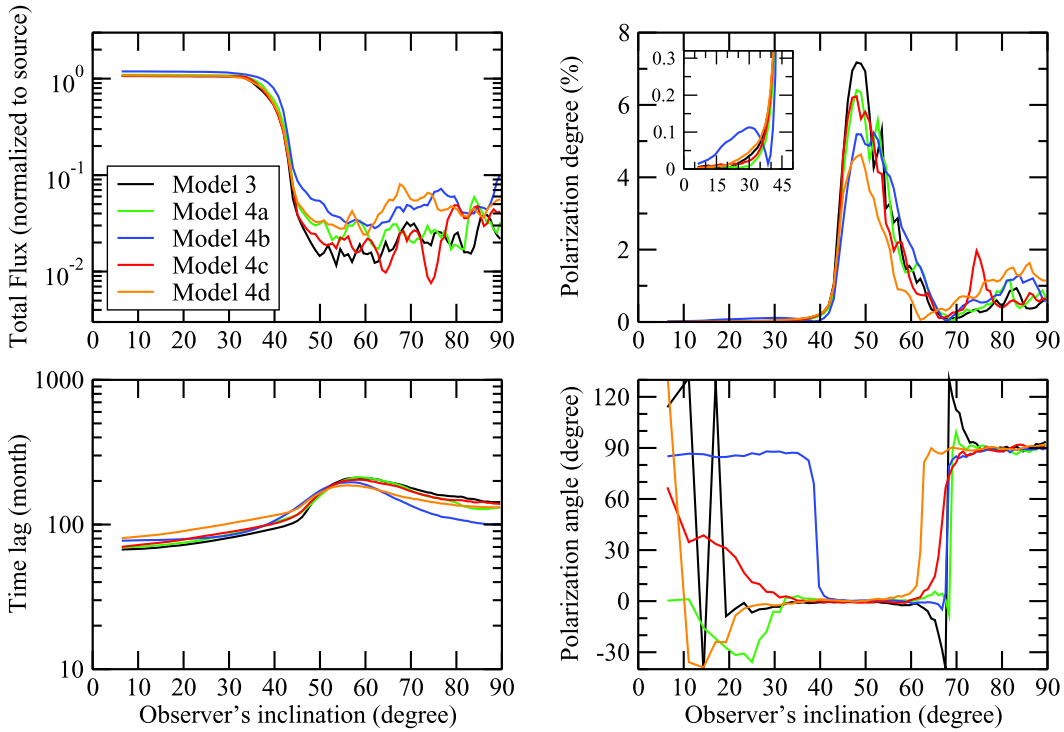

Fig. 8. Same as Fig. 7 but in the optical band (5500 Å).

3.2. Fragmented disks with constant-radius clouds

Our second series of models focuses on fragmented disks with clumps of equal sizes. We examine in Figs. 7–9 a model in which the optical depth is the same for all clumps (fixed to 50 in the V band, model 3) and a model in which the dust opacity varies with radial distance from the central source (model 4). In the later case, we consider the same four dust prescriptions (a), (b), (c), and (d) as previously (see Fig. 2).

The normalized photon fluxes are maximum at polar inclinations as discussed in the previous section. However the flux attenuation due to obscuration is much less important at edge-on orientations. The clumpy structure of the disk is responsible for gaps between the cloudlets, allowing radiation to escape more easily thanks to multiple scattering. The interclump medium is pure vacuum here, but similar results are found for a clumpy two-phased medium with high density clumps embedded in a low density interclump dust (Stalevski et al. 2012). The flux attenuation is model-dependent. In the infrared, fluxes along the equator are smaller by about one order of magnitude than the polar value for models with exponential opacity distributions, and by almost two orders of magnitude in the linear case. The constant-density

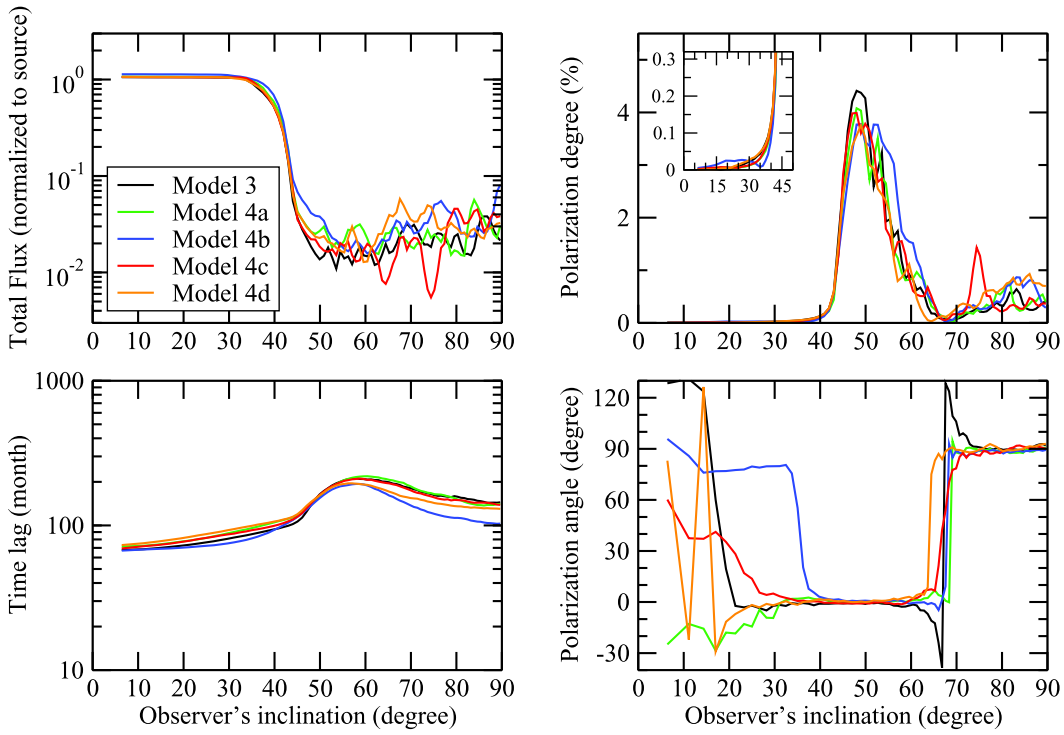

Fig. 9. Same as Fig. 7 but in the ultraviolet band (2000 Å).

model (model 3) presents the lowest equatorial flux. We therefore see that the dust distribution has a profound impact on the quantity of transmitted flux at edge-on views. The photon fluxes are almost inclination-independent once the line of sight of the observer has crossed the disk horizon with a smooth transition between $i = 35°$ and $i = 50°$. The geometry of the system drives the shape of the curves and all five models appear similar (albeit their flux levels). Moving toward shorter wavelengths has no impact on the shape of the curve but the derived photon flux at edge-on inclinations is slightly different owing to the combined effect of albedo and cross section. All models appear to give equivalent fluxes along the equatorial plane, between one and two orders of magnitude less than along the pole.

The polarimetric results (right panels of Figs. 7–9) are very different from the plain flared disk models and are also characteristic of the model used. Whereas the infrared polarization degree along polar directions for the plain disk cases can reach ~0.25%, here it is at best 0.17% for the model with an exponentially increasing dust opacity with radial distances from the source (model 4(b)). For this model, radiation mainly scatters in the equatorial plane until this radiation reaches the outer part of the disk. At this location, the dust density is maximum and the resulting polarization position angle is equal to 90°. A clumpy disk with a linear increase of dust opacity with distance (model 4(a)) also presents a 90° polarization angle when observed edge-on, but its polarization degree is smaller. The seemingly chaotic variations of the polarization angle are due to the clumpiness of the medium and not to insufficient statistics. For the other models (model 3 and models 4(c–d)), the level of linear polarization at polar inclinations is very low because of the inefficiency of the clumpy disk to scatter photons toward the observer. The resulting polarization angle is 0°. This efficiency increases with inclination as the line of sight of the observer becomes obstructed by clumps. The infrared polarization degree sharply rises up to 18% in the case of constant-density clumps (model 3). For dust densities that decrease linearly (model 4(c)), the maximum polarization degree is 15% and for the last two models that are much less capable of absorbing/scattering radiation, the maximum polarization is about 10%. For all models, the polarization position angle is equal to 0° between 40°–60° inclinations since polar scattering dominates. At larger inclinations, there is a rotation of the polarization angle for all models: the polarization angle becomes parallel while the polarization degree decreases. Scattering along the equatorial plane is now the easiest path to escape the clumpy dusty disk. This results in low infrared polarization degrees with 90° polarization position angles. This behavior was already revealed in Marin et al. (2015) and Marin & Schartmann (2017) for constant-density clumpy models, but we now show that their results also apply to more complex dust distributions. As for the plain disk discussed in Sect. 3.1, we find a wavelength-dependent polarization variation, the maximum polarization degree of the models decreasing for shorter wavelength. This is due to a smaller scattering cross section when the photon energy increases, which allows radiation to travel more easily through the dusty structure without interacting.

The time lag results (bottom left panel of Figs. 7–9) are also very different from their plain disk counterparts. Even at polar inclinations the time needed to escape from the dusty structure is large for photons that have scattered only once or twice. Since the medium is clumpy, radiation has traveled far inside the disk before being scattered toward the observer. The time lag is thus about ten times larger than for a plain disk, where radiation mainly scatters inside the dust funnel. We note that this is not due to a higher albedo, but rather to the existence of vacuum between the cloudlets that allows radiation to travel without being absorbed. Model 4(b) presents the highest time lags due to the exponential increase of optical depth with distance to the source. Only the outer parts of the disk are filled with high density, high opacity clumps. Photons thus travel a large distance before these photons are scattered toward the observer. All other models show approximatively equal time lags, and the lowest values are obtained for the constant-density sphere model (model 3). When obscuration becomes efficient (at inclination larger than

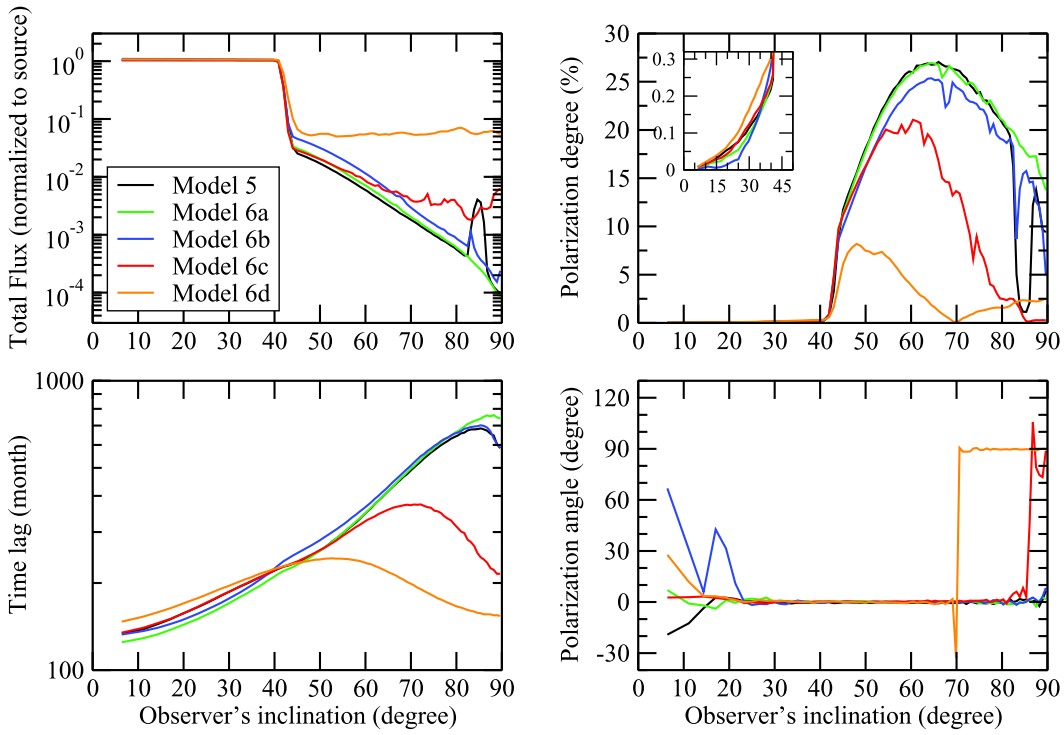

Fig. 10. Near-infrared (10 000 Å) total flux (normalized to the source emission), polarization degree, polarization angle, and time lag (normalized to the size of the disk) as a function of the inclination of the observer. Five clumpy flared disk models with clumps of increasing radius and different dust distributions are presented (see Sect. 2.1 for details).

45°), the time-lag values increase by a factor ~2 depending on the model. This increase correlates with the flux attenuation and the rise of polarization degree observed in other panels. This is a clear indication for a maximum efficiency of obscuration and a large number of scattering events. Finally, when equatorial scattering dominates at edge-on inclinations, the time lags decrease but stay larger than at polar angles. The dependence of time lags with inclination is very similar at shorter wavelengths, and there is only a marginal quantitative decrease.

We conclude that, for clumpy disks with constant radius spheres, the attenuation between a polar and an equatorial inclination is not very effective. The transition between the two extreme inclinations is smooth and operates around the half-opening angle of the dusty structure. If the half-opening angle is not the same for all observable sources, then it becomes impossible to distinguish between various dust stratifications. However polarimetry can reveal the distribution of dust with respect to the central source as the polarization degree reaches different maxima for different cases. The best waveband for observing the polarimetric signatures of clumpy tori is in the near-infrared, where polarization levels larger than 10% are expected for a narrow range of inclinations. Different dust structuring also imprints the polarization position angle with specific values at polar orientations. Finally, reverberation measurements hardly differentiate between the different models since they all give the same inclination-dependent curves. The time lags they produce are too similar to be clearly distinguished.

3.3. Fragmented disks with variable clump sizes

Our last set of models is presented in Figs. 10–12. In this case, the dusty disk is clumpy and the clump radii increase with distances from the central source. We arbitrarily set the radius of clumps situated at the outer part of the structure to be ten times larger than clumps located at the inner edge. Similarly to Sects. 3.1 and 3.2, we examine a model in which the dust opacity is constant for each clump (model 5) and four models (6(a)–(d)) in which the dust opacity varies with radial distance from the source (see Fig. 2).

The normalized total flux appears to be constant at polar viewing angles since, as previously, it is dominated by direct flux from the central source. At low angles, the fluxes are inclination- and model-independent. Differences only appear when the line of sight of the observer crosses the dusty disk. In the case in which the opacity exponentially decreases with distance, the disk does not efficiently block radiation at equatorial viewing angles. The flux has decreased by only one order of magnitude. The gaps between the clouds and the presence of low opacity, large dust cloudlets at the outer disk radius do not allow for a large obscuration. If the dust opacity decreases linearly, obscuration is slightly more efficient since the cloud opacity is still higher than 10 (V band) at 8 pc from the source (while it is about 2–3 in model 6(d)). If the disk is composed of low opacity inner (small) clouds and high opacity outer (large) clouds, radiation is more heavily absorbed. Fluxes are about four orders of magnitude lower at extreme equatorial inclinations for the three remaining models (models 5, 6(a), and 6(b)). The flux decrease with inclination is exponential for these three cases and the transition between unobscured and obscured sources is sharp at around the disk half-opening angle. The fluctuations we see in the flux curves are due to the distribution of clouds inside the model. Some features might appear for different realizations of clumpy disk models if a given equatorial line of sight is not obscured by several optically thick clouds. This occurs, for example, in Fig. 10, models 5 and 6(c), at inclinations larger than 70°. The appearance of peaks and dips in the photometric curves are wavelength-dependent. As the photon energy decreases, radiation is less absorbed by dust grains and, if there is not enough dusty material to block radiation along a given direction, photons escape more easily. This causes the low amplitude peaks of flux in the photometric curves observed in, for example, 6(d), which are visible in the ultraviolet but not in the infrared.

The polarimetric plots (right panels of Figs. 10–12), show a sharp rise of polarization with increasing inclinations. At polar

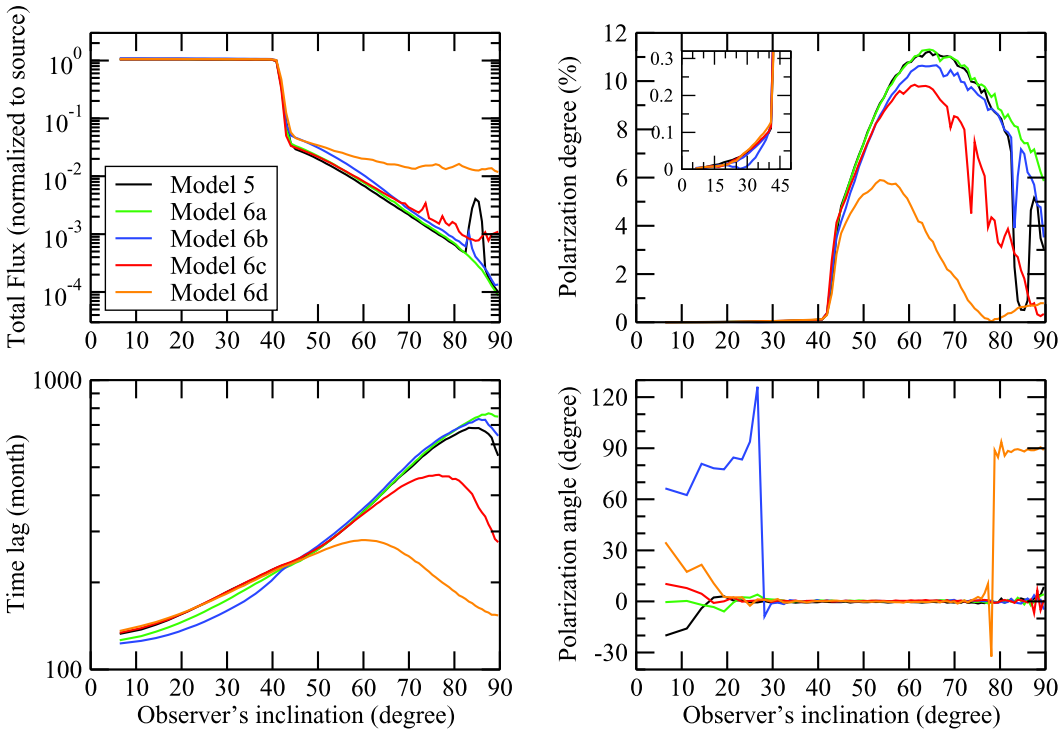

Fig. 11. Same as Fig. 10 but in the optical band (5500 Å).

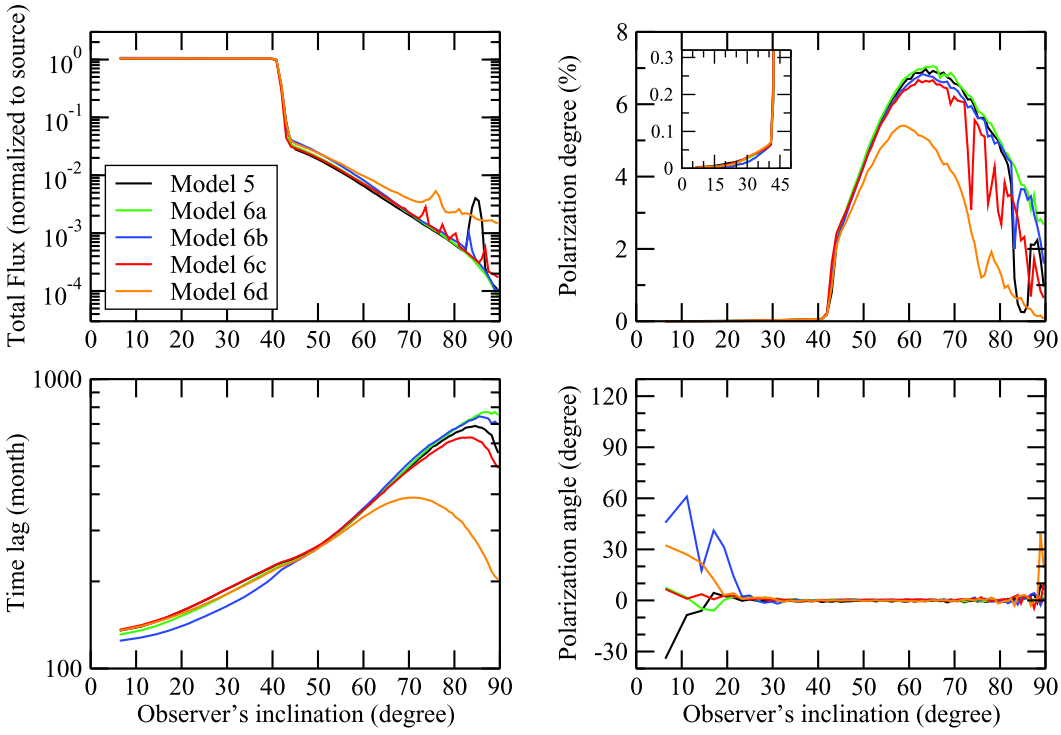

Fig. 12. Same as Fig. 10 but in the ultraviolet band (2000 Å).

angles, the polarization degree exponentially rises up to 0.3%. The associated polarization position angle is 0° for all models in the near-infrared. This means that photons have not scattered much along the equatorial plane before escaping the system, but have instead mainly scattered on the large dust clumps located high above the equatorial plane, resulting in the characteristic perpendicular polarization angle. When the line of sight of the observer becomes obstructed by dust, the polarization degree sharply rises since polar scattering clearly dominates over unpolarized emission from the (now) obscured source. Models with decreasing optical depth with radial distances from the center (6(c) and 6(d)) have the lowest polarization degrees, since photons easily escape from the system, and therefore do not carry large scattering-induced polarization. This effect is even more pronounced at equatorial inclinations when scattering along the equatorial plane dominates over polar scattering, resulting in a rotation of the polarization position angle for the two aforementioned models. The polarization degree thus

shows dips that have minima associated with the rotation of the polarization angle. The case is slightly different for the other three models (5, 6(a), and 6(b)). Their polarization degree is as high as 25% and it is always associated with a perpendicular polarization position angle. For increasing inclinations the polarization degree regularly decreases for the same reason as above but since obscuration by large, optically thick, outer clumps is more efficient, equatorial scattering does not dominate and the polarization position angle remains equal to 0°. At shorter wavelengths, the results are similar but the polarization degrees are lower (down to 7% for the most polarized models in the ultraviolet band) as obscuration and depolarization through multiple scattering dominate over transmission.

The time lags (bottom left panel of Figs. 10–12) are also very different for different dust opacity prescriptions. The time lags are similar for all models at polar inclinations, since they mainly result from scattering onto the large dust clouds at the outer radii of the fragmented disk. However, once the inclination is larger than 45°, the five models show different behaviors. Model 6(d) (density decreasing exponentially with distance) shows the lowest time lags that have an infrared maximum around $i = 50°$. The time lag decreases at equatorial inclinations as photons preferentially escape by scattering close to the equatorial plane, carrying a smaller time delay than photons that have backscattered onto the disk funnel and then inside the cloud distribution. The same conclusions apply to a model with a linear decrease of density. It follows that a clumpy disk with increasing cloud radii and decreasing optical depths would be, contrary to naive expectations, a poor target for reverberation measurements. Better targets are models 5, 6(a) and 6(b). The time lags increase with inclination, by factors up to up to 5. The presence of optically thick, large dust clouds in the outer borders of the system greatly facilitate time-lag observations since photons have to travel through the whole disk before these photons are efficiently blocked and/or scattered by dust. This statement is even strengthened at shorter wavelengths at which the time lags are larger because of the ability of optical and ultraviolet photons to penetrate deeper in the dusty medium.

In summary, our last set of models has shown that clumpy disks with clumps of variable sizes and optical thickness have very distinctive features that are very different for a variety of dust prescriptions. The importance of large and dense clumps at the outer edges of the disk is crucial for obtaining an efficient obscuration. They also enable large polarization degrees and time lags. If the disk becomes more transparent with radial distances from the source, obscuration is less efficient and we observe a rotation of the polarization angle with increasing inclinations.

4. Discussion and observational prospects

We have shown that varying the morphology and/or the distribution of dust density in equatorial dusty structures has a profound impact on the observational properties (total flux, polarization degree and angles, and time lags) we have considered. The flux detected at equatorial inclinations is very sensitive to the structure of the disk: uniform or fragmented media result in flux levels that can be orders of magnitude different from those observed at polar viewing angles. Clumpy structures (either with constant or variable cloudlet radii) tend to be less efficient in blocking radiation along the equatorial plane unless the outer clouds are substantially bigger than the inner clouds. The resulting polarization is also distinctively different between the three morphologies and we found it to be much more sensitive to the radial distribution of dust than the photometric marker. The polarization degree is inclination-dependent and varies together with rotations of the polarization position angle that can trace the dust stratification. Finally, the averaged time lags resulting from multiple scattering in different models is also a very distinctive signature that can probe the morphology of the scattering medium. Those two observational properties, polarization and time lags, are the bases of the polarized reverberation mapping technique introduced by Gaskell et al. (2012).

4.1. Polarized reverberation mapping

By comparing the amplitude of variability of the polarized flux to the amplitude of variability of the total flux in a blue passband with effective wavelength of 3600 Å, Gaskell et al. (2012) found that the polarized flux of the Seyfert-1 NGC 4151 follows the total flux with a lag of 8 ± 3 days. This, together with the orientation of the position angle of the polarized flux, enabled us to constrain the effective size of the unresolved equatorial scattering region of the AGN, most probably composed of electrons. This is the first and unique example so far illustrating the importance of polarized reverberation mapping in resolving the innermost structure of AGN. Achieving those observations is time consuming and required about 7 yr of monitoring the total and polarized fluxes of NGC 4151. In contrast with the work of Gaskell et al. (2012), who probed the inner broad line region, we showed here that dust scattering results in longer timescales on the order of several months for type-1 (polar) inclinations. It is therefore very important to select the optimal wavebands before starting such long observational campaigns.

Our results indicate that the near-infrared band seems to be the best to search for high degrees of polarization, since photons are not energetic enough to travel far into the dusty medium; instead, they are reflected (the albedo is large) and do not penetrate the disk much, leading to high polarization degrees. This applies to either polar, intermediate, or equatorial inclinations. However, thermal re-emission from dust and starlight dilution (from the host galaxy in the case of AGN) may also be strong enough to wipe out the polarization signature (Miller & Antonucci 1983). Hence, a more secure waveband to search for the polarization signal from dusty equatorial structures is ultraviolet, where starlight emission decreases in spiral and elliptical galaxies (Bolzonella et al. 2000).

The reverberation mapping technique requires us to observe both the continuum and reprocessed spectra; the central source must be directly visible and the line of sight must not cross the obscuring dusty torus. This limits us to polar viewing angles, for which the time lags are the shortest. In the AGN context, this is beneficial since the averaged time delays between variations of the polarized flux and total flux can be on the order of months (see Fig. 3 for example). We compared our results to those obtained by Almeyda et al. (2017), who have investigated the mid-infrared reverberation responses of a clumpy torus and found these responses to be in agreement with ours, even if the authors considered lower energies. Depending on the isotropic or anisotropic distribution of clumps in their torus models, Almeyda et al. (2017) have found an averaged optical-to-infrared time-lag of 80–150 days (i.e., 2.6–4.9 months) at 3.6 μm. In comparison, our clumpy model with constant cloudlet radius and optical depth gives a time lag of 3.9 months (cross-correlated between the total and polarized fluxes at 1 μm). Shorter delays can be obtained in the ultraviolet band, which is a conclusion that is also shared by Almeyda et al. (2017).

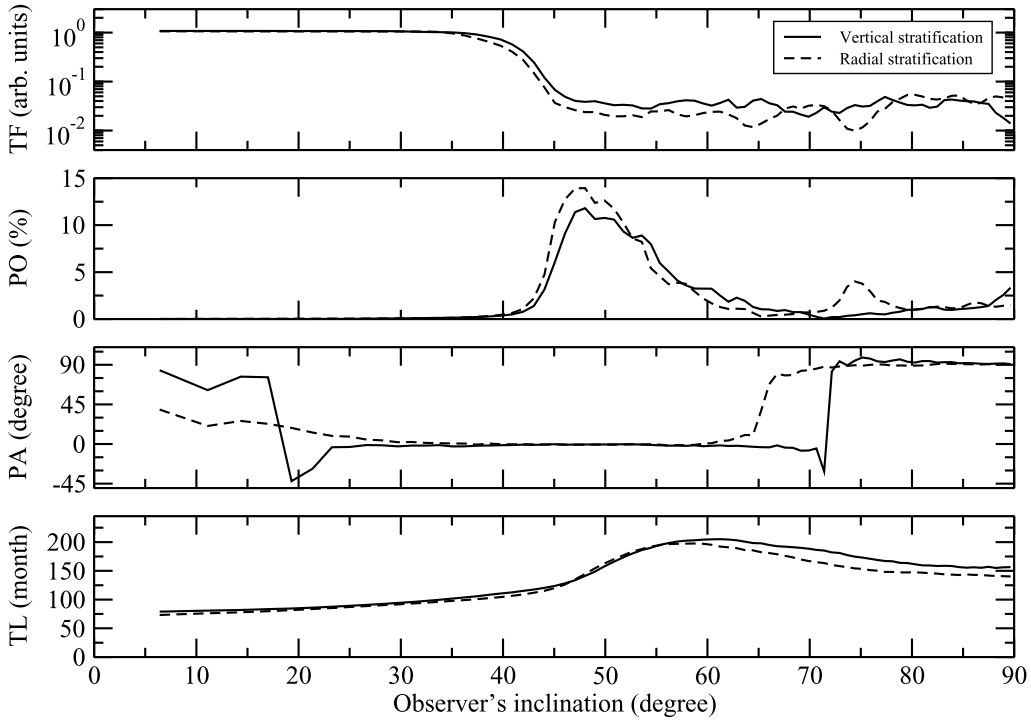

Fig. 13. Comparison between a radial (solid dashed line) and vertical (solid plain line) dust stratification in a clumpy equatorial flared disk with spheres of constant radius. The variation of the dust density is linear and decreases from the center of the model (first case) and from the equatorial plane (second case). The top panel shows the normalized photon flux at 1 μm, the second panel is the polarization degree, the third panel is the polarization position angle, and the last panel is the time lag as a function of the system inclination.

We therefore conclude that polarized reverberation mapping is very possibly better suited for ultraviolet/blue observations. The time lags between the unpolarized continuum and polarized reprocessed spectrum is shortened, while the observed polarization degree is less diluted by starlight contribution. The combination of the two techniques, leading to polarized time reverberation studies, strongly helps to break degeneracies. Our simulations suggest that much more sophisticated models are less easy to distinguish/constraint, but the combination of observables can still serve to rule out certain scenarios. The main difficulty here is that for low inclinations, the polarized fraction is small whereas for large inclinations, the unabsorbed, direct flux is severely reduced. Gaskell et al. (2012) nevertheless clearly established the feasibility of such an observational study for the case of NGC 4151, but one has to remember that it took them about 7 yr to complete the observations. Multiwavelength analysis such as radio observations to probe the kinematics and composition of the circumstellar/circumnuclear region or hard X-rays, which are much less absorbed/scattered than the optical, might be useful to narrow down the uncertainties. A detailed treatment of the problem is deferred to a forthcoming paper in which we intend to construct artificial light curves in both total and polarized light to measure realistic time lags, including both dilution by the host, interstellar polarization, and sophisticated transfer functions.

4.2. Toward more sophisticated models

We have shown that two dusty structures with the same geometry but different dust grain distributions (e.g., a linear increase and an exponential increase of opacity with radial distance from the central source) are distinctively different in terms of polarization and timing properties; see Fig. 12 for example. However, those differences are less likely to be detectable in terms of photometry, since almost all models give the same inclination-dependent trend in flux attenuation. To detect a radial stratification of dust, time-resolved polarimetry appears to be the solution but it is unclear whether this conclusion would also apply for vertical stratifications and chemical variations of the dust grains with distance from the source. It has been known for long that the dust composition and temperature of stellar nebulae varies with distance from its young star (Bally & Reipurth 2006); the same applies to galaxies, since the galactocentric dust mineralogy varies with distance and metallicity (Giannetti et al. 2017). We thus naturally expect circumstellar and circumnuclear dusty disks to be more complex than considered here.

It is beyond the scope of this paper to consider all possible dust distributions with distance, altitude, temperature, or metallicity. We have already proven that uniformly filled equatorial dusty structures give different polarimetric and timing outputs than structures with radial dust opacity gradients. However, in order to illustrate the complexity of the parameter space for filling the disk with dust, we show in Fig. 13 one realization of our numerical code for a clumpy disk with constant cloud radii in the case of a linear decrease of dust density with vertical distance from the equatorial plane. The simulation was achieved at 1 μm and results are shown in Fig. 13 using a plain solid black line. For comparison, we also show a model with the same parameters except that the gradient is now radial instead of vertical; the dust opacity linearly decreases with radial distance from the central source (black dashed line). As can be seen, the two configurations (vertical and radial variations of opacity) are almost indistinguishable in terms of photometry. The signal is the same at polar viewing angles and the obscured flux at equatorial orientations is equivalent. Differences can only be attributed to the random positions of the clouds. The unique true difference between the two models is the inclination angle at which the transition between the unobscured and obscured state occurs. The vertical opacity stratification configuration is similar to a configuration in which an optically thin atmosphere lays on top of denser equatorial layers. Photons grazing the disk surface are less likely to be absorbed. It is only at a larger inclination, where the medium finally becomes optically thick, that the disk can efficiently block radiation. In terms of polarization we see that the inclination-dependent degree of polarization follows the same trend, but the maximum amount of polarization is

only 11% instead of 14% at intermediate inclinations. The small bump of polarization observed at an inclination of ∼75° is due to the random distribution of the clumps position in the disk. The polarization position angle is the only marker showing a distinctive difference between the two configurations. The polarization angle is 90° for $i = 0°$, indicating that scattering mainly happens along the equatorial plane. In comparison, for a radial opacity stratification, the polarization angle is close to 45° since both equatorial and polar scattering are contributing. Here, the vertical stratification of dust density favors scattering along the equatorial plane where the disk is denser. For larger inclinations, the polarization angle rotates to 0°, as in the radial case, since backscattering on the disk funnel becomes important at those intermediate inclinations. It is only at large inclinations, when the continuum is obscured and when backscattering is no longer dominant with respect to equatorial scattering, that the polarization angle switches to 90°. Similarly to the photometric results, the angle at which this transition happens is different from the radial stratification scenario. Finally, the inclination-dependent averaged time lag is almost indistinguishable between the two cases since the geometry of the medium plays a more important role than its composition in time domain studies.

5. Conclusions

In this paper, we have shown that the morphology or the distribution of dust density of an equatorial dusty structure has a profound impact on the polarized signal and on the expected (averaged) time lags. A plain uniform structure may have a similar behavior to that of a complex clumpy structure in terms of flux attenuation but the polarization degree and angle would be significantly different. If the polarization signal from the equatorial dusty disk can be isolated from the central source or from additional components (which is more problematic in the case of AGN), it is possible, in principle, to distinguish between different models. In particular, the dust distribution inside a disk has a very clear inclination-dependent polarization signature. Since the inclination is not easy to determine from observations, coupling timing and polarimetric information are crucial for determining the physical size of the unresolved region together with its composition.

We also found that the ultraviolet/blue band is very probably better suited for polarized time-reverberation studies. The polarization level due to dust scattering is not expected to be as high as in the near-infrared, but the ultraviolet waveband should be less contaminated by external starlight and thermal re-emission. In addition, the time delays are expected to be slightly shorter in this waveband, allowing for less time-consuming observational campaigns. We intend to continue this study by applying cross-correlation methods to light curves obtained by our Monte Carlo method. We aim to reproduce the observed time delays of NGC 4151 first, estimate the inclination of the AGN by testing all the possible orientations thanks to our numerical code, and then try to evaluate the existence of additional structures in the AGN by checking their influence on the resulting polarization signal and time delays.

Acknowledgements. The authors would like to thank the anonymous referee for useful suggestions that helped to improve this paper. This research has been supported by the French Programme National des Hautes Energies (PNHE). F.M. is grateful for CNES funding under the post-doctoral grant "Probing the geometry and physics of active galactic nuclei with ultraviolet and X-ray polarized radiative transfer". A.P.R.L. acknowledge support from the CONICYT BECAS Chile grant no. 72150573.

References

Almeyda, T., Robinson, A., Richmond, M., Vazquez, B., & Nikutta, R. 2017, ApJ, 843, 3
Andrews, S. M., Wilner, D. J., Zhu, Z., et al. 2016, ApJ, 820, L40
Antonucci, R. 1993, ARA&A, 31, 473
Antonucci, R. R. J., & Miller, J. S. 1985, ApJ, 297, 621
Apai, D., Pascucci, I., Brandner, W., et al. 2004, A&A, 415, 671
Bally, J., & Reipurth, B. 2006, The Birth of Stars and Planets (Cambridge: Cambridge University Press)
Beckert, T., Driebe, T., Hönig, S. F., & Weigelt, G. 2008, A&A, 486, L17
Beckwith, S. V. W., & Sargent, A. I. 1996, Nature, 383, 139
Beckwith, S. V. W., Sargent, A. I., Chini, R. S., & Guesten, R. 1990, AJ, 99, 924
Bilíková, J., Chu, Y.-H., Gruendl, R. A., Su, K. Y. L., & De Marco O. 2012, ApJS, 200, 3
Bolzonella, M., Miralles, J.-M., & Pelló, R. 2000, A&A, 363, 476
Burtscher, L., & Tristram, K. R. W. 2013, The Messenger, 154, 62
Chu, Y.-H., Su, K. Y. L., Bilikova, J., et al. 2011, AJ, 142, 75
Clayton, G. C., De Marco, O., Nordhaus, J., et al. 2014, AJ, 147, 142
Czerny, B., & Hryniewicz, K. 2012, J. Phys. Conf. Ser., 372, 012013
D'Alessio, P., Cantö, J., Calvet, N., & Lizano, S. 1998, ApJ, 500, 411
D'Alessio, P., Calvet, N., Hartmann, L., Lizano, S., & Cantó, J. 1999, ApJ, 527, 893
Dubrulle, B., Morfill, G., & Sterzik, M. 1995, Icarus, 114, 237
Dullemond, C. P., Henning, T., Visser, R., et al. 2007, A&A, 473, 457
Eisner, J. A., Hillenbrand, L. A., White, R. J., et al. 2007, ApJ, 669, 1072
Farihi, J., Jura, M., & Zuckerman, B. 2009, ApJ, 694, 805
Gaskell, C. M., Goosmann, R., Antonucci, R., & Whysong, D. 2004, in AGN Physics with the Sloan Digital Sky Survey, eds. G. T. Richards, & P. B. Hall, ASP Conf. Ser., 311, 61
Gaskell, C. M., Goosmann, R. W., Merkulova, N. I., Shakhovskoy, N. M., & Shoji, M. 2012, ApJ, 749, 148
Giannetti, A., Leurini, S., König, C., et al. 2017, A&A, 606, L12
Gledhill, T. M., Scarrott, S. M., & Wolstencroft, R. D. 1991, MNRAS, 252, 50P
Gnedin, Y. N., Piotrovich, M. Y., Silant'ev, N. A., Natsvlishvili, T. M., & Buliga, S. D. 2015, Astrophysics, 58, 443
Goosmann, R. W., & Gaskell, C. M. 2007, A&A, 465, 129
Hillenbrand, L. A., Strom, S. E., Calvet, N., et al. 1998, AJ, 116, 1816
Holwerda, B. W., Bianchi, S., Böker, T., et al. 2012, A&A, 541, L5
Horne, K. 1985, MNRAS, 213, 129
Jaffe, W., Meisenheimer, K., Röttgering, H. J. A., et al. 2004, Nature, 429, 47
Jones, A. P. 2016, Roy. Soc. Open Sci., 3, 160224
Kishimoto, M., Hönig, S. F., Beckert, T., & Weigelt, G. 2007, A&A, 476, 713
Krolik, J. H., & Begelman, M. C. 1988, ApJ, 329, 702
Li, A. 2007, in The Central Engine of Active Galactic Nuclei, eds. L. C. Ho, & J.-W. Wang, ASP Conf. Ser., 373, 561
Liu, J., Liu, Y., Li, X., et al. 2016, MNRAS, 459, L100
López-Gonzaga, N., & Jaffe, W. 2016, A&A, 591, A128
Marin, F. 2014, MNRAS, 441, 551
Marin, F. 2016, MNRAS, 460, 3679
Marin, F., & Goosmann, R. W. 2014, in SF2A-2014: Proceedings of the Annual Meeting of the French Society of Astronomy and Astrophysics, eds. J. Ballet, F. Martins, F. Bournaud, R. Monier, & C. Reylé, 103
Marin, F., & Schartmann, M. 2017, A&A, 607, A37
Marin, F., Goosmann, R. W., Gaskell, C. M., Porquet, D., & Dovčiak M. 2012, A&A, 548, A121
Marin, F., Goosmann, R. W., & Gaskell, C. M. 2015, A&A, 577, A66
Marinucci, A., Bianchi, S., Matt, G., et al. 2016, MNRAS, 456, L94
Marsh, T. R., & Horne, K. 1988, MNRAS, 235, 269
Meisenheimer, K., Raban, D., Tristram, K., et al. 2008, The Messenger, 133, 36
Miller, J. S., & Antonucci, R. R. J. 1983, ApJ, 271, L7
Mundy, L. G., McMullin, J. P., Grossman, A. W., & Sandell, G. 1993, Icarus, 106, 11
Nenkova, M., Ivezić, Ž., & Elitzur, M. 2002, ApJ, 570, L9
Netzer, H. 2015, ARA&A, 53, 365
Pinte, C., Harries, T. J., Min, M., et al. 2009, A&A, 498, 967
Pollack, J. B., Hollenbach, D., Beckwith, S., et al. 1994, ApJ, 421, 615
Sazonov, S., Churazov, E., & Krivonos, R. 2015, MNRAS, 454, 1202
Scholz, A., Xu, X., Jayawardhana, R., et al. 2009, MNRAS, 398, 873
Schräpler, R., & Henning, T. 2004, ApJ, 614, 960
Siebenmorgen, R., Heymann, F., & Efstathiou, A. 2015, A&A, 583, A120
Stalevski, M., Fritz, J., Baes, M., Nakos, T., & Popović, L.Č. 2012, MNRAS, 420, 2756
Su, K. Y. L., Chu, Y.-H., Rieke, G. H., et al. 2007, ApJ, 657, L41
Vicente, S. M., & Alves, J. 2005, A&A, 441, 195
Walker, C., Wood, K., Lada, C. J., et al. 2004, MNRAS, 351, 607
Wolf, S., & Henning, T. 1999, A&A, 341, 675

Appendix B

Acronyms

ACF	:	Auto-Correlation Function
AD	:	Accretion Disk
ADAF	:	Advection Dominated Accretion Flow
AGN	:	Active Galactic Nucleus
BAL	:	Broad Absorption Line
BB	:	Black Body
BBB	:	Big Blue Bump
BEL	:	Broad Emission Line
BH	:	Black Hole
BLR	:	Broad Line Region
BP	:	Blandford-Payne
CCF	:	Cross Correlation Function
CCVF	:	Cross Covariance Function
CDT	:	Clumpy Dusty Torus
CFD	:	Clumpy Flared Disk
DDA	:	Discrete Dipole Approximation
FIR	:	Far Infra Red
FWHM	:	Full Width Half Maximum Infra Red
HIG	:	High Ionized Gas
IR	:	Infrared
ISM	:	interstellar Medium
ISCO	:	Innermost Stable Circular Orbit
LINER	:	Low Ionization Nuclear Emitting Region
LOC	:	Locally Optimally emitting Clouds
MASER	:	Microwave Amplification by Stimulated Emission of radiation
MHD	:	Magneto Hydrodynamic
MIR	:	Mid Infrared
MRN	:	Mathis, Rumpl and Nordsieck
NAL	:	Narrow Absorption Lines
NEL	:	Narrow Emission Line
NIR	:	Near Infrared
NLR	:	Narrow Line Region

PDF	:	Probability Distribution Function
PF	:	Polarized Flux
QSO	:	Quasi Stellar Object
QUASARS	:	Quasi Stellar Radio Source
RM	:	Reverberation Mapping
SED	:	Spectral Energy Distribution
SF	:	Star Formation
SMBH	:	Super Massive Black Hole
TF	:	Total Flux
UDT	:	Uniform Dusty Torus
UFD	:	Uniform Flared Disk
UFO	:	Ultra Fast Outflow
UV	:	Ultraviolet
WA	:	Warm Absorber

Bibliography

Afanasiev, V. L., Shapovalova, A. I., Popović, L. Č., and Borisov, N. V. (2015). Spectropolarimetric monitoring of active galaxy 3C 390.3 with 6-m telescope SAO RAS in the period 2009-2014. *MNRAS*, 448:2879 2889. 91

Antonucci, R. (1993). Unified models for active galactic nuclei and quasars. *ARA&A*, 31:473 521. 14

Antonucci, R. R. J. and Miller, J. S. (1985). Spectropolarimetry and the nature of NGC 1068. *ApJ*, 297:621 632. 3, 12, 21

Bagchi, J., Vivek, M., Vikram, V., Hota, A., Biju, K. G., Sirothia, S. K., Srianand, R., Gopal-Krishna, and Jacob, J. (2014). Megaparsec Relativistic Jets Launched from an Accreting Supermassive Black Hole in an Extreme Spiral Galaxy. *ApJ*, 788:174. 18

Bahcall, J. N., Kozlovsky, B.-Z., and Salpeter, E. E. (1972). On the Time Dependence of Emission-Line Strengths from a Photoionized Nebula. *ApJ*, 171:467. 73

Balbus, S. A. and Hawley, J. F. (1992). A Powerful Local Shear Instability in Weakly Magnetized Disks. IV. Nonaxisymmetric Perturbations. *ApJ*, 400:610 621. 24

Baldwin, J., Ferland, G., Korista, K., and Verner, D. (1995). Locally Optimally Emitting Clouds and the Origin of Quasar Emission Lines. *ApJ*, 455:L119. 26

Beckmann, V. and Shrader, C. R. (2012). *Active Galactic Nuclei*. 14, 15, 20, 21, 26

Bennert, N., Jungwiert, B., Komossa, S., Haas, M., and Chini, R. (2006). Size and properties of the narrow-line region in Seyfert-1 galaxies from spatially-resolved optical spectroscopy. *A&A*, 459:55 69. 28

Bentz, M. C., Denney, K. D., Cackett, E. M., Dietrich, M., Fogel, J. K. J., Ghosh, H., Horne, K., Kuehn, C., Minezaki, T., Onken, C. A., Peterson, B. M., Pogge, R. W., Pronik, V. I., Richstone, D. O., Sergeev, S. G., Vestergaard, M., Walker, M. G., and Yoshii, Y. (2006). A Reverberation-based Mass for the Central Black Hole in NGC 4151. *ApJ*, 651:775 781. 91

Blandford, R. D. and McKee, C. F. (1982). Reverberation mapping of the emission line regions of Seyfert galaxies and quasars. *ApJ*, 255:419 439. 73

Blandford, R. D. and Payne, D. G. (1982). Hydromagnetic flows from accretion discs and the production of radio jets. *MNRAS*, 199:883 903. 30

Blandford, R. D. and Znajek, R. L. (1977). Electromagnetic extraction of energy from Kerr black holes. *MNRAS*, 179:433 456. 30

Bohren, C. F. and Huffman, D. R. (1983). *Absorption and scattering of light by small particles*. 39, 40, 52

Chandrasekhar, S. (1931). The highly collapsed configurations of a stellar mass. *MNRAS*, 91:456 466. 23

Collinson, J. S., Ward, M. J., Landt, H., Done, C., Elvis, M., and McDowell, J. C. (2017). Reaching the peak of the quasar spectral energy distribution - II. Exploring the accretion disc, dusty torus and host galaxy. *MNRAS*, 465:358 382. 22

Done, C. (2010). Observational characteristics of accretion onto black holes. *ArXiv e-prints*. 24

Draine, B. T. (1988). The discrete-dipole approximation and its application to interstellar graphite grains. *ApJ*, 333:848 872. 38

Draine, B. T. and Lee, H. M. (1984). Optical properties of interstellar graphite and silicate grains. *ApJ*, 285:89 108. 39, 52

Einstein, A. (1915a). Die Feldgleichungen der Gravitation. *Sitzungsberichte der Königlich Preußischen Akademie der Wissenschaften (Berlin), Seite 844-847*. 23

Einstein, A. (1915b). Zur allgemeinen Relativitätstheorie. *Sitzungsberichte der Königlich Preußischen Akademie der Wissenschaften (Berlin), Seite 778-786*. 23

Einstein, A. (1916). Die Grundlage der allgemeinen Relativitätstheorie. *Annalen der Physik*, 354:769 822. 23

Emmering, R. T., Blandford, R. D., and Shlosman, I. (1992). Magnetic acceleration of broad emission-line clouds in active galactic nuclei. *ApJ*, 385:460 477. 26

Esin, A. A., McClintock, J. E., and Narayan, R. (1997). Advection-Dominated Accretion and the Spectral States of Black Hole X-Ray Binaries: Application to Nova Muscae 1991. *ApJ*, 489:865 889. 25

Fausnaugh, M. M., Grier, C. J., Bentz, M. C., Denney, K. D., De Rosa, G., Peterson, B. M., Kochanek, C. S., Pogge, R. W., Adams, S. M., Barth, A. J., Beatty, T. G., Bhattacharjee, A., Borman, G. A., Boroson, T. A., Bottorff, M. C., Brown, J. E., Brown, J. S., Brotherton, M. S., Coker, C. T., Crawford, S. M., Croxall, K. V., Eftekharzadeh, S., Eracleous, M., Joner, M. D., Henderson, C. B., Holoien, T. W.-S., Horne, K., Hutchison, T., Kaspi, S., Kim, S., King, A. L., Li, M., Lochhaas, C., Ma, Z., MacInnis, F., Manne-Nicholas, E. R., Mason, M., Montuori, C., Mosquera, A., Mudd, D., Musso, R., Nazarov, S. V., Nguyen, M. L., Okhmat, D. N., Onken, C. A., Ou-Yang, B., Pancoast, A., Pei, L., Penny, M. T., Poleski, R., Rafter, S., Romero-Colmenero, E., Runnoe, J., Sand, D. J., Schimoia, J. S., Sergeev, S. G., Shappee, B. J., Simonian, G. V., Somers, G., Spencer, M., Starkey, D. A., Stevens, D. J., Tayar, J., Treu, T., Valenti, S., Van Saders, J., Villanueva, Jr., S., Villforth, C., Weiss, Y., Winkler, H., and Zhu, W. (2017). Reverberation Mapping of Optical Emission Lines in Five Active Galaxies. *ApJ*, 840:97. 73

Fischer, T. C., Crenshaw, D. M., Kraemer, S. B., and Schmitt, H. R. (2013). Determining Inclinations of Active Galactic Nuclei via their Narrow-line Region Kinematics. I. Observational Results. *ApJS*, 209:1. 28

Fukue, J. and Sanbuichi, K. (1993). Model of obscuring molecular tori in Seyfert nuclei. *PASJ*, 45:135 138. 63

Gardner, E. and Done, C. (2014). A physical model for the X-ray time lags of narrow-line Seyfert type 1 active galactic nuclei. *MNRAS*, 442:2456 2473. 16

Gaskell, C. M. (2009). What broad emission lines tell us about how active galactic nuclei work. *New A Rev.*, 53:140 148. 27

Gaskell, C. M. and Goosmann, R. W. (2013). Line Shifts, Broad-line Region Inflow, and the Feeding of Active Galactic Nuclei. *ApJ*, 769:30. 42

Gaskell, C. M., Goosmann, R. W., Antonucci, R. R. J., and Whysong, D. H. (2004). The Nuclear Reddening Curve for Active Galactic Nuclei and the Shape of the Infrared to X-Ray Spectral Energy Distribution. *ApJ*, 616:147 156. 4, 59

Gaskell, C. M., Goosmann, R. W., Merkulova, N. I., Shakhovskoy, N. M., and Shoji, M. (2012). Discovery of Polarization Reverberation in NGC 4151. *ApJ*, 749:148. 3, 6, 12, 57, 58, 68, 74, 85, 87, 91

Gaskell, C. M., Klimek, E. S., and Nazarova, L. S. (2007). The Structure of the Torus and Broad-line Region Of AGNs. In *American Astronomical Society Meeting Abstracts*, volume 39 of *Bulletin of the American Astronomical Society*, page 947. 26

Gaskell, C. M. and Sparke, L. S. (1986). Line variations in quasars and Seyfert galaxies. *ApJ*, 305:175 186. 26, 73, 74

Goosmann, R. W. and Gaskell, C. M. (2007). Modeling optical and UV polarization of AGNs. I. Imprints of individual scattering regions. *A&A*, 465:129 145. 49, 50, 52, 60

Grosset, L., Rouan, D., Gratadour, D., Pelat, D., Orkisz, J., Marin, F., and Goosmann, R. (2018). Exploring the inner parsecs of active galactic nuclei using near-infrared high resolution polarimetric simulations with MontAGN. *A&A*, 612:A69. 49

Haardt, F. and Maraschi, L. (1991). A two-phase model for the X-ray emission from Seyfert galaxies. *ApJ*, 380:L51 L54. 25

Hawking, S. W. (1974). Black hole explosions? *Nature*, 248:30 31. 24

Hoyle, F. and Fowler, W. A. (1963). On the nature of strong radio sources. *MNRAS*, 125:169. 14, 15

Jovanović, P. and Popović, L. Č. (2009). X-ray Emission From Accretion Disks of AGN: Signatures of Supermassive Black Holes. *ArXiv e-prints*. 16

Kauffmann, G., Heckman, T. M., Tremonti, C., Brinchmann, J., Charlot, S., White, S. D. M., Ridgway, S. E., Brinkmann, J., Fukugita, M., Hall, P. B., Ivezić, Ž., Richards, G. T., and Schneider, D. P. (2003). The host galaxies of active galactic nuclei. *MNRAS*, 346:1055 1077. 14

Kishimoto, M., Antonucci, R., Boisson, C., and Blaes, O. (2005). Revealing AGN by Polarimetry. In Adamson, A., Aspin, C., Davis, C., and Fujiyoshi, T., editors, *Astronomical Polarimetry: Current Status and Future Directions*, volume 343 of *Astronomical Society of the Pacific Conference Series*, page 435. 73

Kishimoto, M., Hönig, S. F., Antonucci, R., Millan-Gabet, R., Barvainis, R., Millour, F., Kotani, T., Tristram, K. R. W., and Weigelt, G. (2013). Evidence for a Receding Dust @ARTICLE2010arXiv1008.2287D, author = Done, C., title = "Observational characteristics of accretion onto black holes", journal = ArXiv e-prints, archivePrefix = "arXiv", eprint = 1008.2287, primaryClass = "astro-ph.HE", keywords = Astrophysics - High Energy Astrophysical Phenomena, year = 2010, month = aug, adsurl = http://adsabs.harvard.edu/abs/2010arXiv1008.2287D, adsnote = Provided by the SAO/NASA Astrophysics Data System Sublimation Region around a Supermassive Black Hole. *ApJ*, 775:L36. 4, 68

Königl, A. (2006). AGN winds and jets: a theoretical perspective. *Mem. Soc. Astron. Italiana*, 77:598. 30

Koratkar, A. and Blaes, O. (1999). The Ultraviolet and Optical Continuum Emission in Active Galactic Nuclei: The Status of Accretion Disks. *PASP*, 111:1 30. 16

Korista, K. and Ferland, G. (1998). The Ultraviolet-Optical Albedo of Broad Emission Line Clouds. *ApJ*, 495:672 679. 42

Kormendy, J. and Richstone, D. (1995). Inward Bound The Search For Supermassive Black Holes In Galactic Nuclei. *ARA&A*, 33:581. 14

Koski, A. T. (1978). Spectrophotometry of Seyfert 2 galaxies and narrow-line radio galaxies. *ApJ*, 223:56 73. 28

Kraemer, S. B., Tombesi, F., and Bottorff, M. C. (2018). Physical Conditions in Ultra-fast Outflows in AGN. *ApJ*, 852:35. 29

Krolik, J. H. and Begelman, M. C. (1986). An X-ray heated wind in NGC 1068. *ApJ*, 308:L55 L58. 63

Krolik, J. H. and Lepp, S. (1989). The physical state of the obscuring torus in Seyfert galaxies. *ApJ*, 347:179 185. 63

Liang, E. P. T. and Price, R. H. (1977). Accretion disk coronae and Cygnus X-1. *ApJ*, 218:247 252. 25

Lira, P., Arévalo, P., Uttley, P., McHardy, I., and Breedt, E. (2011). Optical and near-IR long-term monitoring of NGC 3783 and MR 2251-178: evidence for variable near-IR emission from thin accretion discs. *MNRAS*, 415:1290 1303. 20

Liu, F. K. and Zhang, Y. H. (2002). A new list of extra-galactic radio jets. *A&A*, 381:757 760. 18

López-Gonzaga, N. and Jaffe, W. (2016). Mid-infrared interferometry of Seyfert galaxies: Challenging the Standard Model. *A&A*, 591:A128. 63

Loska, Z., Czerny, B., and Szczerba, R. (1993). The short-term disappearance of the broad-line region in NGC 5548 - Implications for the dusty torus model. *MNRAS*, 262:L31 L34. 63

Lynden-Bell, D. (1969). Galactic Nuclei as Collapsed Old Quasars. *Nature*, 223:690 694. 14

Lyubarskij, Y. E., Postnov, K. A., and Prokhorov, M. E. (1994). Eccentric Accretion Discs. *MNRAS*, 266:583. 24

Malkan, M. A. (1983). The ultraviolet excess of luminous quasars. II - Evidence for massive accretion disks. *ApJ*, 268:582 590. 24

Marin, F. (2014). A compendium of AGN inclinations with corresponding UV/optical continuum polarization measurements. *MNRAS*, 441:551 564. 7, 70

Marin, F. (2016). Are there reliable methods to estimate the nuclear orientation of Seyfert galaxies? *MNRAS*, 460:3679 3705. 22, 23

Marin, F. (2017). Unveiling the physics behind the spectral variations of changing-look quasars with optical polarimetry. *A&A*, 607:A40. 22

Marin, F. (2018). Modeling optical and UV polarization of AGNs. V. Dilution by interstellar polarization and the host galaxy. *A&A*, 615:A171. 49

Marin, F., Goosmann, R. W., and Gaskell, C. M. (2015). Modeling optical and UV polarization of AGNs. III. From uniform-density to clumpy regions. *A&A*, 577:A66. 49, 64, 65

Marin, F., Goosmann, R. W., Gaskell, C. M., Porquet, D., and Dovčiak, M. (2012). Modeling optical and UV polarization of AGNs. II. Polarization imaging and complex reprocessing. *A&A*, 548:A121. 49, 83

Marin, F., Rojas Lobos, P. A., Hameury, J. M., and Goosmann, R. W. (2018). A near-infrared, optical, and ultraviolet polarimetric and timing investigation of complex equatorial dusty structures. *A&A*, 613:A30. 91

Marscher, A. P. (2005). Multiband Impressions of Active Galactic Nuclei. *Mem. Soc. Astron. Italiana*, 76:168. 30, 31

Mathis, J. S., Rumpl, W., and Nordsieck, K. H. (1977). The size distribution of interstellar grains. *ApJ*, 217:425 433. 4, 52, 62

Meyer-Hofmeister, E., Liu, B. F., and Meyer, F. (2009). The hard to soft spectral transition in LMXBs-affected by recondensation of gas into an inner disk. *A&A*, 508:329 337. 25

Meyer-Hofmeister, E., Liu, B. F., and Qiao, E. (2017). Interaction of the accretion flows in corona and disk near the black hole in active galactic nuclei. *A&A*, 607:A94. 25

Middei, R., Vagnetti, F., Bianchi, S., La Franca, F., Paolillo, M., and Ursini, F. (2017). A long-term study of AGN X-ray variability . Structure function analysis on a ROSAT-XMM quasar sample. *A&A*, 599:A82. 19

Mushotzky, R. F., Fabian, A. C., Iwasawa, K., Kunieda, H., Matsuoka, M., Nandra, K., and Tanaka, Y. (1995). Detection of broad iron K lines in active galaxies. *MNRAS*, 272:L9 L12. 15

Nandra, K. (2001). X-Ray Variability of AGN and Its Relationship to the Optical/UV. In Peterson, B. M., Pogge, R. W., and Polidan, R. S., editors, *Probing the Physics of Active Galactic Nuclei*, volume 224 of *Astronomical Society of the Pacific Conference Series*, page 167. 19

Narayan, R. and Yi, I. (1995). Advection-dominated Accretion: Underfed Black Holes and Neutron Stars. *ApJ*, 452:710. 24

Netzer, H. (2013). *The Physics and Evolution of Active Galactic Nuclei*. 28

Peterson, B. M. (1997). *An Introduction to Active Galactic Nuclei*. 15, 28

Peterson, B. M., Ferrarese, L., Gilbert, K. M., Kaspi, S., Malkan, M. A., Maoz, D., Merritt, D., Netzer, H., Onken, C. A., Pogge, R. W., Vestergaard, M., and Wandel, A. (2004). Central Masses and Broad-Line Region Sizes of Active Galactic Nuclei. II. A Homogeneous Analysis of a Large Reverberation-Mapping Database. *ApJ*, 613:682 699. 73

Peterson, B. M. and Horne, K. (2004). Echo mapping of active galactic nuclei. *Astronomische Nachrichten*, 325:248 251. 73, 74

Pier, E. A. and Krolik, J. H. (1992). Infrared spectra of obscuring dust tori around active galactic nuclei. I - Calculational method and basic trends. *ApJ*, 401:99 109. 27

Pogge, R. W. (1988). A extended ionizing radiation cone from the nucleus of the Seyfert 2 galaxy NGC 1068. *ApJ*, 328:519 522. 28

Ponti, G., Papadakis, I., Bianchi, S., Guainazzi, M., Matt, G., Uttley, P., and Bonilla, N. F. (2012). CAIXA: a catalogue of AGN in the XMM-Newton archive. III. Excess variance analysis. *A&A*, 542:A83. 19

Popović, L. Č. (2003). Balmer Lines as Diagnostics of Physical Conditions in Active Galactic Nuclei Broad Emission Line Regions. *ApJ*, 599:140 146. 86

Pringle, J. E., Rees, M. J., and Pacholczyk, A. G. (1973). Accretion onto Massive Black Holes. *A&A*, 29:179. 14

Purcell, E. M. and Pennypacker, C. R. (1973). Scattering and Absorption of Light by Nonspherical Dielectric Grains. *ApJ*, 186:705 714. 38

Ramírez, J. M. and Tombesi, F. (2012). On the X-ray low- and high-velocity outflows in active galactic nuclei. *MNRAS*, 419:L64 L68. 29

Rani, P., Stalin, C. S., and Rakshit, S. (2017). X-ray flux variability of active galactic nuclei observed using NuSTAR. *MNRAS*, 466:3309 3322. 20

Rojas Lobos, P. A., Goosmann, R. W., Marin, F., and Savić, D. (2018). Modeling optical and UV polarization of AGNs. IV. Polarization timing. *A&A*, 611:A39. 4, 5, 63, 69, 70

Rubin, V. C. and Ford, Jr., W. K. (1966). Image Tube Spectra of Quasi-Stellar Objects. *AJ*, 71:396. 16

Rubin, V. C. and Ford, Jr., W. K. (1968). Spectrographic Study of the Seyfert Galaxy NGC 3227. *ApJ*, 154:431. 16

Ruiz, M., Young, S., Packham, C., Alexander, D. M., and Hough, J. H. (2003). Near-infrared imaging polarimetry and modelling of NGC 4151. *MNRAS*, 340:733 738. 4, 58

Rybicki, G. B. and Lightman, A. P. (1985). *Radiative processes in astrophysics*. 34, 38

Salpeter, E. E. (1964). Accretion of Interstellar Matter by Massive Objects. *ApJ*, 140:796 800. 14, 15

Sartori, L. F., Schawinski, K., Trakhtenbrot, B., Caplar, N., Treister, E., Koss, M. J., Urry, C. M., and Zhang, C. E. (2018). A model for AGN variability on multiple time-scales. *MNRAS*, 476:L34 L38. 73

Schmidt, M. (1969). Quasistellar Objects. *ARA&A*, 7:527. 13

Schwarzschild, K. (1916). On the Gravitational Field of a Mass Point According to Einstein's Theory. *Abh. Konigl. Preuss. Akad. Wissenschaften Jahre 1906,92, Berlin,1907*, 1916. 23

Seyfert, C. K. (1943). Nuclear Emission in Spiral Nebulae. *ApJ*, 97:28. 13, 16, 26

Shakura, N. I. and Sunyaev, R. A. (1973). Black holes in binary systems. Observational appearance. *A&A*, 24:337 355. 14, 15, 24

Shibata, K. and Uchida, Y. (1985). A magnetodynamic mechanism for the formation of astrophysical jets. I - Dynamical effects of the relaxation of nonlinear magnetic twists. *PASJ*, 37:31 46. 30

Shields, G. A. (1978). Thermal continuum from acretion disks in quasars. *Nature*, 272:706 708. 14

Shields, G. A., Oke, J. B., and Sargent, W. L. W. (1972). The Optical Spectrum of the Seyfert Galaxy 3c 120. *ApJ*, 176:75. 17, 18

Siebenmorgen, R., Heymann, F., and Efstathiou, A. (2015). Self-consistent two-phase AGN torus models⋆.*SEDlibraryforobservers*.*A&A*, 583 : *A*120. 27

Silk, J. and Rees, M. J. (1998). Quasars and galaxy formation. *A&A*, 331:L1 L4. 14

Smith, H. J. and Hoffleit, D. (1963). Light Variations in the Superluminous Radio Galaxy 3C273. *Nature*, 198:650 651. 14

Smith, J. E., Robinson, A., Alexander, D. M., Young, S., Axon, D. J., and Corbett, E. A. (2004). Seyferts on the edge: polar scattering and orientation-dependent polarization in Seyfert 1 nuclei. *MNRAS*, 350:140 160. 6, 70, 71

Stalevski, M. (2012). SKIRTOR - database of modelled AGN dusty torus SEDs. *Bulgarian Astronomical Journal*, 18(3):3. 49

Stalevski, M., Fritz, J., Baes, M., Nakos, T., and Popović, L. Č. (2012). 3D radiative transfer modelling of the dusty tori around active galactic nuclei as a clumpy two-phase medium. *MNRAS*, 420:2756 2772. 27

Steinacker, J., Henning, T., Bacmann, A., and Semenov, D. (2003). 3D continuum radiative transfer in complex dust configurations around stellar objects and active galactic nuclei. I. Computational methods and capabilities. *A&A*, 401:405 418. 43

Tombesi, F., Cappi, M., Reeves, J. N., and Braito, V. (2012). Evidence for ultrafast outflows in radio-quiet AGNs - III. Location and energetics. *MNRAS*, 422:L1 L5. 29

Tombesi, F., Cappi, M., Reeves, J. N., Nemmen, R. S., Braito, V., Gaspari, M., and Reynolds, C. S. (2013). Unification of X-ray winds in Seyfert galaxies: from ultra-fast outflows to warm absorbers. *MNRAS*, 430:1102 1117. 29

Tombesi, F., Cappi, M., Reeves, J. N., Palumbo, G. G. C., Yaqoob, T., Braito, V., and Dadina, M. (2010a). Evidence for ultra-fast outflows in radio-quiet AGNs. I. Detection and statistical incidence of Fe K-shell absorption lines. *A&A*, 521:A57. 29

Tombesi, F., Sambruna, R. M., Reeves, J. N., Braito, V., Ballo, L., Gofford, J., Cappi, M., and Mushotzky, R. F. (2010b). Discovery of Ultra-fast Outflows in a Sample of Broad-line Radio Galaxies Observed with Suzaku. *ApJ*, 719:700 715. 29

Uchida, Y. and Shibata, K. (1985). Sweeping pinch mechanism and the acceleration of jets in astrophysics. In Kundu, M. R. and Holman, G. D., editors, *Unstable Current Systems and Plasma Instabilities in Astrophysics*, volume 107 of *IAU Symposium*, pages 287 291. 30

Vaona, L., Ciroi, S., Di Mille, F., Cracco, V., La Mura, G., and Rafanelli, P. (2012). Spectral properties of the narrow-line region in Seyfert galaxies selected from the SDSS-DR7. *MNRAS*, 427:1266 1283. 28

Vlahakis, N. and Königl, A. (2004). Relativistic Outflows in AGNs. In Richards, G. T. and Hall, P. B., editors, *AGN Physics with the Sloan Digital Sky Survey*, volume 311 of *Astronomical Society of the Pacific Conference Series*, page 151. 30

Wang, J., Zhang, J., Gao, Y., Zhang, Z.-Y., Li, D., Fang, M., and Shi, Y. (2014). SiO and CH_3OH mega-masers in NGC 1068. *Nature Communications*, 5:5449. 21

Watanabe, M., Nagata, T., Sato, S., Nakaya, H., and Hough, J. H. (2003). Simultaneous Optical and Near-Infrared Spectropolarimetry of Type 2 Seyfert Galaxies. *ApJ*, 591:714 732. 49

Wolf, S. and Henning, T. (1999). AGN polarization models. *A&A*, 341:675 682. 49

Woltjer, L. (1959). Emission Nuclei in Galaxies. *ApJ*, 130:38. 15

Wu, X.-B., Wang, R., Kong, M. Z., Liu, F. K., and Han, J. L. (2004). Black hole mass estimation using a relation between the BLR size and emission line luminosity of AGN. *A&A*, 424:793 798. 73

Xue, S.-j. and Cheng, F.-z. (1998). Reverberation mapping analysis of the broad-line region in Seyfert galaxy NGC 4151. *Chinese Astron. Astrophys.*, 22:395 408. 91

Yang, Q., Wu, X.-B., Fan, X., Jiang, L., McGreer, I., Shangguan, J., Yao, S., Wang, B., Joshi, R., Green, R., Wang, F., Feng, X., Fu, Y., Yang, J., and Liu, Y. (2018). Discovery of 21 New Changing-look AGNs in the Northern Sky. *ApJ*, 862:109. 22